Fracturing of tight rocks during internal fuid production : implications for primary migration

Maya Kobchenko

UNIVERSITÉ DE GRENOBLE

THÈSE

Pour obtenir le grade de

DOCTEUR DE L'UNIVERSITÉ DE GRENOBLE

Préparée dans le cadre d'une cotutelle entre l'Université de Grenoble et l'Université d'Olso

Spécialité : **Terre Univers Environnement**

Arrêté ministériel : le 6 janvier 2005 -7 août 2006

Présentée par

Maya KOBCHENKO

Thèse dirigée par **François RENARD** et **Dag Kristian Dysthe**

préparée au sein des **Laboratoires Physics of Geological Processes (Oslo) et ISTerre (Grenoble**

dans **l'Ecole Doctorale Terre Univers Environnement**

Fracturation durant la production interne de fluides dans les roches : application à la migration primaire d'hydrocarbures

Thèse soutenue publiquement le **5 Juillet 2013**
devant le jury composé de :

Monsieur, François, RENARD
Professeur, Université Grenoble I (Membre)
Madame, Einat, AHARONOV
Associate Professor, Hebrew University in Jerusalem (Membre)
Monsieur, Harold, AURADOU
Directeur de Recherche, Laboratoire FAST, Orsay (Membre)
Madame, Luiza, ANGHELUTA
Postdoctoral Researcher, University of Oslo (Membre)

Université Joseph Fourier / Université Pierre Mendès France / Université Stendhal / Université de Savoie / Grenoble INP

Thesis supervisors:

Dag K. Dysthe,
Physics of Geological Processes, University of Oslo, Norway;

François Renard,
Physics of Geological Processes, University of Oslo, Norway and
Univ. Joseph Fourier, ISTerre, BP 53, F-38041 Grenoble;

Paul Meakin,
Physics of Geological Processes, University of Oslo, Norway and
Temple University, Department of Physics, Barton Hall, Philadelphia, PA 19122-6082

"A journey of a thousand miles begins with a single step" – Lao-tzu

Contents

Acknowledgments

Many things happened to me for a first time when I came to Norway four years ago. It was my first stay outside Russia, first year of marriage, first time everyday speaking English and first acquaintance with geophysics. These circumstances in combination were not easy to deal with. But here I am, writing acknowledgments to my PhD-thesis, and it would not have been possible if not all the amazing people which I was so lucky to meet on my way. To all those who believed in me I dedicate this work.

I would like to thank Yuri Podladchikov and Marcin Dabrowski for first introducing and involving me in PGP activities, who also inspired me to switch from theoretical mechanics to geophysics.

The greatest thanks to my dear supervisors – Dag Kristian Dysthe, François Renard and Paul Meakin for being not just excellent supervisors but sometimes more like a family for me.

Thank you, Dag Kristian, for trusting me with experimental project despite my theoretical background, for many hours that you spent with me in the lab and in front of your blackboard making this thesis possible, for enormous scientific and emotional support, and for being my PhD-"father" through these years.

Thank you, François, for your never ending enthusiasm, for generous support and cheering, for your ability to organize and structure things, for

unforgettable trips to France, for all the wine and cheese, and for being a supervisor, which one can only dream about.

Thank you, Paul, for being fantastic group leader, for seeing and putting things in perspective and broad scientific context, for patiently correcting my English and for always willing to take the time to share your wisdom.

I would like to thank Bjørn Jamtveit particulary for welcoming me to PGP with open arms and for giving the opportunity to continue working in multidisciplinary environment.

Special thanks to Olav Gundersen – for being my supervisor in the lab, thank you, Olav, for always willing to share your experience and knowledge, being always positive and more then helpful, and for your "there are no problems – there are challenges".

Thank you, Olivier, for involving me into analogue experiments, for general inspiration and good example of scientific communication.

Thank you to my former office mates, Jacqueline and Marta for the coolest ever girls office, to Kirsten Fristad for showing no mercy in training me English, to Liene and Elvira for staying my friends in spite of geography, to Kristin Larssen, Amélie Neuville and Camilla Kirkemo for great climbing, biking and skiing trips, to Andreas Hafver and Espen for fruitful collaboration and help at the end of my PhD, to Jørgen for his inspiring life credo, to Anja Røyne and Victoria Yarushina for making me believe that babies and science are compatible, thank you to Mauro and OSI Friidrett for the great fun and challenging sport activities, thank you to my Russian friends in Norway, Tanja and Evgueny, for making me feel like home.

However the biggest thank you goes to my husband Rodion, who is not always the "easiest" one to be married to, but who always has been there for me when I really needed and whom I love with every beat of my heart.

Introduction

The problems addressed in this thesis are part of a wider topic, which has attracted considerable attention in recent years: fluid migration into rocks that consume fluids by heterogeneous reactions, and fluid migration out of rocks that produce fluids and/or undergo compaction. The release and consumption of fluids are two fundamentally different processes [1]. This work focuses on the second type of processes, the generation of fluids due to chemical reaction leading to fluid production inside a rock matrix and the associated expulsion of fluid. Depending on the fluid migration rate and the rates of the chemical reaction, different mechanisms of fluid release can be operating. If the rock matrix has a relatively high permeability, the fluid transport is governed by Darcy flow in porous media. The Darcy equation (a linear relationship between the fluid flux and the pressure gradient) describes, for example, expulsion of water, gas or oil through compacting sedimentary rocks and fluid release during prograde metamorphism [2, 3]. Fine-grained rocks such as shales and mud stones usually have a very low initial permeability and fluid transport cannot be accommodated sufficiently rapidly by Darcy flow. In such case, the increasing fluid pressure gradients may lead to internal hydraulic fracturing [4]. Flow in reaction generated cracks or other high permeability and low capillary pressure pathways appears to be essential for the migration of hydrocarbons out of shale source rocks (primary migration) [5] into more permeable secondary migration pathways. This thesis addresses the coupling between fluid generation, crack formation and fluid flow through the fracture networks generated in such tight rocks.

1 Hydrocarbon relevance

Oil seeps out of the ground in many places, and oil seeps have played an important role in the discovery of important petroleum resources. Bitumen or crude oil obtained from seeps has been used for lighting and medicine since ancient time. In the nineteenth century biodegraded heavy oil was mined directly from the shafts, which were bored around the seepage places. Later it was found that oil and gas often accumulate where layers of sedimentary rocks form domes and faults. A low permeability layer (seal or cap rock) composed of low permeability rocks, mostly shales, covers reservoir and prevents oil from migrating to the surface (Fig .1).

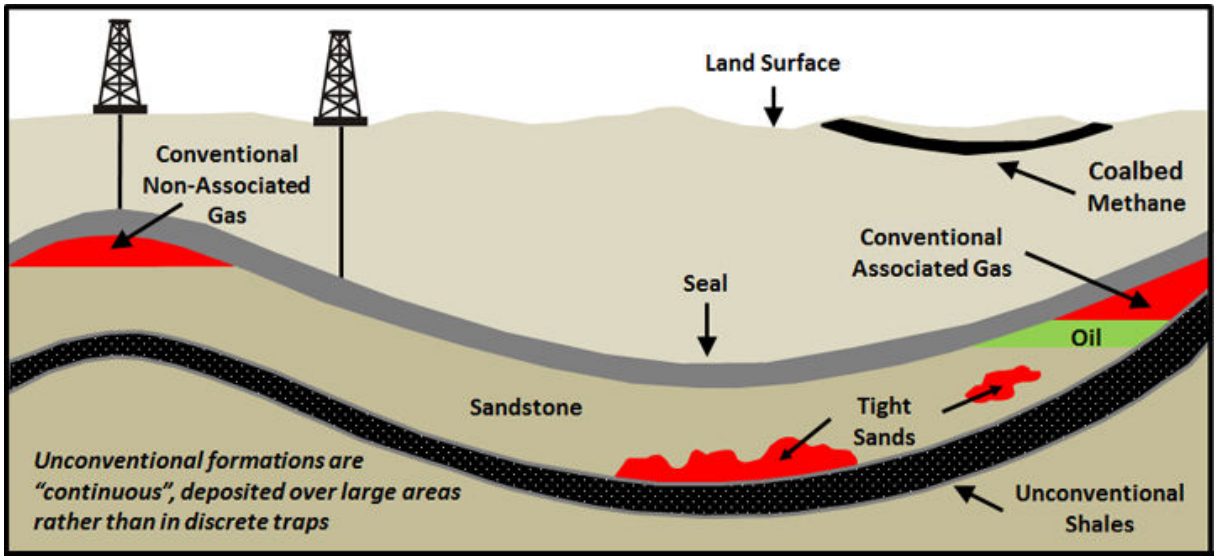

Figure .1: Conventional and unconventional petroleum reservoirs. Image after http://greatbearpetro.com/unconventional-reservoirs-explained.html

Although there are some claims that oil and/or gas are formed in large quantities via abiogenic processes, most oil industry scientists and academic geologists believe that essentially all of the world's oil and gas has organic origins (Fig .2B). Essentially all of our oil resources and most of our gas formed by the slow thermal decomposition (maturation) of solid kerogen (organic material) in sedimentary source rock (organic-rich shale). However, substantial amounts of natural gas are generated from organic

matter by methanogenic microbes at relatively shallow depths. Depending on the burial depth, thermal gradients and time of exposure, the very high molecular mass kerogen breaks into oil at temperatures between $100 - 150$ ° C (in the oil window) and/or into gas at higher temperatures and depths (in the gas window). In addition, some of the oil retained in the source rock may be converted into natural gas as the temperature and burial depth increases. In general the rate of petroleum generation can be expressed by the Arrhenius law: $K = A\exp(-E/RT)$, where A is a weakly temperature dependent pre-exponential frequency factor, E is the activation energy, R is the gas constant and T is the absolute temperature. The reaction rate is very strongly temperature dependent, but because of the slow increase in the burial depth, which results in a slow increase in temperature, the typical time of petroleum generation under natural conditions can vary in the range of $1 - 100$ millions of years.

Part of the petroleum generated in the organic-rich source rock is expelled and migrates along secondary migration pathways to trapping formations (reservoirs) where it accumulates. Movement of petroleum via carrier beds to reservoirs is divided into primary migration, defined as the escape of hydrocarbons from the tight low permeability source rock, and secondary migration through more permeable rocks to a trap or reservoir. Although it is accepted that migration is driven primarily by buoyancy, hydrodynamic forces may also play a significant role. The primary hydrocarbon expulsion from low permeability source rock is still poorly understood, but it is clear that capillary forces together with stratigraphic heterogeneities direct migration along low capillary force pathways and that the lateral migration can be greater than the vertical. Because in the fine-grained shales the capillary forces act against hydrocarbon migration, a significant fraction of the generated petroleum is not expelled from the source rock, which can form an unconventional reservoir for oil and/or gas. During recent years, new technology and rising gas and oil prices has made shale gas, produced directly from mature and overmature source rocks, an important source of energy. If the source rock is immature (oil shale), artificial heating may be used to generate oil and gas. Because the recov-

Figure .2: **A)** Organic-rich source rocks in the Polish Outer Carpathians. A series of waterfalls built of laminated black shales in Rzyki. **B)** Fish fossil between shale lamination in the Menilite Formation in Rowne, Poland. **C)** Shale cores from the Iwiczna Core Warehouse, Poland. **D)** Liquid oil seeping through the ground surface in the Museum of Oil Industry in Bobrka, Poland.

ery factors for unconventional fuels (the amount of hydrocarbons extracted from the source rock relative to the oil in place) are much lower than for conventional reservoirs, a better understanding of fundamental processes that control hydrocarbon generation and retention is a high priority for the petroleum industry.

2 Organic-rich shales and primary migration

Shale is a fine-grained sedimentary rock that forms from the compaction of silt ($0.004 - 0.063$ mm size) and clay (< 0.004 mm size) mineral particles. Well defined lamination and heterogeneous mechanical properties (Fig .2 A,C) are characteristic properties of shales. If shale has sufficient biological material (kerogen) dispersed between inorganic lamina it can form a source rock for oil and gas. When this source rock is buried the temperature and pressure rises until the high-molecular kerogen decomposes into hydrocarbons that have lower densities and viscosities by the process called maturation.

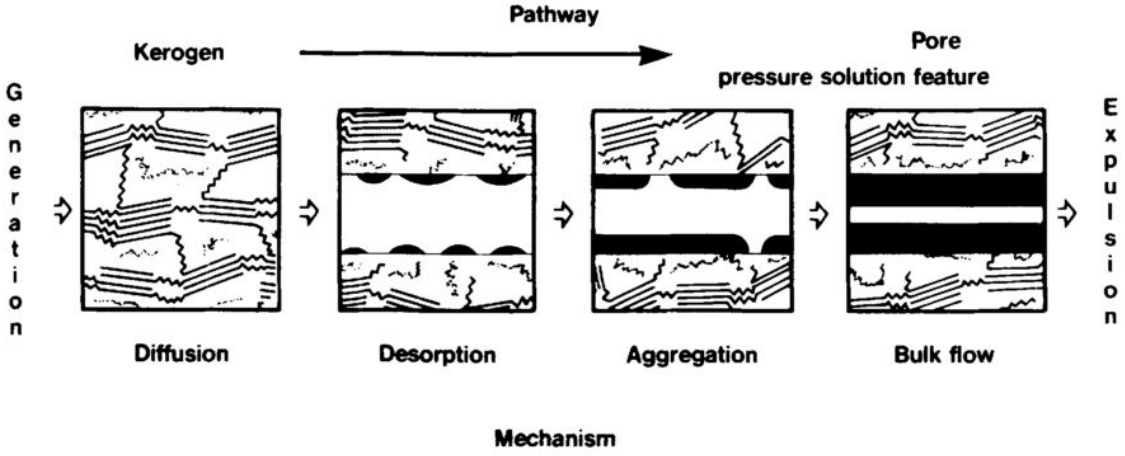

Figure .3: After [6]: Mechanism of petroleum expulsion from the source rock.

Despite decades of research, it remains an enigma how the generated hydrocarbons escape from the source rocks. Some authors believe that petroleum moves as separate oil and gas phases [7, 8]. Others postulate

that oil migrates in solution in water or gas [9]. A number of studies supports the idea that primary migration occurs as diffusion of bitumen molecules through organic matter networks [10]. Others claim that bulk flow of petroleum through the source rock matrix is the main mechanism [11, 12]. Most likely, there is more than one mechanism operating at different times and stages of maturation, and the pathways and efficiencies of individual mechanisms depend on the temperature/pressure history, shale composition, abundance of micro- and macro- pores and other factors [6].

The pores in organic-rich source rock are extremely small (the size of few 100 Å or less) and as a result, the permeability is very low (on the order of 0.01 nanodarcy). If organic-rich shale includes thin lamina of silt and sandstone, the escape of the hydrocarbon generated from kerogen may occur as bulk flow via these more permeable pathways. Otherwise, on short length scales the transport of generated oil and gas out of the source rock is more likely dominated by diffusion than Darcy flow [13]. Figure .3 indicates how diffusion (out of tight shale into more permeable pathways) and bulk flow (through more permeable pathways) act in combination during hydrocarbon migration out of the source rock. Since the

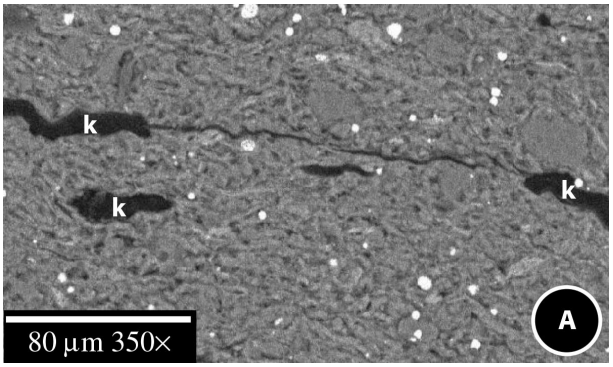

Figure .4: After [5]: Backscattered electron image of a black shale showing a micro-crack originated within kerogen patches.

diffusion time is proportional to the square of the diffusion distance, diffusion is not fast enough to transport hydrocarbon fluids over large distances, and this suggests that the existence of more permeable for petroleum pathways is needed. Several authors indicate that the formation of microcracks

plays an important role [14, 15, 5].

3 Methods

3.1 Fractures

At shallow depths, rocks are typically low strength brittle materials and they usually contain healed and unhealed fractures over a wide range of length scales. Fracture patterns, such as that shown in (Fig .5A) may be diverse due to the different stresses that drive them, the different materials in which they are formed, and the different temperatures and chemical environments in which fracturing occurs. Variations as well as similarities in these patterns may provide information about fracturing processes and the conditions under which fracturing occurred. Understanding the basic strength properties of rocks has been a practical pursuit since ancient times, both because of the importance of mining and because rock was a widely used building material. The crafting of stone tools, mining and quarrying required an intimate knowledge of crack propagation processes and mechanical properties of the rock. Fracture mechanics explains fracture formation and propagation in terms of strain and stress. According to fracture mechanics, a material fails when sufficient stress and work are applied on the atomic level to break the bonds that hold atoms together [16]. Fractures occur when the stress exceeds the rock strength, which can be viewed as the maximum stress that material can support under given conditions.

Fractures play an important role in many natural geological systems. Depending on the mineral composition, structure of the rock, loading conditions as well as pressure and temperature, various type of behaviour such as linear elastic, non-linear elastic, plastic, brittle failure etc. can be observed. A common way of studying rock behaviour is to measure the stress and strain during axial compression of a cylindrical sample to obtain a stress-strain curve $\sigma = f(\epsilon)$. If this function is linear then the stress is related linearly to the strain and the coefficient is the Youngs modulus,

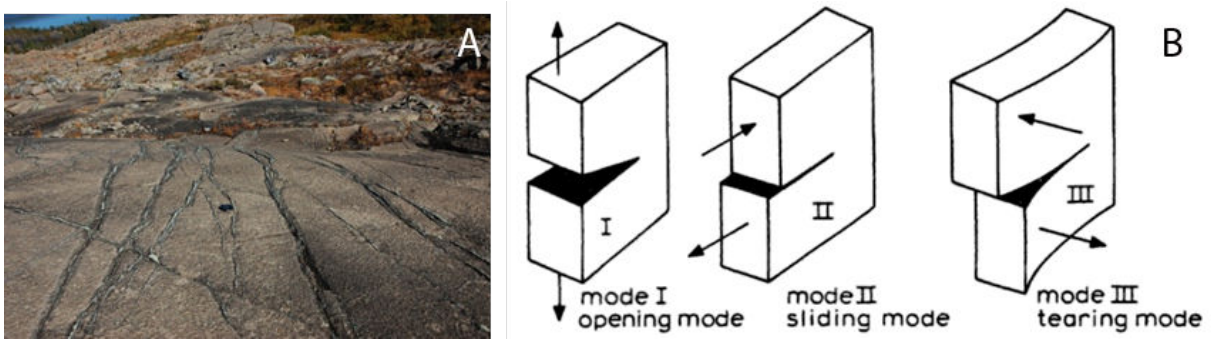

Figure .5: **A)**: Cracks in Ultramafic rocks, Røragen. **B)**: [17] The three modes of fracture: 1) opening mode (extension fracture, mode I propagation); 2) sliding mode (shear fracture, mode II propagation); and 3) tearing mode (shear fracture, mode III propagation).

$E = \sigma/\epsilon$ [18]. If the rock is loaded beyond the yield stress (elastic limit), it may behave in a ductile manner (the rock flows) or a brittle manner (the rock fractures). In brittle deformation, rocks break along well-defined fractures planes or zones, which correspond to surfaces where rock has lost cohesion. Fractures provide conduits for fluid migration through solid rock and therefore play significant role in weathering processes, migration of ground water and hydrocarbons, hydrothermal and metamorphic fluids. The fracture geometry at different scales features self-similarity, which means that the spatial distribution and geometrical pattern does not depend on the scale at which fractures are observed.

Fractures can be either extension fractures or shear fractures, depending on the motion relative to the fracture plane (Fig .5 B). For extensional fractures, the motion during fracture propagation happens in the direction perpendicular to the fracture plane, which is called mode I type propagation. For shear fractures the relative motion occurs parallel to the fracture walls, and fracture can propagate by two regimes, either by mode II, when the sliding occurs perpendicular to the fracture tip, or by mode III, when the propagation happens parallel to the fracture tip. Joins represent examples of extension fractures, faults are shear fractures at the scale of outcrop or greater.

3.2 The stress tensor

Traction is the force divided by the area over which the force is distributed $\mathbf{\Sigma} = \frac{\mathbf{F}}{A}$. The tractions acting on the opposite sides of a surface must be equal and opposite to keep the surface in equilibrium. This pair of tractions is called surface stress. The state of stress at a point, or simply stress, is defined in 2D by knowing surface stress on two different planes through this point, and in 3D – on three non-parallel planes. Because each surface stress is represented by its normal and shear components (σ_n and σ_s) in 2D and three components in 3D, we need a four component matrix (stress tensor) to define stress state in a point in 2D and nine component stress tensor for defining state of stress in 3D. The diagonal elements are the normal-pressure acting onto surfaces within material, whilst the off diagonal entries are the shear stresses (Fig .6). Because the shear stress components are related by $\sigma_{xz} = -\sigma_{zx}, \sigma_{xy} = -\sigma_{yx}, \sigma_{yz} = -\sigma_{zy}$, only three of the four stress components in 2D coordinate system (x, y) are independent – $\sigma_{xx}, \sigma_{yy}, \sigma_{xy}$ (in 3D space six of nine components of the stress tensor are independent).

$$\sigma = \begin{bmatrix} \sigma_{11} & \sigma_{12} & \sigma_{13} \\ \sigma_{21} & \sigma_{22} & \sigma_{23} \\ \sigma_{31} & \sigma_{32} & \sigma_{33} \end{bmatrix} = \begin{bmatrix} \sigma_{xx} & \sigma_{xy} & \sigma_{xz} \\ \sigma_{yx} & \sigma_{yy} & \sigma_{yz} \\ \sigma_{zx} & \sigma_{zy} & \sigma_{zz} \end{bmatrix} = \begin{bmatrix} \sigma_x & \tau_{xy} & \tau_{xz} \\ \tau_{yx} & \sigma_y & \tau_{yz} \\ \tau_{zx} & \tau_{zy} & \sigma_z \end{bmatrix}$$

A stress ellipse in 2D (ellipsoid in 3D) is used for graphical representation of the stress state on all possible orientations of plane through a point. The orientation of major and minor axis of the stress ellipse represent the principle axis and their magnitude – the principle stresses $\sigma_1 \geq \sigma_3$. The stress tensor in principle coordinates has only diagonal entries, because the shear stress on principle planes is zero. In 3D the state of stress at a point can be described by the three principle stress $\sigma_1 \geq \sigma_2 \geq \sigma_3$ and their orientations (principle axis).

3.3 Fracture criteria

Experiments on brittle failure of rock samples reveal two type of fractures: extension fractures and shear fractures. For extension fractures, the frac-

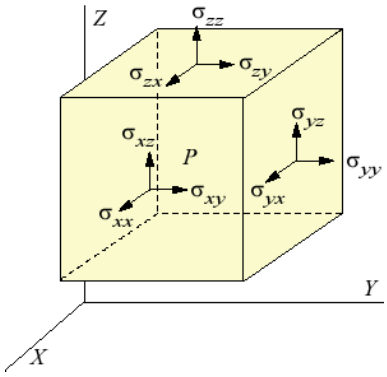

Figure .6: Stress tensor.

ture plane is perpendicular to the minimum principal stress σ_3 and parallel to the maximum principal stress σ_1. Extension fractures can form as tension fractures during uniaxial tension ($\sigma_1 = \sigma_2 = 0 > \sigma_3$), by longitudinal splitting during uniaxial compression ($\sigma_1 > \sigma_2 = \sigma_3 = 0$), or under conditions of extensional stress ($\sigma_1 = \sigma_2 > \sigma_3 > 0$). For each rock type there is a characteristic values of tensile stress T_0 at which tension fracturing occurs. A tension fracture forms on any plane in the material on which the normal stress reaches tensile strength $\sigma_n = T_0$, and the fracture plane is perpendicular to the maximum tensile stress σ_3.

Initiation of fracturing depends on the differential stress:

$$\sigma^{dif} = \sigma_1 - \sigma_3.$$

The magnitude of σ^{dif} necessary to cause shear fracture increases with increasing confining pressure. Shear fractures form under confined compression ($\sigma_1 > \sigma_2 = \sigma_3 > 0$) at angles around 30 ° to the maximum compressive stress σ_1 with displacement parallel to the fracture surface. Whenever the state of stress in the rock is such that on a plane of some orientation the surface stress components (σ_n, σ_s) satisfy $\sigma_s^* = c + \mu\sigma_n$ (Coulumb fracture criterion), where μ is coefficient of internal friction and c is cohesion, that plane can become a shear fracture.

Coulomb failure criterion is applicable to the rocks fracturing at around 100m-1km depth. With increasing depth and confining pressure transition from brittle to ductile behaviour occurs. Ductile deformation begins at

a critical shear stress, yield stress, which is independent of the confining pressure (von Mises criterion).

3.4 Griffith cracks

Fractures typically nucleate at the weaker sites in the material: microcracks, voids and disorder. The importance of defects and fluctuations in material properties was first investigated in the work of Griffith in 1920 [19]. A precursor to the Griffith study was the work by Inglis (1913) [20], who considered an isolated elliptical crack in an elastic plate subjected to externally applied stress (Fig .7A). It was shown that the stress at the crack tip σ_c was several times as large as the applied load σ_A depending on the sizes of the small axes of the crack, b, and large, c: $\sigma_c/\sigma_A \simeq 2c/b$. This ratio is called stress concentration factor – K. Thus, even small microcracks can be potential sources of weakness in the solid (Fig .7C). For the opening fracture mode the stress field around crack tip can be analysed as a plane strain (no displacement in the direction perpendicular to the plane) problem using the theory of elasticity (Westergaard, Muskhelishvili, Irwin) and can be expressed as (Fig .7B):

$$\begin{cases} \sigma_x = \frac{K}{\sqrt{2\pi r}} cos\frac{\Theta}{2}\left[1 - sin\frac{\Theta}{2}sin\frac{3\Theta}{2}\right] \\ \sigma_y = \frac{K}{\sqrt{2\pi r}} cos\frac{\Theta}{2}\left[1 + sin\frac{\Theta}{2}sin\frac{3\Theta}{2}\right] \\ \tau_{xy} = \frac{K}{\sqrt{2\pi r}} sin\frac{\Theta}{2}cos\frac{\Theta}{2}cos\frac{3\Theta}{2} \\ \sigma_z = \nu(\sigma_x + \sigma_y), \\ \tau_{xz} = \tau_{yz} = 0 \end{cases} \tag{.1}$$

3.5 Effect of pore fluid pressure

The presence of fluid causes a rock to behave as though the confining pressure were lower by an amount roughly equal to the pore fluid pressure. In the fracture criterion the normal stress is replaced by the effective normal stress $\sigma_n^{eff} = \sigma_n - p_f$. The stress state can become unstable if the pore pressure is sufficiently high. If the differential stress $\sigma^{dif} = \sigma_1 - \sigma_3$ is small,

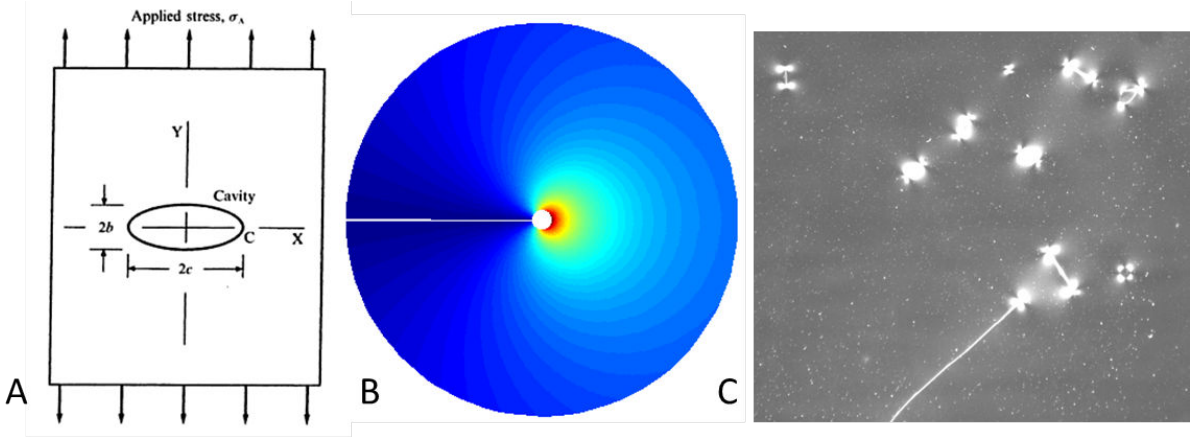

Figure .7: **A)** Plate containing elliptical crack, with semi-axis b, c, subjected to uniform applied tension, C denotes crack tip. **B)** Stress field around crack tip (Eq. .1). **C)** Fracture pattern in linear polarized light. Stress filed around crack tips is not symmetrical due to linear polarization of light.

which is commonly the case in the Earth, and pore pressure exceeds the minimum compressive stress σ_3 by an amount equal to the tensile strength of the rock, then extensional fracturing can occur, even at great depths. If the differential stress is large, shear fracturing can occur.

3.6 Hydraulic fracturing in nature

The usual origins of pore fluid are water incorporated into a sediment during deposition and fluids released from minerals by dehydration reaction during metamorphism. During metamorphic reactions in the Earths crust large quantities of fluids can be generated and released by the formation of hydraulic fractures [21]. Hydrofracturing generates permeable pathways for expelled fluids at different scales from microscopic to the regional scale. For example, partial melting of minerals occurs at the microscale [22, 23] (Fig .8A), whereas magma emplacement, formation of sills and rapid heating of either water (phreatic explosions) or the rocks and the organic matter it contains, may lead to the explosive release of fluids, on the kilometer scale or greater [24] (Fig .8B). In the current work we study crack formation in the organic-rich shale during decomposition of high-molecular kerogen

into lighter hydrocarbons, which happens at microscale, and fracturing of elastic gels during internal gas generation occurring at decimeter scale.

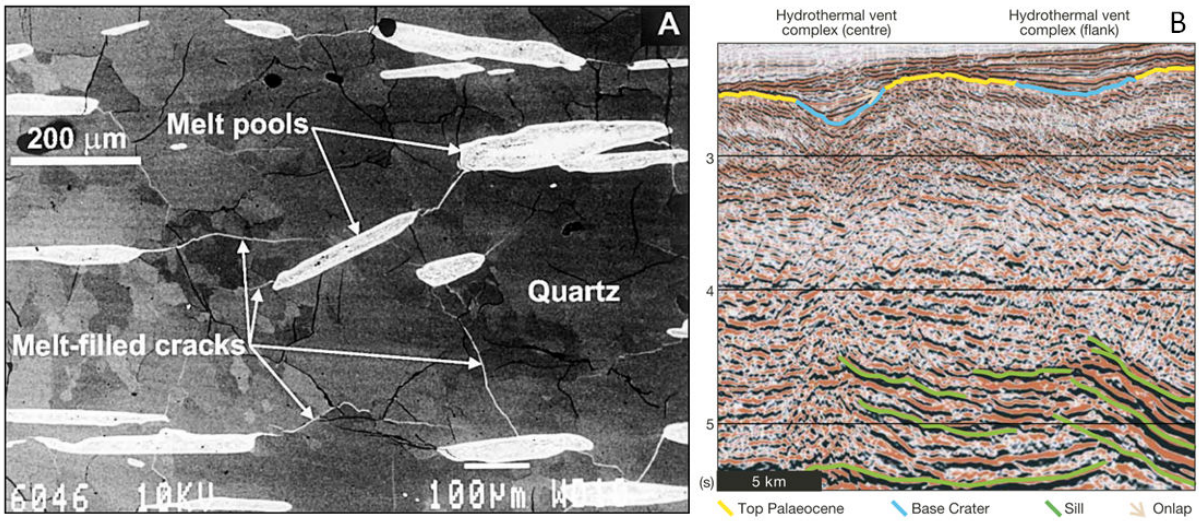

Figure .8: **A)** After [22]: Scanning back-scattered-electron microscopy image of cracks and melt pools of muscovite and quartz melting. **B)** After [24]: Seismic image of hydrothermal vent complexes, formed by explosive release of fluids after heating of organic-rich rock by sill intrusion.

3.7 Imaging

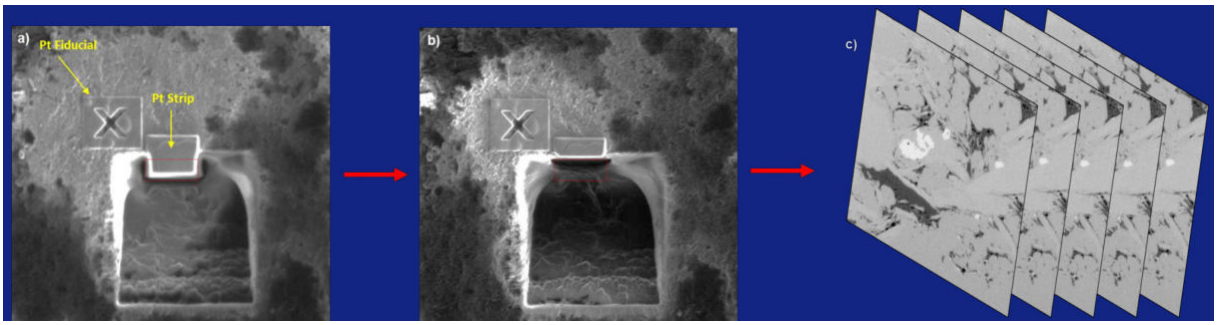

Figure .9: After [25]: Focused ion beam milling of 10nm thick layers to capture SEM images and reconstruct 3D shale microstructure.

Quantitative information about the evolution of microcracks is essential for the proper characterization of microscopic and macroscopic transport

phenomena in the tight rocks. The imaging techniques and the data processing are constantly improving, and at present several methods are available which allow a high resolution study of the pore structure. SEM (Scanning Electron Microscopy) [25], TEM (Transmission Electron Microscopy) and XRF (X-ray Fluorescence Imaging) are commonly used to obtain 2D images of planar cuts through 3D objects at micron and sub-micron scales. However these methods have some limitations. First, constructing a 3D image of a sample from multiple 2D micrographs is very untrivial and can not reproduce all the sample heterogeneities since the information on the pore structure between the 2D sections is missing. Second, repositioning of a sample after removing it for preparation of a new surface or a thin layer may be very challenging, because to prevent distortion in the final 3D image each 2D image needs to have exactly the same orientation and lateral position. A modification of the SEM method, focused ion beam scanning electron microscopy (FIB-SEM), which has recently been used to obtain 3D images of shales and mudstones (Fig .9) is free from both of the problems and is capable of constructing 3D images on very small scales. In this method a focused ion beam is used to mill/cross-section the sample without moving it, and an SEM image is obtained, again without moving the sample after each new surface has been prepared by the ion beam. However, all four methods mentioned above can not be used for a direct monitoring of the evolution of the structure of a sample over time (under changing or constant conditions). Finally, in the process of preparation of thin layers or flat surfaces the original sample is inevitably destroyed. These are the reasons why the X-ray micro-computed tomography, a non-destructive technique with somewhat lower resolution compared to FIB-SEM, was utilized in this study.

3.8 3D computed tomography

X-ray computed axial tomography is a non-intrusive technique for investigating the internal structure of diverse objects including rock samples. This technique is based on attenuation of X-rays in the material with dif-

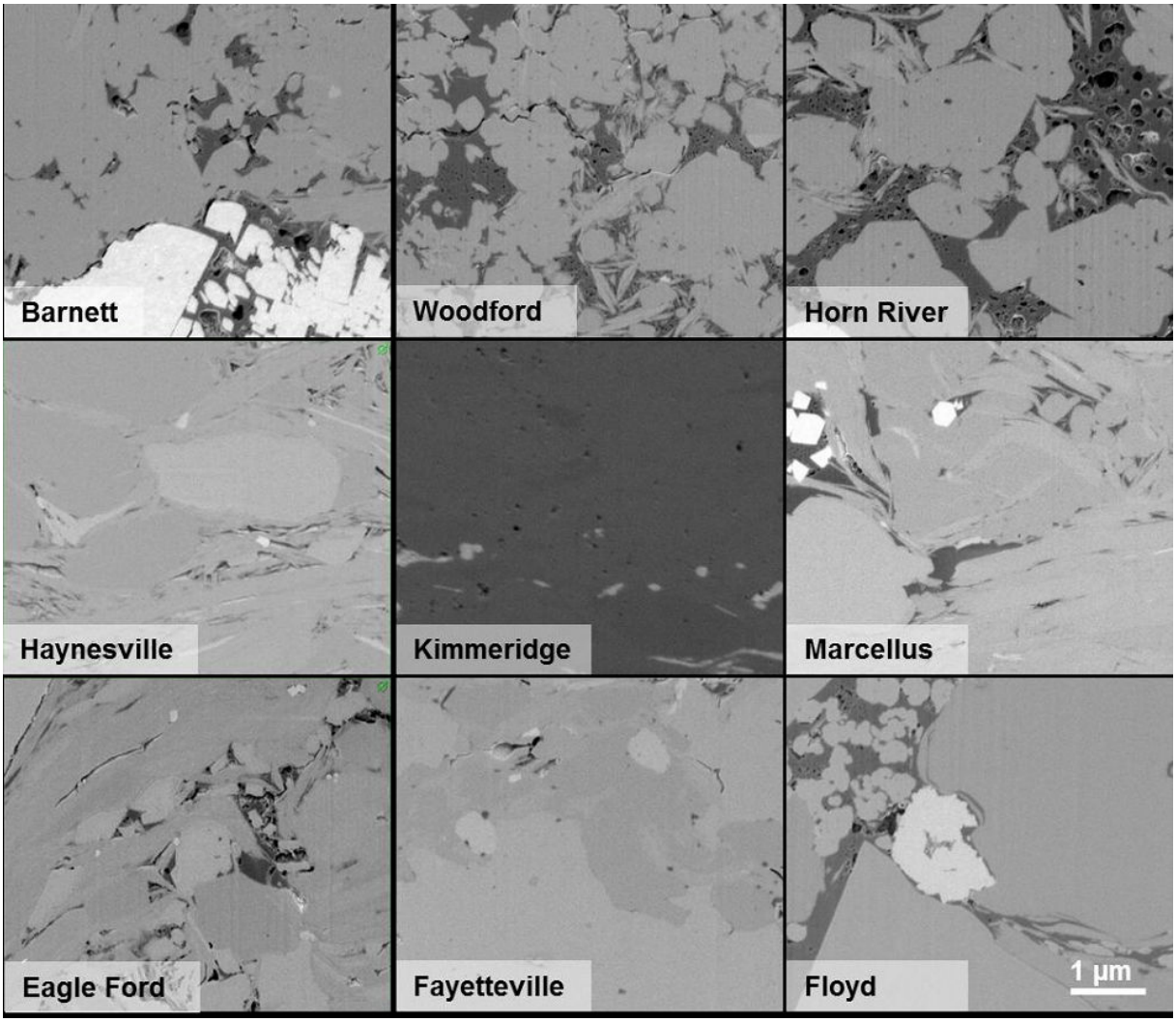

Figure .10: After [25]: SEM images of different shale rocks from the shale fields, which are potentially interesting for exploration.

ferent electron densities. The 3D image of the grain structure and pore network of a rock sample is a map of the linear attenuation coefficients. As an X-ray beam passes through material, it is attenuated following Beers law: $dI/dx = -\mu(x)$, where x is the position along the x-tay beam and $\mu(x)$ is the attenuation coefficient at position x.

2D radiographs are acquired by step-wise rotation of the sample and recorded by CCD camera. A mathematical algorithm reconstructs the horizontal cross-sections, which are perpendicular to the rotation axis and a 3D image is constructed from these cross-sections.

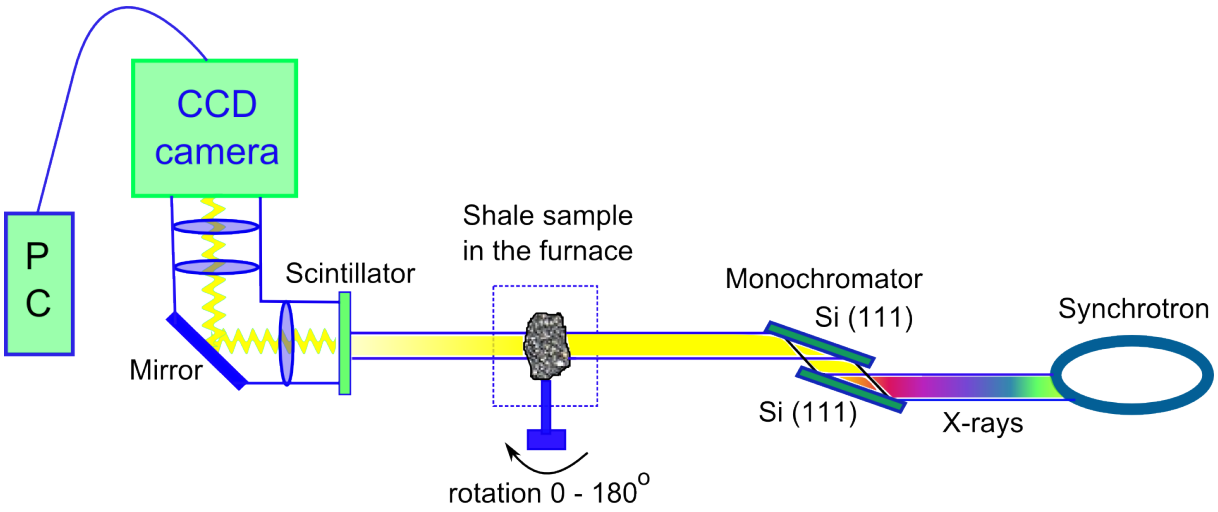

Figure .11: Synchrotron tomography setup.

The data presented in this thesis were acquired at European Synchrotron Radiation Facility (ESRF) at the tomographic beamline ID19 in Grenoble, France. The synchrotron X-ray radiation is emitted when high-energy electrons are forced to bend by a magnetic field. The advantage of this source is the high photon flux, which allows high-resolution images (less than 1 μm) to be obtained even for highly absorptive materials such as rocks. The collimation of the X-ray beam and usage of silica crystal monochromators (Fig .11) improves the accuracy of reconstructed images and eliminates the complications caused by energy dependent X-ray absorption.

When the high flux synchrotron X-ray is combined with a high-speed detector (CCD camera), the projections can be acquired with a speed that

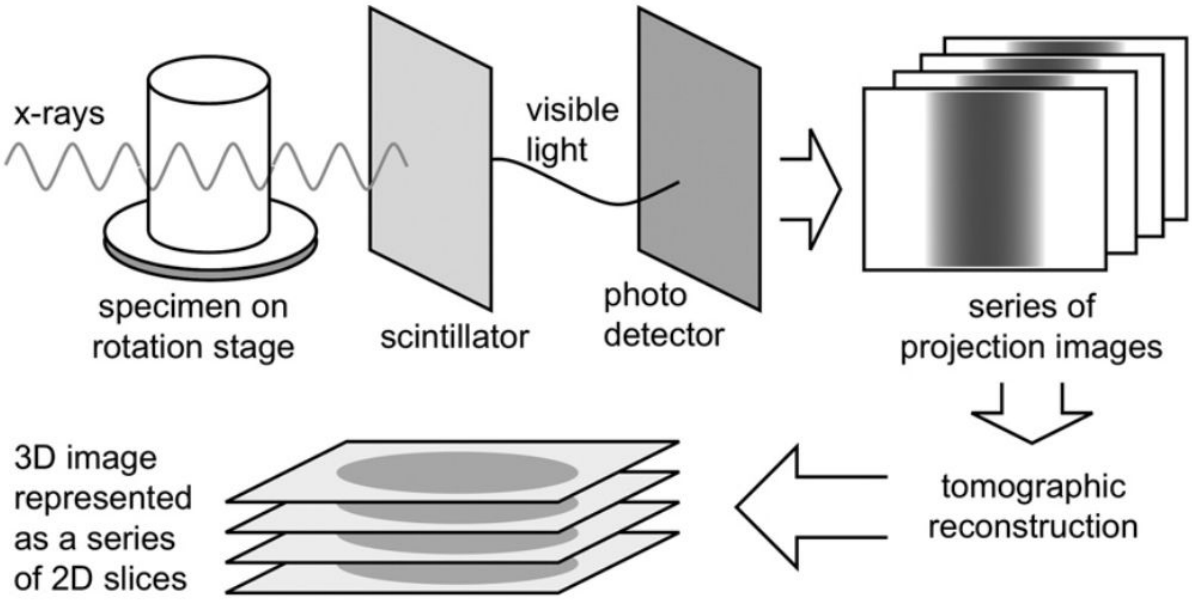

Figure .12: After [26]: Illustration of the computed tomography acquisition and reconstruction processes. A series of X-ray projection images is acquired and mathematically reconstructed to produce a 3D map of X-ray absorption in the volume. The 3D map is typically presented as a series of 2D slice images.

makes it possible to image changes of the rock structure over time. The combination of in-situ temperature control or loading devices with time-resolved imaging provides the opportunity of studying geophysical processes in close to reality situations. For example [27] observed the dehydration of gypsum during *in-situ* heating in a X-ray transparent furnace installed at the Advanced Photon Source (USA). With a spatial resolution of 2.2 μm^3 they traced the position, volume, shape and orientation of pores in gypsum over the duration of the experiment with a time resolution of 25 minutes per one 3D scan.

A part of this thesis presents an X-ray tomography investigation of fracturing process in organic-rich shale subjected to heating. Fig .13 shows the experimental *in situ* setup at tomographic beamline ID19, ESRF. A cylindrical shale sample was glued on a ceramic stick, installed on a rotating platform and placed in an X-ray transparent furnace. The voxel size of acquired volumes is 5×5×5 μm^3 and one 3D image was obtained in 11–14 minutes.

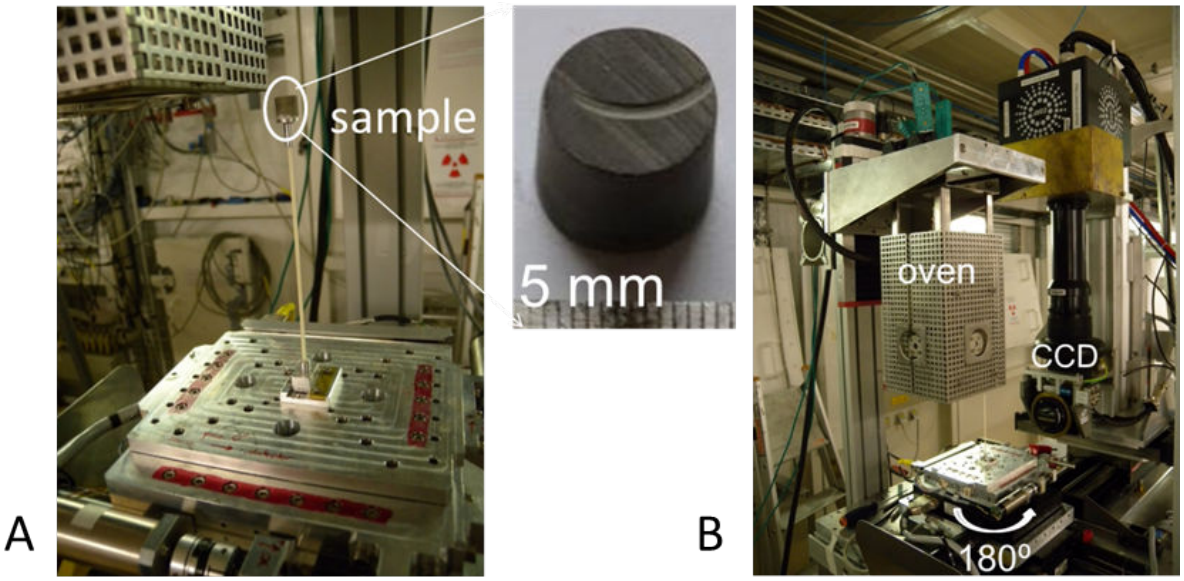

Figure .13: **A)** A shale sample installed on the rotating platform for tomography scanning. **B)** X-ray transparent oven at tomography beamline ID19, ESRF.

3.9 Image analysis of 3D data sets

In order to distinguish the pore structure and minerals a good contrast of the grey-level intensity in 3D volume is needed. The X-ray absorption of rock matrix is sufficiently different from air and water/hydrocarbons, and this allows good quality high resolution images to be obtained. Minimization of noise and artifacts is also crucial, and a suitable reconstructing algorithm is needed to reduce noise and artefact. Different software and algorithms are used to analyse 3D images. In [28] a skeletonisation technique available in Avizo software was used in order to investigate the connectivity of segregated melts. The work [29] used a distribution of labelled connected components to analyse shape and orientation of micro-racks in the rock volume. In the present study we investigated the nucleation, growth and interaction of cracks during thermal alteration of organic-rich shale. For this task the shape, size, spatial orientation and fracture roughness were characterized. The software package Avizo Fire was used to develop the image processing scheme.

4 Analogue experiment

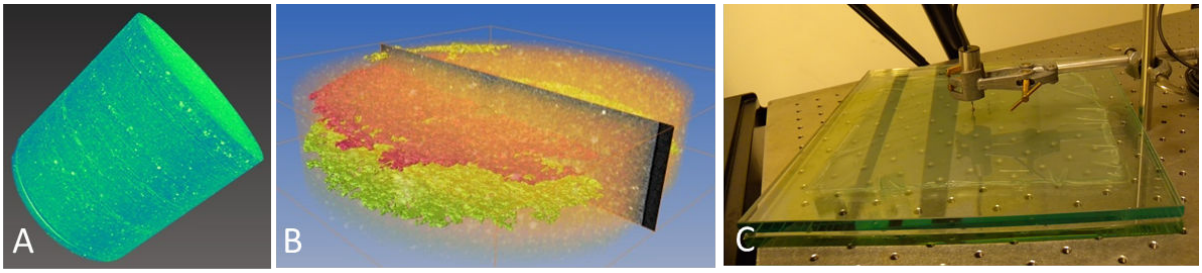

Figure .14: **A)** 3D tomographic image of the fractured shale sample. Cracks are distributed perpendicular to the cylinder axis. **B)** A fractured shale layer. Cracks are confined between the shale lamination. **C)** Fractured gelatine layer confined between two glass plates. The LVDT device was used to measure vertical displacement during fracturing.

Obtaining quantitative information about the coupling between fluid pressure build-up in the solids and the fracturing processes requires visual-

ization. The combination of *in situ* 3D imaging techniques, such as X-ray micro-tomography, with various thermodynamic conditions (temperature, pressure) remains challenging. For example, in the work of Fusseis [27] the dehydration of a gypsum sample was imaged *in situ*, but the heating reaction had to be suspended during 3D image acquisition, which led to the partial cooling of the sample. The imaging of microcracks forming during heating of shales [30] was performed *in situ* in 4D (time+space), but without desirable confinement of the sample. In such studies, obtaining a good time and spatial resolution, under the thermodynamic conditions at which the process occurs, is technically challenging. The micro-tomography technique does not allow ultrafast acquisitions for rock samples because of their high absorption of X- rays. In the experiment with shale sample [30] the acquisition time of 11–14 minutes allowed 3D images with a 5μm pixel size to be obtained, whereas in the gypsum dehydrating experiment the 3D volumes were recorded with 1.3μm spatial resolution during 25 minutes per scan. At ultra high resolution 0.7μm, 3D images of the melt distribution were obtained in a study of the generation of magmatic melt in oceanic olivine-rich rocks [28], but the processes was not recorded over time. In addition, in investigations of hydrocarbons generation, the imaging of organic matter in source rocks is more complicated than imaging of the mineral phase. Organic material has a small X-ray absorbtion coefficient μ and on a tomographic image it is not easily distinguished from the pore space.

To study fracture formation processes, experiments using materials analog to rocks are widely used [31, 32]. In the analogue experiments the thermodynamic conditions can be varied more easily and this allows the processes of fracturing to be followed at high time and spatial resolutions. In this study the gas exsolution fracturing of a gelatine layer confined between two glass plates was used as an analog for formation of a fracture network in the organic-rich layer of shale subjected to heating (Fig .14B). The geometry and shape of the fractures in the shale is different from the gelatine cracks, because the shale matrix is heterogeneous, whereas gelatine is essentially homogeneous (Fig .15). However, the basic physical principles which govern the fracture formation process in the analogue medium and

the real rock sample are similar. A chemical reaction with volume increase leads to the formation of hydrofractures in both gelatine and rock samples. The shale sample expands in the direction perpendicular to the lamination (along cylinder axis) (Fig .14A). Digital Image Correlation (DIC) technique showed that the shale sample experienced abrupt vertical expansion right before fracturing. In the analogue experiment the inflation of the gelatine layer was measured by using LVDT (Omega Engineering) device (Fig .14C). During fracturing the gelatine layer expanded in the direction perpendicular to the Hele-Shaw plane.

Figure .15: Time-resolved process of fracture development in the gelatine layer.

5 Hydrofracturing by phase separation

The formation of fractures and fracture networks driven by the stresses generated by phase separation is a well known phenomenon. For example, the growth of crystals from supersaturated solutions in porous media generates a maximum normal stress (force of crystallization) given by $\sigma = k_B T \ln \beta / v_0$ if the crystal is large enough for surface energy effects to be ignored, where k_B is the Boltzmann constant, T is the absolute temperature β is the supersaturation and v_0 is the molecular volume in the crystal. The magnitude of the stress emerging from this mechanism can reach several tens of megapascals, and this is sufficient to severely damage building materials [33]. Similarly, the crystallization of ice in undercooled

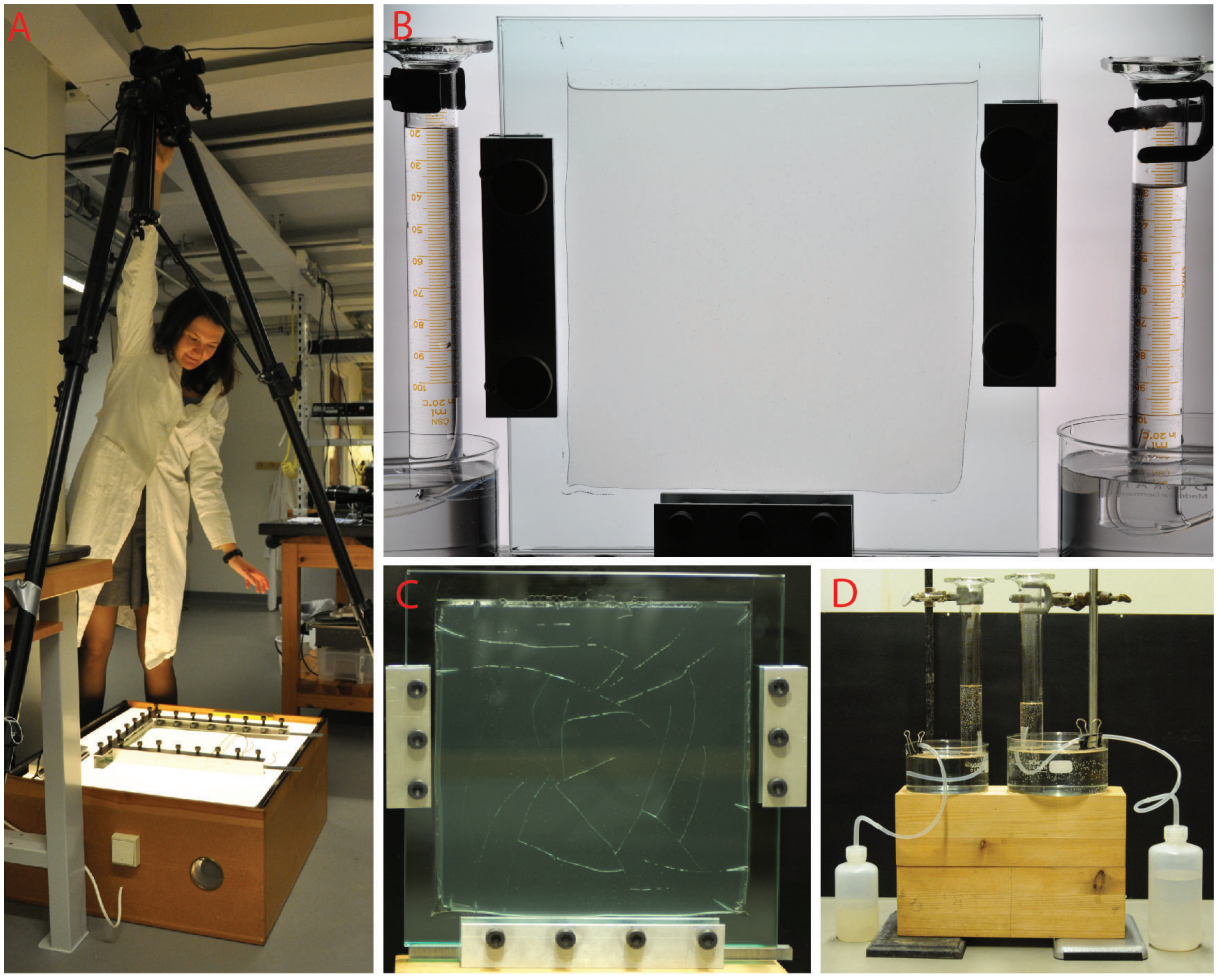

Figure .16: **A)** A light box was used to illuminate the Hele-Shaw cell from behind. A high-resolution camera Nikon D-300 was used to monitor fracture formation. **B)** *In situ* measurement of gas production during fracturing experiment. **C)** Hele-Shaw cell containing a fracturing layer of gelatine. **D)** Measurement of gas production rate. East mixed with sugar was dissolved in pure water (bottle on the right) and in gelatine solution (bottle on the left).

water can generate a maximum stress given by $\sigma = L\Delta T/v_0 T$, where L is the molecular latent heat of fusion and ΔT is the undercooling. Stresses of the order of 10 MPa can be generated in this way, which is also sufficient to drive stress corrosion cracking in rocks and seriously damage building materials via stress cracking corrosion [34]. Similarly, a gas bubble growing in unreactive liquids and some solids can generate a stress(pressure) given by $\sigma \approx k_H c$, where c is the concentration of the dissolved gas, and k_H is the Henry's law coefficient. At high concentrations, the pressure increases sublinearly with increasing concentration, and the maximum gas pressure is determined by the chemical potential of the dissolved gas and the temperature. If the bubble is small and/or the pressure is low $\sigma \approx k_H C - \Gamma\kappa$, where Γ is the surface tension and $\kappa = 1/r_1 + 1/r_2$ is the curvature (r_1 and r_2 are the principal radii of curvature). For high concentrations of dissolved gas stresses (pressures) of the order of 100 MPa can be generated [35, 36]. In some cases, pressures of several hundred MPa, sufficient to overcome the lithostatic pressure at depth up to about 10 km and drive bubble formation and fracturing in magmas and source rocks can be generated.

In liquids, the exsolution of gases generates spherical bubbles, in elastic solids, the exsolution of gases generates cracks, and in viscoelastic materials the shape of the gas filled void depends on the kinetics of exsolution. The formation of penny shaped cracks during the exsolution of gases in mud and other gel-like materials is well known [37, 38, 39]. When fluids are generated by phase separation, the transport of these fluids becomes important. Diffusion can play an important role on short length scales, but advective processes are dominant on larger length scales.

In a wide variety of natural systems fluid transport is focused onto a branched network of channels, and transport within the network plays an important role in its formation. For example, blood vessels have evolved to efficiently transport oxygen and carbon dioxide, the rapid transport of electric charge plays an important role in the formation of branched electric breakdown patterns such as lightning and the electrochemical growth of metal dendrites, the rapid flow of the low viscosity fluid is important in the formation of viscous fingers, and the transport of water, sediment

and sometimes dissolved minerals is important in the formation of river networks. In these systems, transport is driven by a potential gradient, which establishes a preferential direction for growth, and the resulting directed tree networks have characteristic fractal geometries and statistical properties [40, 41, 42, 43, 44, 45, 46]. In the case of river networks, it has been argued that the planform of the river [47] and the associated topography [48, 44] minimize energy dissipation in the river channel network. The key mechanisms of branched river formation are erosion of the landscape and transport of sediment to and along the river channels. The transport is *long ranged* but one-directional (from high to low elevation and towards the "root" of the topologic tree), and flow mediated interaction between one location and another does not extend beyond the local drainage basin that contains both locations [46]. Minimum Energy dissipation concepts can also be applied to biological branched networks such as vascular trees [49]. In this case, an optimization approach can be based on Darwinian evolution instead of the quasi thermodynamic (entropy production) ideas often used for other branched networks.

The statistical description of fractures [50] has only recently been extended to fracture network topology [51], and theoretical, computational and experimental investigations of fluid transport in fracture networks [52, 53] are usually based on a preexisting fracture network. Even if fluid pressure in fractures is increased only locally the interactions are *long ranged* through elasticity of the solid and pressure transport in the fracture apertures. In the subsurface, the formation of fracture networks and the expulsion of fluids through them, driven by the separation of dissolved fluids such as water and carbon dioxide from solid rocks and magmas is an important and ubiquitous phenomenon. Similarly the generation of fluids by the thermal decomposition of carbonates, the dehydration of hydrates and other chemical reactions leading to fracturing and expulsion of the fluids is also very common. Gravitational (buoyancy) effects, particularly on large scales, may drive fluids upwards through fractures and fracture networks, and this is important in rock compaction and the cycling of carbon dioxide, water and other substances.

Although the work presented in this paper is basic in its nature, it is relevant to several phenomena that have a large societal and/or economic impact. Kvalstad [37] investigated the fracturing of transparent Laponite (synthetic hectorite clay) gels by the exsolution (phase separation) of air and CO_2, and the formation of gas escape routes. In this work, experiments were conducted by dissolving the gas under pressure in the gel, which filled a cylinder, for several weeks, and then reducing the pressure. This work was conducted as part of an investigation of the weakening of fine grained sea floor sediments by crack-like methane bubbles generated by biological methanogenesis and/or the decomposition of methane hydrate. This may be an important triggering mechanism for submarine mud slides, such as the $3,000$ km^3 Storegga slide, which are capable of destroying offshore oil and gas facilities and driving tsunamis.

The formation and migration of fission gas bubbles in nuclear fuels plays an important role in the swelling and deformation of nuclear fuels as well as the release of fission products [54], and bubble formation may also play a role in microcrack formation. These processes have an important impact on fuel burnup (the amount of heat that can be generated before the fuel must be removed) and safety.

The work reported in the thesis was motivated primarily by the interest in the natural hydraulic fracturing and fracture healing that occurs when oil and gas are generated during the thermal decomposition of organic matter (kerogen) in very low permeability sedimentary rocks [30]. The catagenic formation of hydrocarbon fluids in source rocks and its expulsion from the source rock (primary migration) is important because it is an essential step in the filling of all conventional oil reservoirs. Primary migration is still poorly understood after many decades of investigation, but natural hydraulic fracturing, and expulsion of oil via fractures is believed to play a key role [55, 56, 57]. Bubble formation, fracturing and fragmentation, driven by the exsolution of dissolved gases, plays a key role in explosive volcanism [35, 36], which is important because it is a major geohazard and because it injects large amounts of particles and gases [CO_2, HCl, SO_2, etc.], which have significant environmental impacts, into the atmosphere.

Fluid generation, hydraulic fracturing by the generated fluid and fluid expulsion via fractures is also important in the retorting of oil shale to produce oil and gas. Hydraulic fracturing (the injection of fluids into rocks to create fracture networks and increase the recovery of hydrocarbon or the injectability of waste products) is now being used on a very large scale. Hydraulic fracturing for the recovery of gas and oil from "shales" has become a topic of great public interest. Other applications include recovery of conventional oil, recovery of coalbed methane and tight gas, sequestration of CO_2, disposal of produced water and chemical waste, solution mining, recovery of water from aquifers.

In this thesis experiments are described that were conducted to investigate exsolution driven fracturing and degassing in a model system – a horizontal Hele-Shaw cell filled with a gel in which CO_2 is generated via the fermentation of sucrose – with the objective of contributing to a better understanding of the generic aspects of the growth of fractures and fracture networks driven by fluid generation or injection. The model system was designed to retain the processes that are common to essentially all natural systems of this type and enable a detailed investigation of the dynamics of fluid driven fracturing in a system that is as simple as possible. To this end, an elastic medium was selected that is homogeneous on all but very small length scales (to eliminate the effects of multiscale heterogeneity), and weak (to eliminated the experimental challenges associated with high stresses). The transparent two-dimensional nature of the experimental setup facilitated detailed imaging of fracture growth, opening, closing and healing, and the slow generation of CO_2 facilitated investigation of the dynamics of the system via high resolution digital image analysis. The fracture/drainage networks that developed during the experiments were intermediate between branched river network, which have essentially no loops (and no loops at all in modes river network models) and hierarchical fracture network, which is dominated by loops. Drainage networks of this type have been discussed in the scientific literature as networks with suboptimal transport efficiency [40]. Fracture opening and closing, which affects the flow of CO_2 in the fracture network like a valve, was observed. Similar

behavior is believed to occur in a variety of fluid generating subsurface systems, which cannot be directly observed. It is assumed that adhesion between the gel and the Hele-Shaw cells walls has an effect similar to compressive (overburden) stress, and the quasi two-dimensional experiments are relative to three dimensional systems such as oil and gas source rocks undergoing hydrocarbon generation and expulsion (primary migration).

6 Overview and contribution to the papers

This thesis presents background, work and results of a number of laboratory experiments on natural rock samples and analogue materials, as well as analysis of experimental results in two and three dimensions. The first two papers concentrate on time-resolved 3D imaging experiment with natural rock samples. Paper 1 explains the geological origin and mineralogical composition of the shale sample used in the experiments and the processes underling fracture formation upon heating and organic matter decomposition in the sample. Paper 2 gives an overview of the experimental procedure and image analysis workflow, which were used to obtain results presented in the first paper. The other two papers are based on analogue experiments conducted using brittle gelatin gels. Paper 3 describes an investigation of the mechanism of fracture network formation during draining of CO_2 out of a gelatine layer. Paper 4 focuses on the temporal evolution of the drainage network and the mechanism of fracture opening and closing. Finally Paper 5 presents a study in which X-ray microtomography was used to characterize porosity distribution in weathered rock samples.

During my PhD study I participated in two synchrotron micro-tomography experiments at ESRF (Grenoble, France) in 2009 and 2012 (72 hours duration each), together with my supervisors Dag Kristian Dysthe and François Renard, and PhD student Hamed Panahi. In 2009 I took part in the experiment and was processing the obtained data. In 2010 I participated in the application for beamtime, sample preparation and development of experimental set-up, as well as conducting experiment and processing of

acquired data. In March 2010 I followed five weeks of HERCULES course (Higher European Research Course for Users of Large Experimental Systems), organized by University Grenoble 1 and providing training in the field of Neutron and Synchrotron Radiation for condensed matter studies. In April 2010 I participated in a three days course organized by Visualization Sciences Group company, which provided training in analysis of 3D tomographic images of rocks using the commercial software Avizo Fire. During this course we were suggested an example workflow for processing 3D images of shale core samples, acquired during ESRF experiment in 2009. I developed further and adapted this workflow in application to 3D time-resolved image sequence acquired during heating of organic-rich shale. Based on the results obtained I wrote one paper and contributed to another one (paper 1 and 2). Also I participated in developing two experiments based in the University of Oslo laboratory. First, I contributed to installation and testing of high pressure autoclaves with the goal to measure pressure variation during heating of organic-rich shale samples. Second, I built an analogue experiment to simulate fracture formation during gas production in elastic media. Based on the last experiment I wrote two papers (paper 3 and 4). I also was involved in collaboration with geologists. I contributed to studying pore structure in andesite rocks using X-ray micro-tomography (paper 5).

Paper 1. This paper is based on the results obtained in the ESRF experiment in 2009. My part was to perform all 3D image analysis and process the image sequence obtained during heating of the shale sample in tomographic experiment using Avizo Fire software, as well as analysis of the processed images, measurements of fracture area and other characteristics of 3D fracture pattern using Matlab and ImageJ. With the help of my supervisors, I prepared all the figures, provided data interpretation and discussion, wrote the article. Image correlation analysis and numerical simulation was suggested by the co-authors, but I actively participated in interpretation of the results, connection to the experiment and discussion.

Paper 2. This paper is based on the results obtained in the ESRF experiment in 2009. My input was 3D image analysis of the image sequence

obtained during heating of the shale sample in tomographic experiment using Avizo Fire software.

Paper 3. My contribution to this work was to build the experimental device to study the fracture formation process in a gelatine media during CO_2 generation by yeasts, as well as develop measurement techniques to document the fracture propagation, healing and coalescence during gas flow out of the fractures. I also developed complementary experiments used to measure gas production, Hele-Shaw cell deformation and other parameters. I performed all experiments described in the paper, created image analysis workflow, processed all the images, videos and other experimental data and performed statistical data treatment. The modelling part was performed with the help of my co-authors. I prepared all the figures and wrote the article.

Paper 4. This paper is based on the same experiments as paper 3. I developed data analysis workflow, performed statistical data treatment, interpretation of the results and discussion. I prepared all the figures and wrote the article. The numerical section is a contribution of the co-authors.

Paper 5. My contribution to this paper was to develop 3D image analysis workflow to process X-ray tomography images of porosity in andesite samples. I also analyzed pore size distribution data and prepared Figures 6 and 7.

Bibliography

[1] Bjørn Jamtveit and Håkon Austrheim. Metamorphism: The role of fluids. *Elements*, 6(3):153–158, 2010.

[2] James A. D. Connolly. The mechanics of metamorphic fluid expulsion. *Elements*, 6(3):165–172, 2010.

[3] J. A. D. Connolly and Yu Yu Podladchikov. Compaction-driven fluid flow in viscoelastic rock. *Geodinamica Acta*, 11(23):55–84, 1998.

[4] E. G. Flekkoy, A. Malthe-Sorenssen, and B. Jamtveit. Modeling hydrofracture. *Journal of Geophysical Research-Solid Earth*, 107(B8), 2002.

[5] G. G. Lash and T. Engelder. An analysis of horizontal microcracking during catagenesis: Example from the catskill delta complex. *Aapg Bulletin*, 89(11):1433–1449, 2005.

[6] Ulrich Mann. An integrated approach to the study of primary petroleum migration. *Geological Society, London, Special Publications*, 78(1):233–260, 1994.

[7] B. Durand. Understanding of hc migration in sedimentary basins (present state of knowledge). *Organic Geochemistry*, 13(13):445–459, 1988.

[8] P. Ungerer. State-of-the-art of research in kinetic modeling of oil formation and expulsion. *Organic Geochemistry*, 16(1-3):1–25, 1990.

[9] L. C. Price. Primary petroleum migration from shales with oxygen-rich organic-matter. *Journal of Petroleum Geology*, 12(3):289–324, 1989.

[10] J. G. Stainforth and J. E. A. Reinders. Primary migration of hydrocarbons by diffusion through organic-matter networks, and its effect on oil and gas generation. *Organic Geochemistry*, 16(1-3):61–74, 1990.

[11] W. A. England, A. S. Mackenzie, D. M. Mann, and T. M. Quigley. The movement and entrapment of petroleum fluids in the subsurface. *Journal of the Geological Society*, 144:327–347, 1987.

[12] E. I. Sandvik and J. N. Mercer. Primary migration by bulk hydrocarbon flow. *Organic Geochemistry*, 16(13):83–89, 1990.

[13] X. Cui, A. M. M. Bustin, and R. M. Bustin. Measurements of gas permeability and diffusivity of tight reservoir rocks: different approaches and their applications. *Geofluids*, 9(3):208–223, 2009.

[14] Robert R. Berg and Anthony F. Gangi. Primary migration by oil-generation microfracturing in low-permeability source rocks; application to the austin chalk, texas. *AAPG Bulletin*, 83(5):727–756, 1999.

[15] R. M. Capuano. Evidence of fluid-flow in microfractures in geopressured shales. *Aapg Bulletin-American Association of Petroleum Geologists*, 77(8):1303–1314, 1993.

[16] T.L. Anderson. *Solutions Manual for Fracture Mechanics: Fundamentals And Applications*. Taylor & Francis Group, 2006.

[17] D. Broek. *Elementary Engineering Fracture Mechanics*. Springer, 1982.

[18] J.C. Jaeger, N.G.W. Cook, and R. Zimmerman. *Fundamentals of Rock Mechanics*. Wiley, 2009.

[19] A.A. Griffith. *The Phenomena of Rupture and Flow in Solids*. Proceedings of the Royal Society of London, 1920.

[20] B. Lawn. *Fracture of Brittle Solids*. Cambridge University Press, 1993.

[21] W.S. Fyfe, N.J. Price, and A.B. Thompson. *Fluids in the earth's crust: their significance in metamorphic, tectonic, and chemical transport processes*. Elsevier Scientific Pub. Co., 1978.

[22] J. A. D. Connolly, M. B. Holness, D. C. Rubie, and T. Rushmer. Reaction-induced microcracking: An experimental investigation of a mechanism for enhancing anatectic melt extraction. *Geology*, 25(7):591–594, 1997.

[23] F. Renard, P. Ortoleva, and J. P. Gratier. Pressure solution in sandstones: influence of clays and dependence on temperature and stress. *Tectonophysics*, 280(3-4):257–266, 1997.

[24] H. Svensen, S. Planke, A. Malthe-Sorenssen, B. Jamtveit, R. Myklebust, T. R. Eidem, and S. S. Rey. Release of methane from a volcanic basin as a mechanism for initial eocene global warming. *Nature*, 429(6991):542–545, 2004.

[25] M.E. Curtis, J.A. Raymond, C.H. Sondergeld, and S.R. Chandra. Investigating the microstructure of gas shales by fib/sem tomography & stem imaging. In *Oklahoma Geological Survey, Meetings, Shales moving forward*, 2011.

[26] Eric N. Landis and Denis T. Keane. X-ray microtomography. *Materials Characterization*, 61(12):1305–1316, 2010.

[27] F. Fusseis, C. Schrank, J. Liu, A. Karrech, S. Llana-Funez, X. Xiao, and K. Regenauer-Lieb. Pore formation during dehydration of a polycrystalline gypsum sample observed and quantified in a time-series synchrotron x-ray micro-tomography experiment. *Solid Earth*, 3(1):71–86, 2012.

[28] W. L. Zhu, G. A. Gaetani, F. Fusseis, L. G. J. Montesi, and F. De Carlo. Microtomography of partially molten rocks: Three-dimensional melt distribution in mantle peridotite. *Science*, 332(6025):88–91, 2011.

[29] S. Zabler, A. Rack, I. Manke, K. Thermann, J. Tiedemann, N. Harthill, and H. Riesemeier. High-resolution tomography of cracks, voids and micro-structure in greywacke and limestone. *Journal of Structural Geology*, 30(7):876–887, 2008.

[30] Maya Kobchenko, Hamed Panahi, Franois Renard, Dag K. Dysthe, Anders Malthe-Srenssen, Adriano Mazzini, Julien Scheibert, Bjrn Jamtveit, and Paul Meakin. 4d imaging of fracturing in organic-rich shales during heating. *J. Geophys. Res.*, 116(B12):B12201, 2011.

[31] P. D. Bons and B. P. van Milligen. New experiment to model self-organized critical transport and accumulation of melt and hydrocarbons from their source rocks. *Geology*, 29(10):919–922, 2001.

[32] E. Di Giuseppe, F. Funiciello, F. Corbi, G. Ranalli, and G. Mojoli. Gelatins as rock analogs: A systematic study of their rheological and physical properties. *Tectonophysics*, 473(34):391–403, 2009.

[33] G. W. Scherer. Crystallization in pores. *Cement and Concrete Research*, 29(8):1347–1358, 1999.

[34] J. Walder and B. Hallet. A theoretical model of the fracture of rock during greezing. *Geological Society of America Bulletin*, 96:336–346, 1985.

[35] M. Mangan and T. Sisson. Delayed disequilibrium degassing in rhyolite magma: decompression experiments and implications for explosive volcanism. *Earth and Planetary Science Letters*, 183:441–455, 2000.

[36] M. T. Mangan, T. W. Sisson, and W. B. Hankins. Decomposition experiments identifying kinetic controls on explosive silicic eruptions. *Geophysical Research Letters*, 31:L08605, 2004.

[37] T. J. Kvalstad. Effect of gas hydrate dissociation on clay. In *1st National Workshop on Gas Hydrates and Natural Seeps in the Nordic Sea Region*, Trondheim, Norway, 2004.

[38] W. Soh. Computed tomography scan analysis of site 941 cores, western mass-transport deposit, amazon fan. In R. D. Flood, D. J. W. Piper, A. Klaus, and L. C. Peterson, editors, *Proceedings of Ocean Drilling Program Scientific Results*, volume 155, pages 465–474, 1997.

[39] B. P. Boudreau, C. Algar, B. D. Johnson, I. Croudace, A. Reed, Y. Furukawa, K. M Dorgan, P. A. Jumara, A. S. Grader, and B. S. Gardiner. Bubble growth and rise in soft sediment. *Geology*, 33(6):47–97, 2005.

[40] J. R. Banavar, A. Maritan, and A. Rinaldo. Size and form in efficient transportation networks. *Nature*, 399(6732):130–132, 1999.

[41] P. S. Dodds and D. H. Rothman. Geometry of river networks. i. scaling, fluctuations, and deviations. *Physical Review E*, 63(1), 2001.

[42] P. S. Dodds and D. H. Rothman. Geometry of river networks. ii. distributions of component size and number. *Physical Review E*, 63(1), 2001.

[43] P. S. Dodds and D. H. Rothman. Geometry of river networks. iii. characterization of component connectivity. *Physical Review E*, 63(1), 2001.

[44] A. Rinaldo, J. R. Banavar, and A. Maritan. Trees, networks, and hydrology. *Water Resources Research*, 42(6), 2006.

[45] Kyungrock Paik and Praveen Kumar. Emergence of self-similar tree network organization. *Complexity*, 13(4):30–37, 2008.

[46] Ilya Zaliapin, Efi Foufoula-Georgiou, and Michael Ghil. Transport on river networks: A dynamic tree approach. *Journal of Geophysical Research-Earth Surface*, 115, 2010.

[47] I. Rodriguez-Iturbe, A. Rinaldo, R. Rigon, R. L Bras, E. Ijjasz-Vasquez, and Alessandro Marani. Fractal structures as least energy patterns: The case of river networks. *Geophysical Research Letters*, 19(9):889–892, 1992.

[48] T. Sun, P. Meakin, and T. Josang. The topography of optimal drainage basins. *Water Resources Research*, 30(9):2599–2610, 1994.

[49] T. Sun, P. Meakin, and T. Josang. Minimum energy-dissipation fractal structures of vascular systems. *Fractals*, 3(1):123–153, 1995.

[50] Mikko J. Alava, Phani K. V. V. Nukalaz, and Stefano Zapperi. Statistical models of fracture. *Advances in Physics*, 55(3-4):349–476, 2006.

[51] C. A. Andresen, A. Hansen, R. Le Goc, P. Davy, and S. M. Hope. Topology of fracture networks. *arXiv:1203.4510*, 2012.

[52] M. Sahimi. Flow phenomena in rocks - from continuum models to fractals, percolation, cellular-automata, and simulated annealing. *Reviews of Modern Physics*, 65(4):1393–1534, 1993.

[53] B. Berkowitz. Characterizing flow and transport in fractured geological media: A review. *Advances in Water Resources*, 25(8-12):861–884, 2002.

[54] M. V. Speight R. M. Cornell and B. C. Masters. The role of bubbles in fission gas release from uranium dioxide. *Journal of Nuclear Materials*, 30:170–178, 1998.

[55] A. N. Snarsky. Relationship between primary migration and compaction of rocks. *Geology*, 5:362–365, 1961. Translated from Geologiya Nefti i Gaza.

[56] B. Tissot and D. H. Welte. *Petroleum formation and occurrence*. Springer, New York, 1978.

[57] I. Ozkaya. A simple analysis of oil-induced fracturing in sedimentary-rocks. *Marine and Petroleum Geology*, 5(3):293–297, 1988.

Scientific papers

Paper 1

4D imaging of fracturing in organic-rich shales during heating

Maya Kobchenko[1], Hamed Panahi[1,2], Franois Renard[1,3], Dag K. Dysthe[1], Anders Malthe-Sørenssen[1], Adriano Mazzini[1], Julien Scheibert[1,4], Bjørn Jamtveit[1], and Paul Meakin[1,5,6]

[1]Physics of Geological Processes, University of Oslo, Oslo, Norway.
[2]Statoil ASA, Oslo, Norway.
[3]Institut des Sciences de la Terre, Universit Joseph Fourier, CNRS, Grenoble, France.
[4]Laboratoire de Tribologie et Dynamique des Systmes, CNRS, Ecole Centrale de Lyon, Ecully CEDEX, France.
[5]Center for Advanced Modeling and Simulation, Idaho National Laboratory, Idaho Falls, Idaho, USA.
[6]Institute for Energy Technology, Kjeller, Norway.

Publication data:
Journal of geophysical research, Vol. 116, B12201, doi:10.1029/2011JB008565, 2011.

4D imaging of fracturing in organic-rich shales during heating

Maya Kobchenko,[1] Hamed Panahi,[1,2] François Renard,[1,3] Dag K. Dysthe,[1] Anders Malthe-Sørenssen,[1] Adriano Mazzini,[1] Julien Scheibert,[1,4] Bjørn Jamtveit,[1] and Paul Meakin[1,5,6]

Received 1 June 2011; revised 12 September 2011; accepted 16 September 2011; published 7 December 2011.

[1] To better understand the mechanisms of fracture pattern development and fluid escape in low permeability rocks, we performed time-resolved in situ X-ray tomography imaging to investigate the processes that occur during the slow heating (from 60° to 400°C) of organic-rich Green River shale. At about 350°C cracks nucleated in the sample, and as the temperature continued to increase, these cracks propagated parallel to shale bedding and coalesced, thus cutting across the sample. Thermogravimetry and gas chromatography revealed that the fracturing occurring at ∼350°C was associated with significant mass loss and release of light hydrocarbons generated by the decomposition of immature organic matter. Kerogen decomposition is thought to cause an internal pressure build up sufficient to form cracks in the shale, thus providing pathways for the outgoing hydrocarbons. We show that a 2D numerical model based on this idea qualitatively reproduces the experimentally observed dynamics of crack nucleation, growth and coalescence, as well as the irregular outlines of the cracks. Our results provide a new description of fracture pattern formation in low permeability shales.

Citation: Kobchenko, M., H. Panahi, F. Renard, D. K. Dysthe, A. Malthe-Sørenssen, A. Mazzini, J. Scheibert, B. Jamtveit, and P. Meakin (2011), 4D imaging of fracturing in organic-rich shales during heating, *J. Geophys. Res.*, *116*, B12201, doi:10.1029/2011JB008565.

1. Introduction

[2] A wide variety of geological phenomena involve the generation and migration of fluids in low permeability rocks. For example, dehydration of sediments in subduction zones generates large fluxes of water that rise along low-permeability subduction interfaces, and provide a mechanism for creep and/or slow earthquakes [*Obara*, 2002]. Similarly, the illitization of clays at depth and the production of methane in organic-rich shales were suggested to contribute to the development of overpressure and the formation of piercement structures, which are manifest on the surface as mud volcanoes [*Mazzini*, 2009]. Also, the emplacement of magmatic bodies into sedimentary basins induces rapid decomposition of organic matter, and the resulting gases migrate through low permeability rocks in quantities that may significantly alter the climate [*Svensen et al.*, 2004]. In all these geological systems, the migration of a fluid through low permeability rocks is coupled with deformation. This type of coupling between fluid flow and deformation is also important in the primary migration of hydrocarbons.

[3] Primary migration is the transport of hydrocarbon fluids from extremely low permeability source rocks, in which they are generated, to more permeable rocks through which they migrate to a trap (reservoir) or to the surface. This natural process is of both economic and fundamental interest. As the organic-rich fine grained sediment from which the source rock is formed is buried, the organic material is transformed into complex high molecular weight/cross-linked organic oil and gas precursors (kerogen). As the burial depth increases, the temperature and pressure rise, and kerogen decomposes into low molecular weight hydrocarbon fluids (gas and oil), which have much lower viscosities than the kerogen. The generated hydrocarbon fluids escape from the shale into secondary migration pathways, by processes that remain enigmatic, in spite of decades of investigation [*Bjørlykke*, 2010].

[4] Fracturing is commonly cited as a likely mechanism to increase the permeability of source rocks and provide pathways for the generated hydrocarbons [*Berg and Gangi*, 1999; *Lash and Engelder*, 2005]. During kerogen decomposition, generation of less dense fluids leads to pore pressure build-up, which may cause fracturing of the host rock. The presence of microcracks is commonly observed in thin sections of recovered source rock samples [*Capuano*, 1993; *Marquez and Mountjoy*, 1996; *Lash and Engelder*, 2005],

[1]Physics of Geological Processes, University of Oslo, Oslo, Norway.
[2]Statoil ASA, Oslo, Norway.
[3]Institut des Sciences de la Terre, Université Joseph Fourier, CNRS, Grenoble, France.
[4]Laboratoire de Tribologie et Dynamique des Systèmes, CNRS, Ecole Centrale de Lyon, Ecully CEDEX, France.
[5]Center for Advanced Modeling and Simulation, Idaho National Laboratory, Idaho Falls, Idaho, USA.
[6]Institute for Energy Technology, Kjeller, Norway.

0148-0227/11/2011JB008565

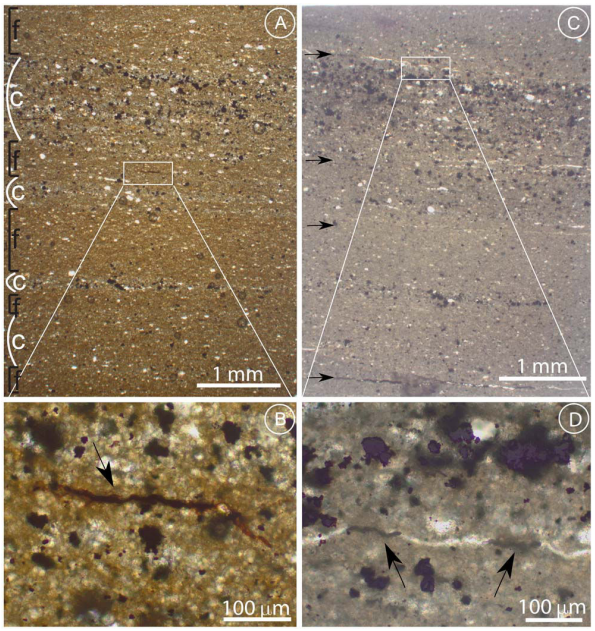

Figure 1. Thin section images of Green River Shale sample before and after heating. (a) Interlaminated silt and clay-rich layers before heating. Here f indicates clay-rich layers with a higher amount of kerogen lenses and c indicates coarser layers with siliciclastic grains. (b) Detail of a kerogen lens. (c) Image of the same sample after heating. Arrows indicate the position of cracks developed during heating. Fractures propagated mainly in the finer grained intervals where the highest concentration of organic matter lenses was also observed. (d) Detail of a crack filled with organic remains (arrows).

suggesting that microcracks may be involved in fluid migration.

[5] Under natural conditions, this fracture process takes place at depths of several kilometers over millions of years, making its monitoring impossible. Therefore, it is very important to construct adequate models of primary migration. Several theoretical and numerical studies of fracture formation in organic-rich shales have been described in the scientific literature [*Ozkaya*, 1988; *Jin et al.*, 2010]. *Jin et al.* [2010] introduced a fracture mechanics model of subcritical crack propagation and coalescence, based on the assumption of linear elastic behavior of the rock. Although the model provides an estimate of the fracture propagation time, the 3D geometry and mechanism of fracture formation in heterogeneous shale remain unclear.

[6] To better understand the complex phenomenon of hydrocarbon expulsion from very low permeability source rock, we employed a new experimental approach – real-time 3D X-ray tomography – during gradual heating of a shale sample coupled with thermogravimetry and petrography analyses before and after heating. This study included only unconfined samples, but it is an important step toward the goal of unraveling the numerous and complex mechanisms controlling primary migration.

2. Characterization of Green River Shale Samples

[7] The samples were obtained from an outcrop of the organic-rich R-8 unit of the Green River Shale Formation (Piceance Basin, northwestern Colorado). The formation consists of Eocene lacustrine marl/silt sediments [*Ruble et al.*, 2001] with well-developed lamination and anisotropic mechanical properties [*Vernik and Landis*, 1996]. It contains organic matter (total organic content = 9.92 wt% in analyzed samples) present in the form of patches of kerogen, preferentially distributed parallel to the bedding (Figures 1a and 1b). This part of the formation has never been buried deeply enough to reach temperatures sufficient to cause significant thermal maturation.

[8] Cylindrical core samples (5 mm height, 5 mm in diameter) cut perpendicular to the bedding were prepared for X-ray tomography. Thin sections were taken before and after heating. Optical microscope images (Figures 1a and 1b) highlight the micro-fabric of the uncooked shale consisting of alternating lamellae of: coarser and lighter colored carbonate cemented layers rich in siliciclastic grains (e.g., quartz) and pyrite framboids; and darker and finer grained clay-rich layers, containing greater amount of discontinuous organic matter lenses.

3. 4D Imaging and Data Processing

[9] Time-lapse X-ray tomography 3D imaging of the shale samples was carried out using beamline ID19 at the European Synchrotron Radiation Facility in Grenoble, France. This non-invasive imaging technique measures the absorption of X-rays, to produce a 3D attenuation map.

[10] The prepared shale cylinder was placed in a home-built furnace in contact with air, with no confining pressure, and it was gradually heated in situ from 60°C to 400°C at approximately 1°C/min. 68 3D scans of this sample were taken, of which 28 were acquired during the heating phase and the rest at 400°C. For all scans, 1500 radiographs were acquired while the sample was rotated over 180°. The beam energy of 20 keV allowed images to be captured with a spatial resolution of 5 μm ($5 \times 5 \times 5$ μm^3 voxels) and a time resolution of 11–14 min per 3D scan. 3D raw-tomograms representing the microporous structure of the sample at different stages of heating were constructed from the X-ray data. The final volumes contained 830^3 voxels coded in 8-bit gray levels.

[11] The 3D images were processed in two ways. First, the strain field was measured in a typical 2D vertical slice of the volume, using digital image correlation [*Rechenmacher and Finno*, 2004; *Hild and Roux*, 2006; *Viggiani*, 2009; *Bornert et al.*, 2010]. Second, in order to determine crack geometries and track crack propagation, the shape, volume and morphology of the cracks were analyzed in 3D using the AvizoFire© software package. Quantitative analysis of the crack formation required isolation of the cracks from the rock matrix. Due to the small crack opening (4–5 voxels), the following procedure was applied: first a binary mask was used to delete the background; then an edge-preserving

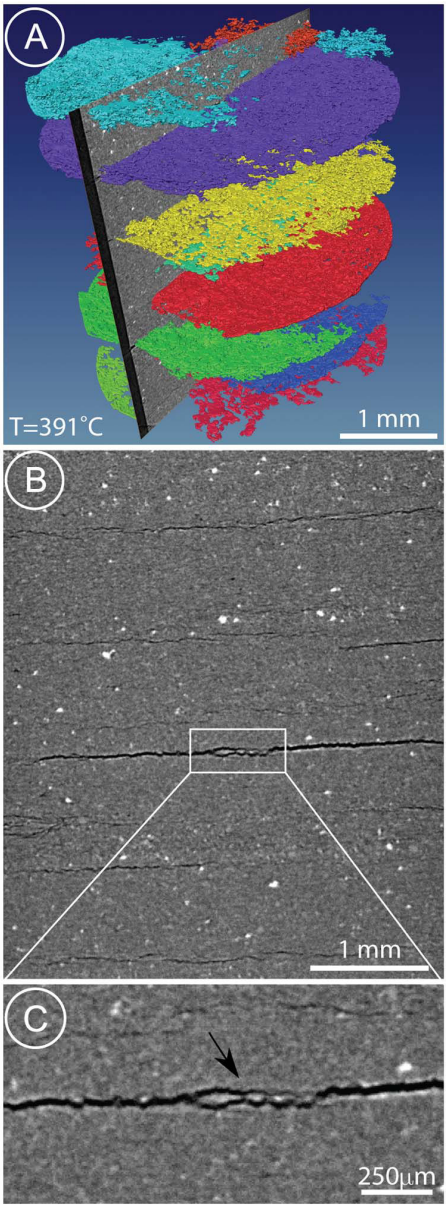

Figure 2. Tomography images of the shale sample at 391°C, corresponding to the moment of maximum crack opening. (a) 3D rendering of final crack network. Each color defines an independent crack. (b) 2D slice showing (dark color) elongated cracks that developed parallel to the bedding. (c) Detail of Figure 2b showing a crack developed around a pyrite grain (arrow).

smoothing filter based on Gaussian smoothing combined with a nonlinear diffusion algorithm was applied; then a "watershed" procedure enabled individual cracks to be isolated [*Sonka et al.*, 1999]. The final result of this segmentation procedure was a series of cracks consisting of connected voxels, marked by different labels/colors (Figure 2a and Animations S1 and S2 of the auxiliary material).[1]

4. Observation of Deformation and Crack Formation

[12] Correlation analysis and 3D image analysis were performed to determine the deformation of the sample before fracturing and the geometries of the developing cracks. The spatial fluctuations of the attenuation maps (see Figure 2b) served as markers when the digital correlation technique was used to compare successive images. To calculate the correlation matrix we used a correlation box of size 25 by 25 pixels (125 by 125 μm^2), which enabled us to measure the spatial distribution of micro-displacements.

[13] Between room temperature and 300°C, the shale dilated anisotropically in the vertical (perpendicular to the shale bedding) and horizontal (parallel to the shale bedding) directions, and the strain curves showed a quasi-linear increase with temperature, as expected for linear thermal expansion (Figure 3a). The coefficient for thermal expansion was determined to be 5.5 * 10^{-5}/°C in the vertical direction and 2.5 * 10^{-5}/°C in the horizontal direction, which clearly indicates the anisotropy of the shale, in agreement with other studies on the same shale [*Grebowicz*, 2008]. At 300°C, the vertical expansion started to deviate from linearity, which is likely related to the onset of organic degassing before crack formation. At a temperature of about 350°C the sample undergoes rapid localized deformation owing to fluid generation and the onset of fracturing. When the sample breaks, black structures corresponding to the newly formed cracks appear in the images (see Figure 2b), which have no equivalent in the preceding ones, thus ruining the correlation technique. Moreover, after the sample fractures, global movement of the sample occurs (translation and rotation), with displacements from one data set to the next of amplitude greater than 12 pixels, which was estimated to be the maximum displacement that can be accurately measured using the correlation technique. Even though the correlation results during and after fracturing are not trustworthy, this technique accurately determines the sample deformation before fracturing occurs.

[14] With 3D tomography, we imaged 3 stages of fracture propagation. The first microfracture pattern was detected at a temperature of about 350°C. Figure 2a shows a 3D rendering of the most opened fractures at T = 391°C (third time step) and Figures 2b and 2c show a vertical slice through the tomography image. The general direction of crack propagation followed the shale bedding, and no perpendicular fractures were observed (Figure 2b). Pyrite grains, observable as bright spots in the tomography images (Figure 2c), affected crack growth by pinning the crack front, and controlling the out-of-plane fluctuations of the crack path.

[15] The fractures can be described in terms of two rough, essentially parallel surfaces that enclose the fracture aperture. Both surfaces can be described by height functions, $h_1(x,y)$ and $h_2(x,y)$, where (x,y) is the position in the common plane. Figure 4a shows the topography of fracture surface $h_1(x,y)$, where the fluctuation of surface function

[1]Auxiliary materials are available in the HTML. doi:10.1029/2011JB008565.

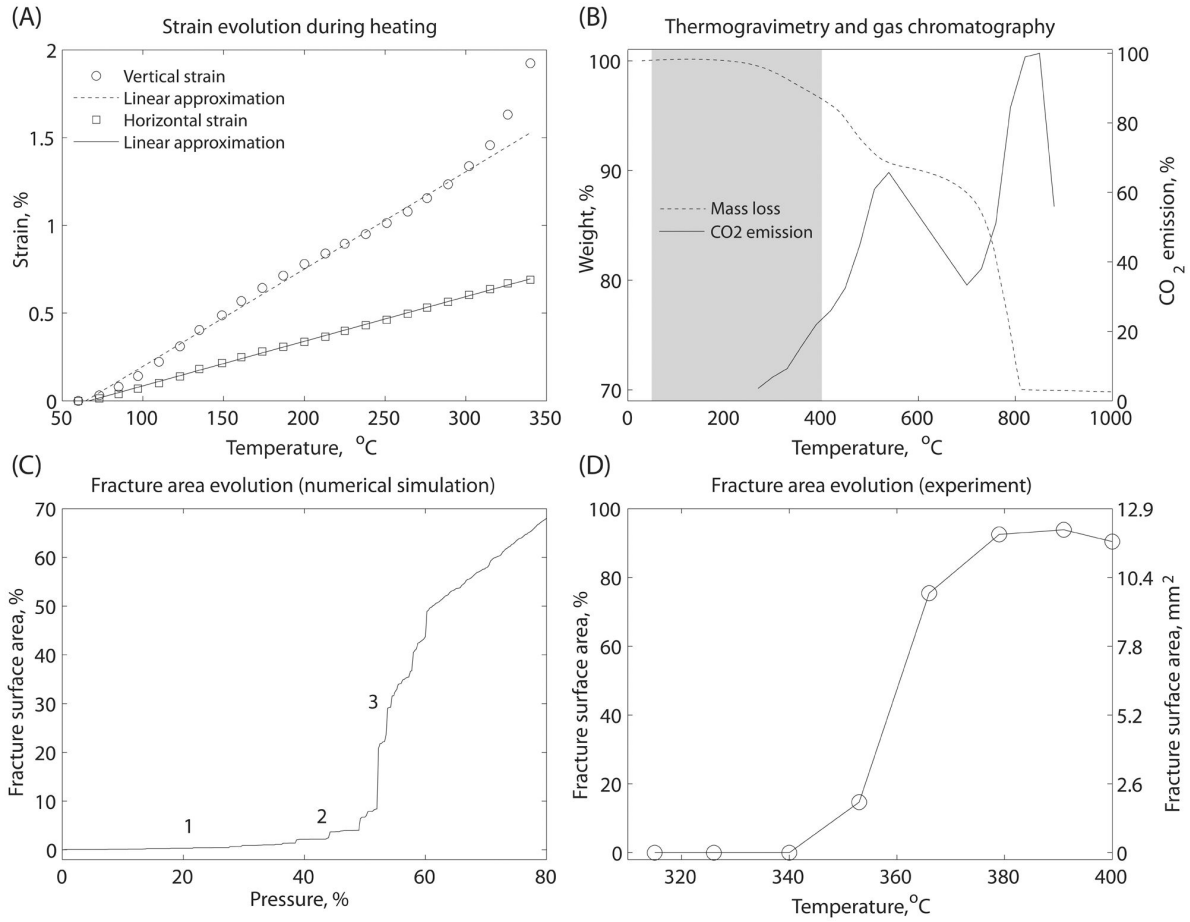

Figure 3. (a) Vertical and horizontal strain in a shale sample during heating. The linear relationship between 70°C and 300°C corresponds to dilation of the sample due to thermal expansion. Because of the anisotropy of the shale, the vertical and horizontal dilations are different. The vertical strain-temperature relationship deviates from linearity at 300°C, at the onset of degassing. Failure of the correlation technique at 350°C corresponds to the fracturing of the sample. (b) Thermogravimetry (mass loss) and carbon dioxide emission analyses in aerobic conditions. The change of slope on the mass loss curve at around 300°C occurs at the same temperature as the onset of CO_2 production and corresponds to the onset of kerogen decomposition. The gray shaded area indicates the temperature range of the tomography experiment. The peak of CO_2 production and mass loss at around 800°C corresponds to the decomposition of carbonate. (c) Growth of the area of the biggest crack as a function of pressure (% of maximum applied pressure) in the 2D lattice model. Numbers 1–3 are the three stages of crack evolution corresponding to nucleation, growth and coalescence (see corresponding snapshots 1–3 in Figure 5b). (d) Fracture evolution in the experiment. Growth of the surface area of the largest crack (in % of the sample cross-sectional area and in mm^2) as a function of temperature. The slight decrease of fracture surface area observed after 390°C is attributed to partial crack closing after fluid expulsion.

$h_1(x,y)$ around the flat plane (x,y) is indicated by the color code. Cracks have essentially constant aperture widths - the thickness function $h_2(x,y) - h_1(x,y)$ (4–5 pixels, i.e., 20–25 μm, see Figure 4b), and rough irregular outlines. The amplitude of the topography variation is around 10–15 pixels (i.e., 50–75 μm), as seen in the Figure 4a. The mid-plane ($H(x,y) = [h_1(x,y) + h_2(x,y)]/2$) is also rough, and it fluctuates about a flat plane – the "plane of the fracture." The projections of $h_1(x,y)$, $h_2(x,y)$ and $([h_1(x,y) + h_2(x,y)]/2$ into this plane, in a direction perpendicular to the plane, have a common shape, which consists of a continuous region with rough edges. When one fracture coalesces with another, a new fracture is formed, and it can be described in terms of the rough surfaces $H^{new}(x,y)$, $h_1^{new}(x,y)$ and $h_2^{new}(x,y)$. The projections of these rough surfaces are also a common shape, which consists of a continuous region with rough edges. The planes of the coalesced fracture and the two fractures that coalesced to form it are more-or-less parallel,

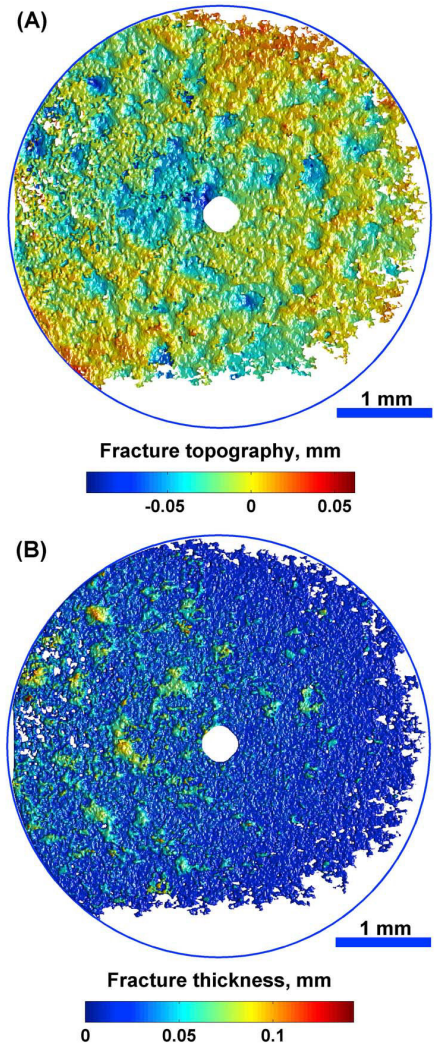

Figure 4. Reconstruction of the (a) topography and (b) thickness of a fracture extracted from Figure 2a. The circular central region in each image was removed because of a data acquisition artifact. The outer circle defines the boundaries of the sample. In Figure 4a fluctuation of fracture surface height $h_1(x,y)$ around the fracture plane (x,y) is indicated by the color scale. The fracture front is irregular. The topography is created by small heterogeneities (i.e., pyrite minerals) that pin the fracture during its propagation. In Figure 4b the fracture thickness, taken as the difference between the upper surface $h_1(x,y)$ and lower surface $h_2(x,y)$ of the fracture, is indicated by the color scale. The thickness is quasi-constant and it is perturbed by pyrite inclusions.

and also quasi-parallel to the shale lamination. Viewed from "above," in the direction perpendicular to the plane of the fractures and the lamination, the fractures are continuous, and they grow and coalesce in three successive stages (Figure 5a). As the temperature rose, cracks nucleated (1), grew and coalesced in a quasi-static manner (2) until they spanned the sample (3). The growth of the surface area of the biggest fracture with increasing temperature is shown in Figure 3d.

5. Organic Decomposition Induces Fracturing in the Shale

[16] Thin sections were studied in order to compare petrographic characteristics of the shale before and after heating. Before heating, organic precursors, which were preferentially oriented parallel to the shale bedding, could be distinguished throughout the sample (see Figures 1a and 1b). After heating, an abundance of cracks, partially filled with residual organic material, was distributed parallel to the bedding (Figures 1c and 1d). Petrographic observations revealed that cracks propagated mainly in the finer grained layers where the highest concentrations of organic matter lenses were observed (Figures 1a and 1c). The coarser grained layers, where quartz grains and pyrite framboids were present in higher concentration, also displayed better cementation with larger calcite crystals. The preferential location of fracture propagation is ascribed to two main factors: (1) Higher amounts of organic matter (kerogen lenses), which decomposes leading to fluid formation, internal pressure build up and eventually fracture initiation and propagation. (2) Finer grained intervals are less cemented than the coarser grained ones and they fracture more easily.

[17] The link between hydrocarbon generation and fracturing was tested using thermogravimetry and gas chromatography. Aerobic and anaerobic (nitrogen) thermogravimetry analyses on 500 mg samples were performed to investigate the presence of organic and inorganic carbon (carbonates) using a ATG/SDTA 851 Mettler Toledo apparatus. We monitored mass loss of the sample during heating at 10°C/min in air or nitrogen between 20°C and 1000°C. The loss of mass during heating occurred in distinct stages (Figure 3b), and the temperature range of each stage indicates the nature of the component that evaporates. We also used gas chromatography (GC 5890-MS 5973 Agilent) to analyze the gas that escaped (water, CO_2, and organic volatiles) during heating at a rate of 5°C/min in air. The first step of mass loss (Figure 3b) in the temperature range 300–450°C corresponds to the release of various organic molecules (alkanes, alkenes, toluene, xylenes), water and CO_2 (first peak on CO_2 emission plot) and indicates decomposition of organic matter. The second step of mass loss around 600–800°C indicates decomposition of carbonates. A similar behavior was observed when nitrogen was used instead of air with two peaks of CO_2 release located at the same temperatures.

[18] Figure 6 shows the correlations between strain evolution, mass loss, CO_2 emission and fracture surface area growth. Comparing the temperatures of degassing, mass loss and hydrocarbon release with the temperature of fracturing onset, we conclude that fracturing was induced by overpressure in the sample caused by organic matter decomposition.

6. Discrete Model of Crack Propagation

[19] Based on the experimentally observed fracturing behavior (Figure 5a), a two dimensional (2D) model of

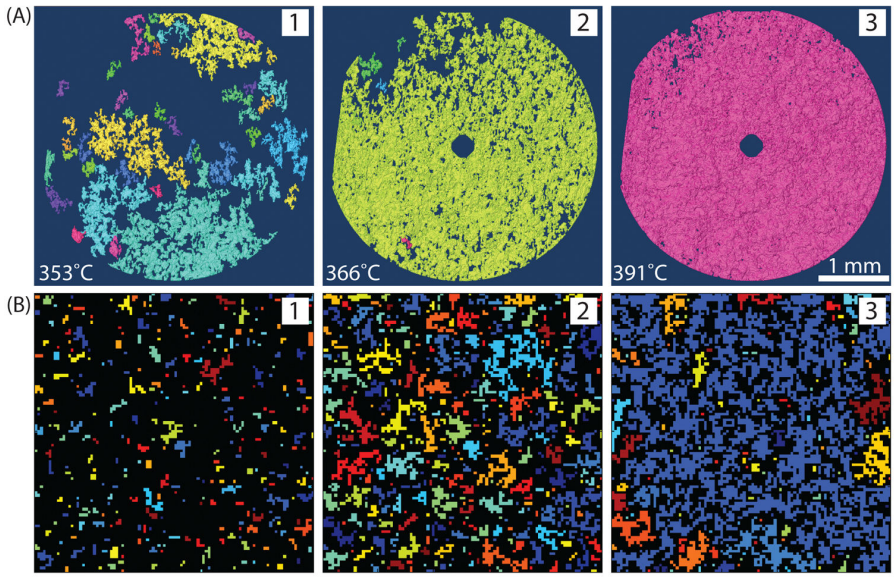

Figure 5. Comparison of crack evolution in the experiment and numerical model. (a) Crack propagation dynamics during heating in the experiment. View of the cracks in a kerogen rich layer viewed from a direction perpendicular to the average plane of the cracks. (1) Numerous small cracks nucleated at ~350°C. Each crack is indicated by a different color. (2) Cracks grew and merged with increasing temperature. (3) Ultimately all cracks merged into a single sample-wide crack. The circular central region in each image was removed because of a data acquisition artifact. (b) 2D lattice model at three stages of crack development: nucleation (1), growth (2) and coalescence (3) of cracks (see three stages of the area growth (1–3) in Figure 3c).

in-plane crack nucleation and growth due to internal pressure increase was developed (Figure 7). The choice of a 2D model is based on the observation of planar mode 1 cracks that follow the layering of the shale and the focus on in-plane dynamics rather than the placement of cracks and relation between cracks normal to their plane. To reproduce key characteristics of the crack growth process including the merging of small cracks and the very irregular crack shapes, we used a statistical fracture model [*Alava et al.*, 2006]. The main parameter needed is the variability of local strength, and the model neglects long range effects of the stress field. The model includes neither the kinetics of kerogen decomposition nor the elastic properties of the source rock, and therefore it cannot quantitatively predict threshold temperatures and pressures, or rates of primary migration. The objective of the model is to find the minimum number of features that explain the observed behavior. The macroscopic fracture threshold and kerogen transformation kinetics are important to predict at what temperature and rate these phenomena occur, but they do not help us understand how the fracture evolves. The percolation like evolution of the fracture, as opposed to the nucleation of a single fracture that propagates rapidly through the shale, which would be predicted by a macroscopic elastic model with a distributed pressure build-up, shows that the material disorder may cause the slow formation of percolating fluid pathways for expulsion of hydrocarbon fluids at pressures much smaller than those needed to completely fracture the shale. The model focuses on a layer of shale that fractures more rapidly than nearby layers because it has a higher kerogen content. The layer is modeled by using a regular square lattice in which every site represents a small organic-rich

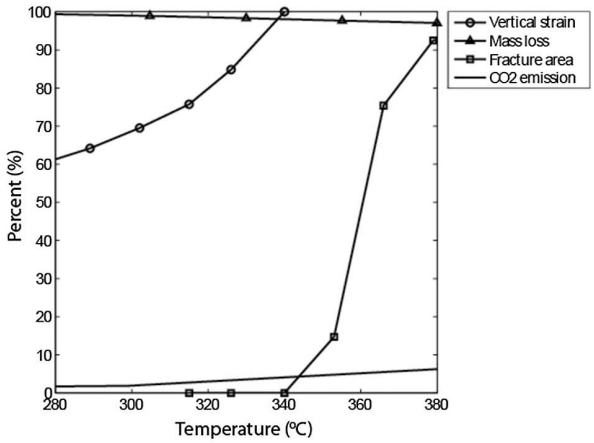

Figure 6. The correlation between vertical strain evolution (perpendicular to the shale lamination) during heating, mass loss, CO_2 emission and growth of fracture area in the shale sample. The onset of the mass loss and CO_2 emission corresponds to decomposition of organic material. The nonlinear strain growth in the vertical direction, which is caused by internal fluid pressure buildup, leads to the fracturing at 340°C.

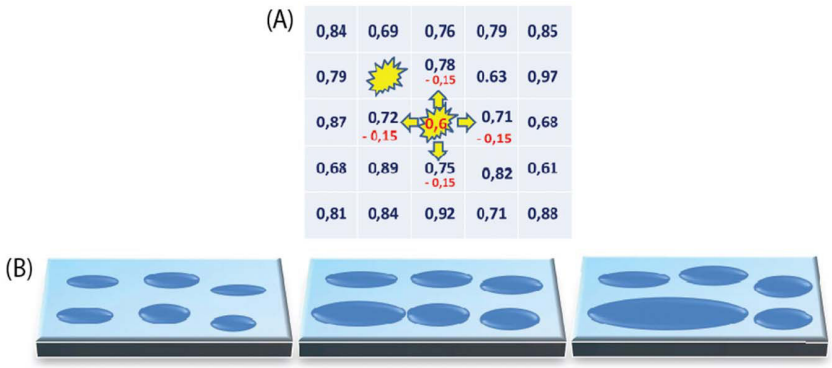

Figure 7. Sketch of the 2D discrete model. (a) The rock layer is modeled by a lattice of sites with assigned breaking thresholds. When a site fractures the stress is distributed equally to the non-broken neighbors, bringing them closer to failure. Two fractured neighbors are called a continuous crack. (b) The cracks grow by including new neighboring broken sites. When two cracks coalesce they form a bigger crack.

shale element. Each site is characterized by a randomly assigned breaking threshold $\sigma_{c,i}$. The pressure in the lattice rises incrementally during each time step and, when it exceeds the breaking threshold ($p_i > \sigma_{c,i}$), the site fractures to represent either nucleation of a new crack or growth of a pre-existing crack. This relaxes the stress, which is distributed equally to the nearest non-broken neighbors (long-range elastic interactions are neglected), bringing them closer to failure. The distribution of stress was implemented by reducing the breaking threshold, $\sigma_{c,i} \rightarrow \sigma_{c,i} - d\sigma$, for all nearest non-broken neighbors. Dimensionless units were used for the pressure and breaking thresholds. Each crack is represented by a cluster of broken sites. As soon as sites belonging to different clusters become adjacent, both clusters are merged to form a single crack, and all the merged sites are given the same label/color.

[20] Figure 5b shows three successive snapshots during a simulation. In the early stage, the system contains many small independent cracks. Each crack has a rough front, and over time, individual cracks grow slowly and merge until the whole plane is covered. Figure 3c displays the increase of the area of the crack that was the largest at the end of the simulation. Crack growth occurs in three stages: (1) the microcracks are all separated and their surface areas grow gradually; (2) the cracks start to coalesce, the rate at which the fractured area increases accelerates, and growth in the total fracture area is dominated by distinct jumps; and (3) ultimately the system is dominated by one large fracture, with an area that grows by intermittent increases (see also the corresponding snapshots 1–3 in Figure 5b and Animation S3 of the auxiliary material). The qualitative trend of the fracture area growth in the simulation (Figure 3c) is similar to that observed in the experiment (Figure 3d).

[21] The model is similar to the fiber bundle model with local load sharing, which has been intensively used to model material failure [*Pradhan et al.*, 2010]. We suggest that it can be applied to other geological systems in which chemical reactions induce volume increase and stress build-up in rocks. These systems are widespread and include, apart from primary migration of hydrocarbons, weathering of rocks near the surface [*Røyne et al.*, 2008] and dehydration of serpentines in subduction zones [*Jung*, 2004].

7. Discussion and Conclusion

[22] Time-resolved high-resolution synchrotron X-rays tomography was performed during gradual heating (from 60 to 400°C) of organic-rich immature shales. At 350°C the nucleation of many small cracks was detected. With further temperature increase these microcracks propagated parallel to the shale bedding, coalesced and ultimately spanned the whole sample.

[23] The central point of our work is the observed correlation between hydrocarbon expulsion and fracturing within the sample. To do this, we combined thermogravimetry, gas chromatography, strain analysis and 3D observation of fracture formation and analyze the data in 3 steps:

[24] 1. Analyzing tomograms, we found that fracturing begins at a temperature of about 350°C.

[25] 2. Using thermogravimetry, we determined that the sample started to loose mass in the same temperature range (about 350°C). This alone does not provide us with the composition of the lost material.

[26] 3. Using gas chromatography, we determine that the gases expelled at temperatures near 350°C were mainly oxidized hydrocarbons, and we conclude that they originate from kerogen decomposition.

[27] In the literature, some shale rocks are reported to contain horizontal (in the direction of shale bedding) mode I fractures as well as vertical (perpendicular to the shale bedding) fractures. The presence of vertical fractures indicates that the maximum stress is vertical [*Olson*, 1980; *Smith and Chong*, 1984]. However, at shallow depths, where the magnitudes of both the vertical and horizontal stresses are similar, horizontal hydro-fractures of significant lateral extent can be created due to anisotropy of shales [*Thomas*, 1972; *Jensen*, 1979]. Horizontal fractures are also observed to develop in clay-rich shales in response to high overpressures during maturation [*Littke et al.*, 1988], even in regions where the vertical stress is larger than the horizontal stress. The reason for this is thought to be the strong

lamination of these shales [*Lash and Engelder*, 2005]. Theoretical studies [*Ozkaya*, 1988] also showed that vertical cracks are unlikely to form by oil generation and the excess of oil pressure is sufficient to cause lateral fracturing if the aspect ratio of kerogen patches is sufficiently large.

[28] In nature petroleum generation takes place in the 80–150°C temperature range, and this occurs typically over time periods of 1–100 million years (up to 500 million in some geological situations). The heating rate for a basin like the North Sea is 1–2°C/million years, but during rapid sedimentation and subsidence the heating rate is as high as 10°C/million years [*Bjørlykke*, 2010]. In our experiments, conducted in a much shorter time, fracturing was observed to occur in the temperature range of 300–400°C.

[29] The decomposition of kerogen involves a very large number of coupled chemical reactions, and a temperature dependent rate constant is associated with each reaction. In general, the rates of these reactions can be represented approximately by the Arrhenius function $K_i = A_i T^n exp(-E_i^a/RT)$, where K_i is the rate constant for the ith reaction, A_i is its frequency factor, E_i^a is its activation energy, R is the gas constant and T is the absolute temperature. In most cases, n is small, the temperature dependence is dominated by the exponential term and the Arrhenius equation is often expressed in the form $A_i' exp(-E_i^a/RT)$. The overall rate of the organic maturation process, K, can also be represented by a similar Arrhenius function $K = Aexp(-E^a/RT)$, although the nature of the decomposition products is also somewhat temperature dependent. If the activation energy, E^a, is large enough, the maturation rate increases rapidly with increasing temperature, and this explains why a higher temperature can be used to accelerate the maturation process and achieve a maturation time that is short enough to conduct laboratory experiments.

[30] Under natural conditions cracks form during maturation at lower temperature, and because of the low rate of pressure buildup crack growth is probably a slow subcritical fracturing process. Based on theoretical calculations by [*Ozkaya*, 1988], we can estimate the conditions for the initiation of lateral cracking. [*Ozkaya*, 1988] considered a linearly elastic and isotropic source rock containing isolated kerogen flakes enclosed in an impermeable shale matrix, and showed that the aspect ratio of the kerogen particles may influence the initiation of horizontal microcracks in the source rock beds under maximum vertical principal stress. Initiation of microcracks as a function of kerogen flakes shape occurs when:

$$\Delta P\left(\frac{2w}{h} - 1\right) > S_v(2 - k) + C, \quad (1)$$

where S_v is the principal vertical stress, k is the lateral to vertical stress ratio, C is the strength of the rock, ΔP is the excess oil pressure induced during kerogen decomposition, w is the characteristic length of the kerogen particles, and h is the thickness of kerogen particles. For example, for the kerogen patch shown on the Figure 1c, the aspect ratio is w/h = 50 μm/3 μm ≈ 16. For k = 0.75, ΔP = 5 Mpa, C = 10 MPa [*Ozkaya*, 1988], equation (1) indicates that lateral fracturing may occur if the vertical stress S_v is lower than 116 MPa, which corresponds to a depth h smaller than 4000 m.

[31] One limitation of this calculation is the assumption that the kerogen patches are surrounded by impermeable rock. In reality, shales have very small permeabilities and the transformation reaction is slow. The generated fluids may migrate through the rock matrix without producing pressure gradients that are large enough to cause fracturing. However, magma emplacement in sedimentary basins may result in much higher maturation rates and the rapid production of hydrocarbon fluids may cause rapid internal pressure build up and fracture generation.

[32] To summarize our observations, correlation analysis monitoring of the deformation of the sample indicated abrupt swelling perpendicular to the bedding just before cracks formation began. Petrography observations showed that the main cracks initiate in the finer grained clay-rich layers where a higher amount of organic matter is present. Thermogravimetry and gas chromatography analyses showed that the sample began to lose significant mass and release water, CO_2 and hydrocarbon gasses at about 350°C. These observations support a scenario in which the kerogen, present in thin lenses, starts to decompose around 350°C, causing volume increase and internal pressure build up leading to fracturing. The fracturing mechanism observed experimentally, including crack formation and crack geometry, was successfully reproduced by a 2D "fiber-bundle" lattice simulation. The success of the statistical fracture model indicates that material disorder and local elastic interactions play a key role in the development of the observed percolation like fracture. The implication is that percolating low permeability fluid pathways are formed in the shale long before macroscopic fracturing occurs.

[33] In the present study we do not characterize fracturing of source rocks under natural conditions. In particular, no confinement was applied to the sample. We therefore suggest that the results of our experiments can be directly relevant to better understand induced fracturing of shales located at shallow depth or outcrops, where the confinement pressure is low. More generally, the methods developed here will be relevant for future studies under more realistic conditions.

[34] **Acknowledgments.** We acknowledge support by the Petromaks program of the Norwegian Research Council. We thank Elodie Boller at ESRF for her help during the tomography scans and Rodica Chiriac for her help with the thermogravimetry analyses. This study was supported by a Center of Excellence grant from the Norwegian Research Council to the Physics of Geological Processes Center (PGP).

References

Alava, M. J., P. K. V. V. Nukalaz, and S. Zapperi (2006), Statistical models of fracture, *Adv. Phys.*, *55*, 349–476, doi:10.1080/00018730300741518.

Berg, R. R., and A. F. Gangi (1999), Primary migration by oil-generation microfracturing in low-permeability source rocks: Application to the Austin Chalk, Texas, *AAPG Bull.*, *83*, 727–756.

Bjørlykke, K. (2010), *Petroleum Geoscience: From Sedimentary Environments to Rock Physics*, Springer, Berlin, Germany.

Bornert, M., F. Vales, H. Gharbi, and D. N. Minh (2010), Multiscale full-field strain measurements for micromechanical investigations of the hydromechanical behaviour of clayey rocks, *Strain*, *46*, 33–46.

Capuano, R. M. (1993), Evidence of fluid flow in microcracks in geopressured shales, *AAPG Bull.*, *77*, 1303–1314.

Grebowicz, J. (2008), Thermal properties of Green River oil shales, *Geol. Soc. Am. Abstr. Programs*, *40*, 554.

Hild, F., and S. Roux (2006), Digital image correlation: From displacement measurement to identification of elastic properties: A review, *Strain*, *42*, 69–80, doi:10.1111/j.1475-1305.2006.00258.x.

Jensen, H. B. (1979), Oil shale in situ research and development, Talley Energy systems final report, DOE/LC/01791–T1, U.S. Dep. of Energy, Washington, D. C.

Jin, Z.-H., S. E. Johnson, and Z. Q. Fan (2010), Subcritical propagation and coalescence of oil-filled cracks: Getting the oil out of low-permeability source rocks, *Geophys. Res. Lett.*, *37*, L01305, doi:10.1029/2009GL041576.

Jung, H. (2004), Intermediate-depth earthquake faulting by dehydration embrittlement with negative volume change, *Nature*, *428*(6982), 545–549, doi:10.1038/nature02412.

Lash, G. G., and T. Engelder (2005), An analysis of horizontal microcracking during catagenesis: Example from Catskill delta complex, *AAPG Bull.*, *89*, 1433–1449, doi:10.1306/05250504141.

Littke, R., D. R. Baker, and D. Leythaeuser (1988), Microscopic and sedimentologic evidence for the generation and migration of hydrocarbons in Toarcian source rocks of different maturities, *Org. Geochem.*, *13*, 549–559, doi:10.1016/0146-6380(88)90075-7.

Marquez, X. M., and E. W. Mountjoy (1996), Microcracks due to overpressure caused by thermal cracking in well-sealed Upper Devonian reservoirs, deep Alberta basin, *AAPG Bull.*, *80*, 570–588.

Mazzini, A. (2009), Mud volcanism: Processes and implications, *Mar. Pet. Geol.*, *26*, 1677–1680, doi:10.1016/j.marpetgeo.2009.05.003.

Obara, K. (2002), Nonvolcanic deep tremor associated with subduction in southwest Japan, *Science*, *296*, 1679–1681, doi:10.1126/science.1070378.

Olson, W. A. (1980), Stress relaxation in oil shale, in *Proceedings of 21st Symposium on Rock Mechanics*, edited by D. A. Summers, pp. 517–520, Univ. of Miss., Rolla.

Ozkaya, I. (1988), A simple analysis of oil-induced fracturing in sedimentary rocks, *Mar. Pet. Geol.*, *5*, 293–297, doi:10.1016/0264-8172(88)90008-6.

Pradhan, S., A. Hansen, and B. K. Chakrabarti (2010), Failure processes in elastic fiber bundles, *Rev. Mod. Phys.*, *82*, 499–555, doi:10.1103/RevModPhys.82.499.

Rechenmacher, A. L., and R. J. Finno (2004), Digital image correlation to evaluate shear banding in dilative sands, *Geotech. Test. J.*, *27*, 13–22, doi:10.1520/GTJ10864.

Røyne, A., B. Jamtveit, J. Mathiesen, and A. Malthe-Sorrenssen (2008), Controls of rock weathering rates by reaction-induced hierarchical fracturing, *Earth Planet. Sci. Lett.*, *275*, 364–369, doi:10.1016/j.epsl.2008.08.035.

Ruble, T. E., M. D. Lewan, and R. P. Philp (2001), New insights on the Green River petroleum system in the Uinta basin from hydrous pyrolysis experiments, *AAPG Bull.*, *85*, 1333–1371.

Smith, J. W., and K. P. Chong (1984) Introduction to mechanics of oil shale, in *Mechanics of Oil Shale*, edited by K. P. Chong and J. W. Smith, pp. 1–41, Elsevier, New York.

Sonka, M., V. Hlavac, and R. Boyle (1999), *Image Processing, Analysis and Machine Vision*, PWS Publ., Pacific Grove, Calif.

Svensen, H., S. Planke, A. Malthe-Sorenssen, B. Jamtveit, R. Myklebust, T. R. Eidem, and S. S. Rey (2004), Release of methane from a volcanic basin as a mechanism for initial Eocene global warming, *Nature*, *429*(6991), 542–545, doi:10.1038/nature02566.

Thomas, H. E. (1972), Hydraulic Fracturing of Wyoming Green River Oil Shale: Field Experiments, *Phase I, Rep. Invest. Ser.*, vol. 7596, Bur. of Mines, U.S. Dep. of the Inter., Washington, D. C.

Vernik, L., and C. Landis (1996), Elastic anisotropy of source rocks: Implications for hydrocarbon generation and primary migration, *AAPG Bull.*, *80*, 531–544.

Viggiani, G. (2009), Mechanisms of localized deformation in geomaterials: An experimental insight using full-field measurement techniques, in *Mechanics of Natural Solids*, pp. 105–125, Springer, New York.

D. K. Dysthe, B. Jamtveit, M. Kobchenko, A. Malthe-Sørenssen, A. Mazzini, H. Panahi, and J. Scheibert, Physics of Geological Processes, University of Oslo, Oslo N-0316, Norway. (kobchenko.maya@gmail.com)

P. Meakin, Center for Advanced Modeling and Simulation, Idaho National Laboratory, PO Box 1625, MS 2211, Idaho Falls, ID 83415, USA.

F. Renard, Institut des Sciences de la Terre, Université Joseph Fourier, CNRS, Grenoble F-38041, France.

Paper 2

A 4D synchrotron X-ray-tomography study of the formation of hydrocarbon- migration pathways in heated organic-rich shale

H. Panahi[1,2], M. Kobchenko[1], F. Renard[1,3], A. Mazzini[1], J. Scheibert[4], D. Dysthe[1], B. Jamtveit[1], A. Malthe-Sørenssen[1] and P. Meakin[1,5,6]

[1]Physics of Geological Processes, University of Oslo,
[2]Statoil ASA, Oslo,
[3]Institut des Sciences de la Terre, University of Grenoble I & CNRS,
[4]Laboratoire de Tribologie et Dynamique des Systmes, CNRS, Ecole Centrale de Lyon,
[5]Center for Advanced Modeling and Simulation, Idaho National Laboratory,
[6]Institute for Energy Technology, Kjeller.

Publication data:
Journal of Society of Petroleum Engineers, SPE-162939-PA, doi:10.2118/162939-PA.

A 4D Synchrotron X-Ray-Tomography Study of the Formation of Hydrocarbon-Migration Pathways in Heated Organic-Rich Shale

H. Panahi, University of Oslo, University of Tehran, and Statoil; **M. Kobchenko,** University of Oslo; **F. Renard,** University of Oslo and ISTerre, University of Grenoble I & CNRS; **A. Mazzini,** University of Oslo; **J. Scheibert,** Laboratoire de Tribologie et Dynamique des Systèmes, France; **D. Dysthe, B. Jamtveit,** and **A. Malthe-Sorenssen,** University of Oslo; and **P. Meakin,** University of Oslo, Idaho National Laboratory, and Institute for Energy Technology

Summary

Recovery of oil from oil shales and the natural primary migration of hydrocarbons are closely related processes that have received renewed interest in recent years because of the ever tightening supply of conventional hydrocarbons and the growing production of hydrocarbons from low-permeability tight rocks. Quantitative models for conversion of kerogen into oil and gas and the timing of hydrocarbon generation have been well documented. However, lack of consensus about the kinetics of hydrocarbon formation in source rocks, expulsion timing, and how the resulting hydrocarbons escape from or are retained in the source rocks motivates further investigation. In particular, many mechanisms have been proposed for the transport of hydrocarbons from the rocks in which they are generated into adjacent rocks with higher permeabilities and smaller capillary entry pressures, and a better understanding of this complex process (primary migration) is needed. To characterize these processes, it is imperative to use the latest technological advances. In this study, it is shown how insights into hydrocarbon migration in source rocks can be obtained by using sequential high-resolution synchrotron X-ray tomography. Three-dimensional images of several immature "shale" samples were constructed at resolutions close to 5 μm. This is sufficient to resolve the source-rock structure down to the grain level, but very-fine-grained silt particles, clay particles, and colloids cannot be resolved. Samples used in this investigation came from the R-8 unit in the upper part of the Green River shale, which is organic rich, varved, lacustrine marl formed in Eocene Lake Uinta, USA. One Green River shale sample was heated in situ up to 400°C as X-ray-tomography images were recorded. The other samples were scanned before and after heating at 400°C. During the heating phase, the organic matter was decomposed, and gas was released. Gas expulsion from the low-permeability shales was coupled with formation of microcracks. The main technical difficulty was numerical extraction of microcracks that have apertures in the 5- to 30-μm range (with 5 μm being the resolution limit) from a large 3D volume of X-ray attenuation data. The main goal of the work presented here is to develop a methodology to process these 3D data and image the cracks. This methodology is based on several levels of spatial filtering and automatic recognition of connected domains. Supportive petrographic and thermogravimetric data were an important complement to this study. An investigation of the strain field using 2D image correlation analyses was also performed. As one application of the 4D (space + time) microtomography and the developed workflow, we show that fluid generation was accompanied by crack formation. Under different conditions, in the subsurface, this might provide paths for primary migration.

Original SPE manuscript received for review 31 March 2011. Revised manuscript received for review 6 May 2012. Paper (SPE 162939) peer approved 16 May 2012.

Key words in this work include 4D microtomography, 3D image processing, shale, strain field analysis, kerogen, petroleum generation, primary migration, petrography, and thermogravimetry.

Introduction

Over the past few years, X-ray microtomography or X-ray computed tomography (CT)—a non-destructive technique—has become increasingly more important and widely applied to the study of rock morphology, microtexture, transport properties, and fracturing (Lindquist et al. 2000; Arns et al. 2001; Mees et al. 2003). The internal structure of the rock samples was determined from variations in the X-ray attenuation, which depend on the atomic structure and density. One-dimensional or 2D radiographs are acquired by stepwise rotation of either the X-ray source/detector or the sample followed by mathematical reconstruction of the horizontal cross sections, which are perpendicular to the axis of rotation. It is now common knowledge that CT registers the attenuation of the X-rays, which is material- and X-ray-energy-dependent. The inelastic scattering of X-ray photons in matter results in a decrease in energy (an increase in wavelength), and photoelectric attenuation is also important, especially at low energies. Unless the X-rays are produced by radioactive decay, they are always polychromatic with a wide range of energies (wavelengths). This complicates quantitative analysis and creates artifacts in the CT images, because of the stronger attenuation of X-rays with lower energies. Monochromatization by diffraction eliminates these problems, but it involves a great decrease in intensity and is therefore feasible only for high-intensity X-ray sources, such as linear electron accelerators and large synchrotron "light" sources (Mees et al. 2003). Because of recent advances in computer processing power, high-accuracy X-ray CT is becoming more commonplace in rock-physics laboratories around the world.

Most studies have focused on the analysis of static 3D tomograms. However, with increased resolution and decreased scan duration, made possible by high-intensity, highly collimated, quasimonochromatic X-ray beams, it is now feasible to investigate time-dependent processes. We have applied this methodology to study the coupling between fluid generation and fracturing in Green River shale—an experimental model for primary migration.

A number of mechanisms have been proposed to explain primary migration, the generation of hydrocarbon fluids in source rocks, and the expulsion of these fluids into nearby secondary-migration pathways. These mechanisms include migration through a continuous oil-saturated kerogen network (McAuliffe 1979), migration of microdroplets, migration of micelles (Cordell 1973), migration of oil emulsion, migration of oil dissolved in water (Bray and Foster 1980), and migration of oil dissolved in gas (Price 1989). However, there is still no consensus concerning the controlling mechanisms (Hermanrud et al. 1993). In all likelihood, several mechanisms play a role in primary migration, and their

relative importance depends on the initial organic and inorganic composition of the shale, the heterogeneity, the stage of maturation, the temperature/pressure history, and other factors.

The idea that microcracks play an important role in primary migration is supported by observations that cracks at all scales pervade mature source rocks (Chanchani et al. 1996; Lash and Engelder 2005) and laboratory specimens after experiments in which shales with a significant organic content were thermally decomposed under confinement (Tissot and Pelet 1971). In at least some source rocks, microcracks are expected to heal rapidly after they have formed (Mann 1994), and characterization of the crack network in mature source rocks may lead to substantial underestimation of the role played by microcracks. The mechanical properties of the source rock may be altered during the maturation process, and the roles played by fracturing and crack healing depend on these properties and the rate of fluid production as well as the nature of the fluid.

Flow in cracks or other high-permeability and low-capillary-pressure pathways appears to be essential to support the migration of hydrocarbon over large distances from the interior of thick source-rock beds to secondary migration pathways. Except possibly for methane, the diffusion coefficients are too small, and the solubilities in water are too low (England et al. 1987; Hunt 1995), for diffusion through the organic and/or aqueous phases to be sufficient by itself, and the permeabilities of typically very-fine-grained source rocks are too low, and the capillary pressures are too high, for fluid flow to be sufficient without fracturing. This has led to the idea that microcracks act as fluid pathways during primary migration (Snarsky 1964; Tissot and Welte 1978). Nevertheless, most experiments performed to obtain a better understanding of primary migration (Lafargue et al. 1994; Rudkiewicz et al. 1994) do not address the role played by cracks. Of course, other mechanisms are required to transport the hydrocarbon fluids from where they are formed to the microcracks, but mechanisms such as diffusion and viscous flow through very-low-permeability rock matrices may be more effective over these very short distances.

To be able to properly characterize microscopic and macroscopic transport phenomena in tight rocks, including shales, it is imperative to obtain quantitative information about the evolution of microcracks. Much progress has been made in digital data-processing and imaging techniques, and this has made it possible to study processes at much finer scales. Several methods can be used to visualize the pore structure in two dimensions (planar cuts through 3D objects). Scanning electron microscopy (SEM) (Danilatos 1988), transmission electron microscopy (TEM) and X-ray fluorescence imaging (XRF) have been widely used to obtain 2D images with micron and submicron resolutions. Constructing a 3D representation of a sample from multiple 2D micrographs is challenging and cannot reproduce all the sample heterogeneities. If the sample must be removed to prepare a new surface or thin section, it can be very difficult to reposition the sample and obtain a new image with the same orientation as previous images and a position that is known relative to the positions of the previous images with a high enough accuracy to prevent distortion of the final 3D image. Moreover, the process used to obtain thin sections or prepare flat surfaces for TEM, XRF, and SEM scans requires destruction of the sample. For these reasons, we used X-ray microcomputed tomography as a nondestructive 3D imaging technique. Recently, focused-ion-beam scanning electron microscopy (FIB-SEM) has been used to obtain 3D images of shales and mudstones (Schiffbauer and Xiao 2009). In FIB-SEM, the FIB is used to perform nanotomography by alternately milling or cross-sectioning the sample and recording an SEM image. The SEM images can be used to construct a very-small-scale 3D image, which complements the information obtained from coarser-scale 3D X-ray tomography. However, this destructive technique cannot be used to determine directly how the structure changes in time under constant conditions or as conditions are changed.

X-ray microtomography, which was introduced earlier, has been used for a variety of geological applications including measuring the microstructures and mineral contents of rocks (Wevers et al. 2000; Lindquist et al. 2000), determining the spatial characteristics and distributions of minerals and investigating processes such as fracturing, dissolution, and precipitation (Renard et al. 2004, 2009). Determination of pore-network geometry to calculate permeability and porosity is widely used despite the need for high-speed large-memory computing systems (Arns et al. 2001; Renard et al. 2004).

In the present study, we imaged the nucleation and growth of microcracks in tight rocks, including mudstones and shales, on scales down to the experimental resolution limit. A large number of samples from different geographical locations were imaged using computed X-ray microtomography to investigate geometrically complex cracks and the growth of cracks inside optically opaque materials. The resulting 3D volumes were represented by large 3D voxel maps that required fairly intense data processing. A customized workflow was developed for processing the tight-rock tomograms, with the objective of reducing the processing time. To complement this study, some samples were further investigated using SEM and thermogravimetric analysis. This helped us to identify correlations between the volumes in which organic material is present and the volumes in which microcrack nucleation and growth (underlying strain-field development) occur, and to determine the temperatures over which kerogen transformation happened.

Materials and Methods

Shale Samples. Shale samples were collected from the organic-rich R-8 unit in the upper part of the Green River shale formation, USA **(Table 1).** The Green River shale is a marl, which was deposited in Eocene Lake Uinta. The organic matter has undergone conversion to Type I kerogen, but there has been little or no thermal maturation of the kerogen. The R-8 unit, from which the Green River shale samples were obtained, is of potential commercial interest because of its high oil yield (GRS II and GRS IV samples in Table 1).

Shale Geochemical and Petrophysical Characterizations. Several samples were chosen for geochemical and petrophysical characterizations before acquiring X-ray tomographic images (tomograms). Total carbon content and organic and inorganic carbon ratio measurements, optical observations on thin sections, and chemical analysis using an electron microprobe were performed to characterize the mineralogical composition, the organic content, and the microstructure of the shales.

Microstructure Study. Several thin sections, prepared from the Green River shale sample adjacent to the 4-m $\times$ 4-mm cores extracted from the larger shale samples for X-ray tomography, were used for SEM including back-scattered electron imaging (BSE) and energy-dispersive X-ray spectroscopy (EDS) imaging. Analysis of the data acquired in these experiments allowed us to identify the elements and the types of minerals present and also map the organic and inorganic (carbonate) carbon. **Figs. 1a and 1b** show BSE images of two Green River Shale samples in which organic carbon and pyrite (FeS_2) are clearly visible owing to their gray-level contrast.

Organic Content. The presence of organic carbon was further investigated using TOC and TIC analyses (Table 1), which showed that these samples contained significant amounts of organic carbon. In addition, aerobic and anaerobic thermogravimetric analyses were performed on 20-mg powder samples to investigate the presence of volatile fluids such as water, organic substances, and inorganic minerals that undergo thermal decomposition to form volatile products such as carbon dioxide. We used thermogravimetric analysis with simultaneous differential thermal analysis (ATG/SDTA) with a Mettler Toledo ATCG/SDTA851 thermogravimetric analyzer. This technique continuously measures the weight of a sample during heating from 20 to 1200°C. The release of volatile components during heating occurs in stages, and the temperatures associated with each stage provide

TABLE 1—TWO GEOCHEMICALLY ANALYZED GREEN RIVER SHALE SAMPLES FOR WHICH X-RAY MICROTOMOGRAPHIC IMAGES WERE CONSTRUCTED—SAMPLES ACQUIRED FROM THE GREEN RIVER FORMATION, USA

	TC-TOC-TIC/Geochemical Analyses		
Analyzed Sample (Sample Name)	TC	TOC	TIC
Green River Shale-01	13 wt%	10 wt%	3 wt%
Green River Shale-02 (GRS II, GRS IV)	13 wt%	9 wt%	4 wt%

TC: total carbon
TOC: total organic carbon
TIC: total inorganic carbon

an indication on the nature of the component(s) that evaporates and/or decomposes. Thermogravimetry was also coupled with gas chromatography/mass spectrometry (GC/MS) using an Agilent 5890 GC/5973 mass-spectrometer system to analyze the gases (water, CO_2, and organic volatiles) that were driven off. The thermogravimetric analyses were performed either under air or in an oxygen-free nitrogen environment at atmospheric pressure.

For immature samples of Green River shale, several steps of weight loss could be identified. There was an interval between 250 and 380°C that corresponds to dehydration of clay minerals and another distinct step in the 380–470°C temperature range, that corresponds to the release of various organic molecules. This was observed for the Green River shale samples **(Fig. 2).** The X-ray-tomography analysis, discussed in the following subsection, indicates that this loss of weight is accompanied by the formation of microcracks in the sample. The weight loss that occurred in the 750–850°C range corresponds to the decomposition of carbonate minerals.

X-Ray Tomography Acquisition and 3D Reconstruction. Cylindrical core samples (4×4 mm) were extracted from larger shale samples, perpendicular to the stratification, and were imaged in three dimensions using X-ray tomography. Two X-ray computed microtomography campaigns were conducted at the X02DA TOMCAT beamline at the Swiss Light Source (SLS) in Zürich, Switzerland, and at the ID19 beamline at the European Synchrotron Radiation Facility (ESRF) in Grenoble, France. The voxel resolutions of the images were 5.05 μm at SLS and 4.91 μm at ESRF. In both cases, collimated 20-keV X-ray beams were used. Unlike the ring artifacts in the images obtained from the ESRF samples, most of the samples imaged at SLS had ring artifacts with a wide range of gray-scale values, which made their removal without removing some of the sought after features, such as microcracks, impossible.

Additionally, one of the Green River shale samples was imaged while its temperature was continuously increased from 60 to 400°C. This was performed using an in-situ oven available on site at ESRF (Terzi et al. 2009). The oven was controlled by a computer, and a heat ramp of 1°C/min was programmed between 60 and 400°C, while 3D scans were acquired continuously. On average, each scan required approximately 20 minutes–17 images images were acquired as the sample was heated from 60 to 400°C, and an additional 51 images were required at a constant temperature of 400°C, for a total of 68 scans. Therefore, it was possible to follow the evolution of this sample during the decomposition of organic matter.

Most of the analyses were carried out on this sample, because it was possible to track crack nucleation and growth as resolved at 5 μm and characterize the cracks at many steps during their quasi-static propagation. Other 3D X-ray attenuation images were analyzed in detail to determine the orientation, density, spacing and geometries of the cracks and study their displacement/strain fields.

Before the images can be used for further processing, and eventually scientific interpretation, there is one intermediate step which was performed at the synchrotron facilities in Switzerland and in France. Full 3D representations of the samples were constructed from 2D X-ray images using the projection slice theorem (Bracewell 1990; Levoy 1992) with enhanced features for more-accurate reconstruction (Deans 1983). Several artifacts, which have been discussed in the literature, including beam hardening, hot points, and ring artifacts, were reduced by filtering the raw data. However, ring artifacts were apparent in some of the reconstructed 3D data. The ring artifacts from analysis of the ESRF data could be filtered out in the later stages of image processing by removing the high-contrast voxels, because their grey-scale values were at one end of the spectrum in multiple slices of the imaged samples. This was not possible for the SLS rings artifacts

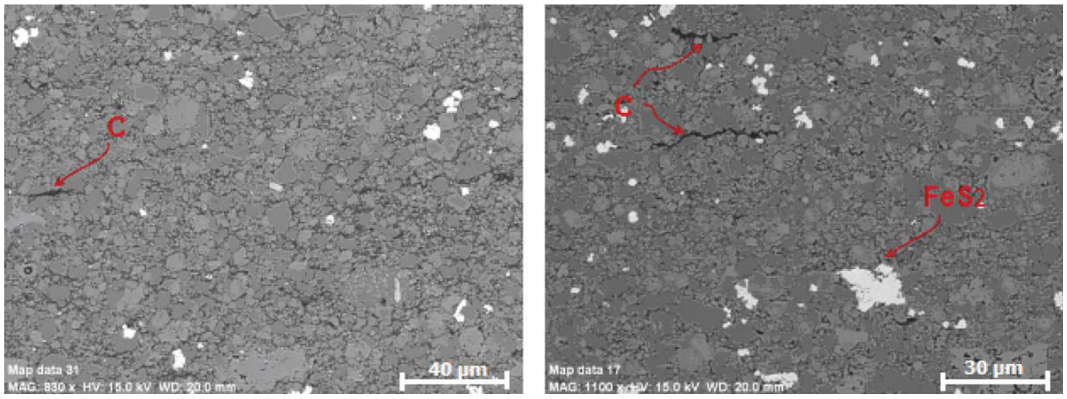

(a) (b)

Fig. 1—Parts a and b display BSE images of two Green River shale thin sections. The atomic backscattering intensity increases with increasing atomic number, and the greatest backscattered-electron intensity (the most lightly shaded areas) correspond to dense minerals such as pyrite composed of high-atomic-number minerals. The darkest areas correspond to low-density, low-atomic-number components, such as organic materials, and the black regions indicate voids.

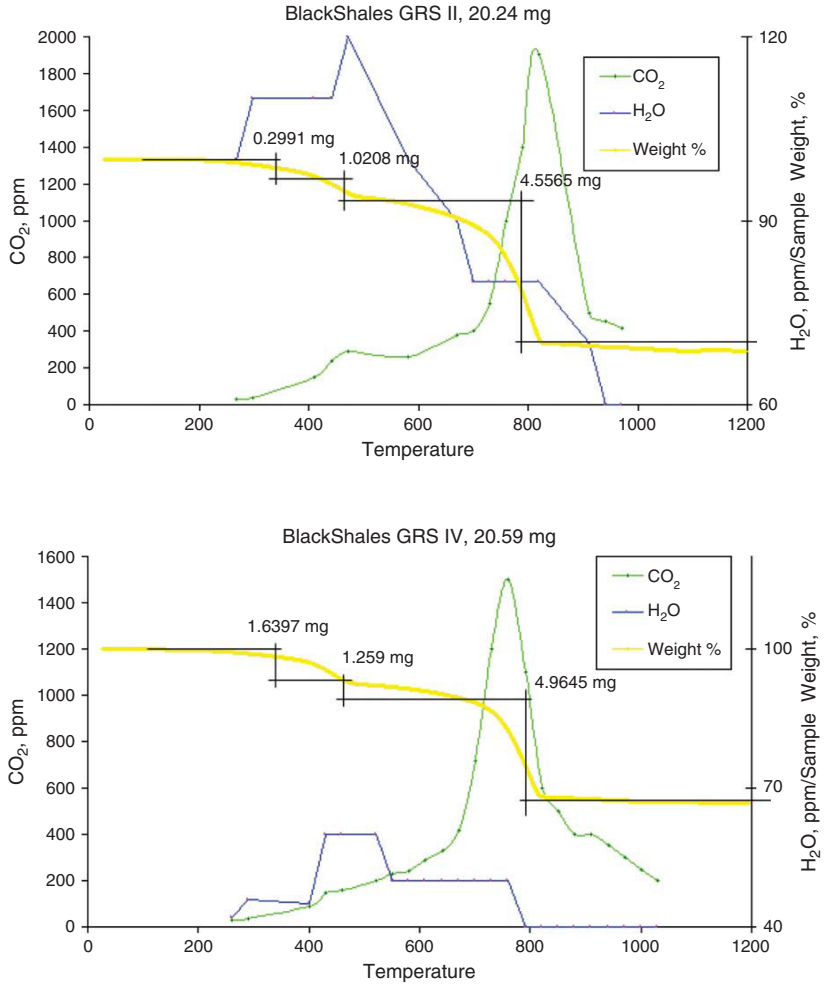

Fig. 2—Thermogravimetric analyses of Green River shale samples. Each figure displays the weight loss (yellow curve), carbon dioxide release (green curve), and water release (blue curve). Three main steps of mass release could be identified. From left to right, Step 1 corresponds to dehydration of clay minerals; Step 2 corresponds to the temperatures over which hydrocarbons are released and detected by GC; and Step 3 corresponds to decomposition of carbonate minerals at temperatures between 750 and 850°C.

because they had a wider range of gray-scale values, which spread well into the range of gray-scale values associated with the features of interest.

Image Analysis

The 2D and 3D image analyses of the shale samples were used for different purposes. The 2D images were used for 2D-image correlation analysis, and this allows the deformation field to be determined without image segmentation. The 3D images were used to study fracture nucleation, growth, and coalescence, and the evolving visible patterns provided information that was helpful in explaining the phenomena behind the fracturing behavior.

Analysis of the Strain Field Using 2D Image Correlation. Digital image correlation (DIC) (Hild and Roux 2006) analysis was performed on two orthogonal vertical slices of the tomographic images obtained as a Green River shale sample was heated. In each of these two planes, the evolution of both the vertical and the horizontal strain was determined as a function of temperature in the following way.

Each image (deformed image) was compared with the immediately preceding image. Around each pixel of the deformed image, a subimage of 25×25 pixels was extracted and correlated to the corresponding subimage in the reference image (the immediately preceding image). A 25×25 correlation matrix was obtained by multiplying the Fourier transforms (obtained using a fast-Fourier-transform algorithm) of both subimages (one being rotated by 180° to account for complex conjugation) before taking the inverse Fourier transform of the result. The maximum element of the correlation matrix was first located. A subpixel determination of the location of the maximum then was obtained by finding the maximum of the best (least-mean-square deviation) parabola representing the 3×3 correlation submatrix centered on the element with the maximum correlation. The x- and y- distance between this maximum and the center of the correlation matrix were assumed to be the x- and y- component of the displacement vector, for this pixel, from the reference to the deformed image.

The size of the subimages was chosen to be 25 after several sizes were tested. Before crack nucleation, displacements up to 5–6 pixels were measured between two successive images, and because the maximum displacement measurable with a subimage of size N is $N/4$, the minimum possible subimage size is $6 \times 4 = 24$ pixels. We then tested three different sizes—25, 37, and 49 pixels—which all gave results very similar to that shown in **Fig. 3,** within variations less than 11% for all temperatures below 350°C. This result strongly suggests that the correlation analysis is almost independent of the size of the subimage, provided that it is ≥ 25.

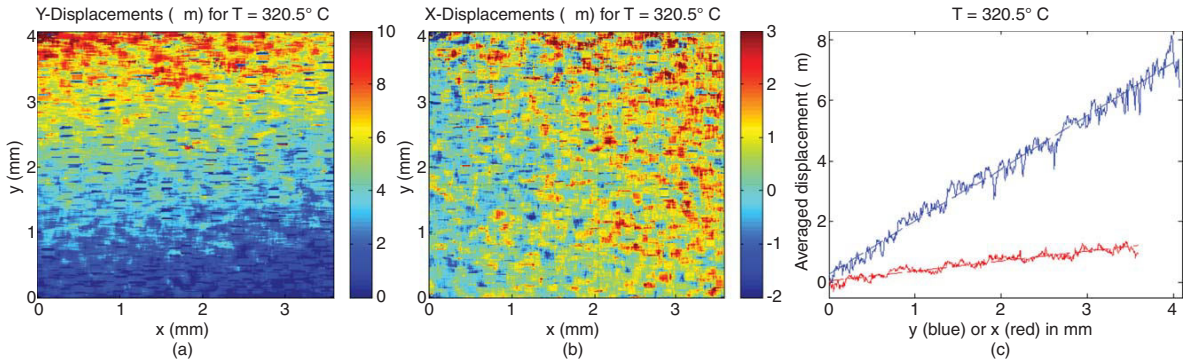

Fig. 3—Displacement fields measured by DIC between two successive images (T = 320.5°C) using a subimage area of 25×25 pixels. (a) Color map of the spatial distribution of the vertical (*y*-direction) displacements in μm (the bottommost line has an average vertical displacement of 0). (b) Color map of the spatial distribution of the horizontal (*x*-direction) displacements in μm (the leftmost line has an average horizontal displacement of 0). (c) Blue: vertical displacement averaged over *x*. Red: horizontal displacement averaged over *y*.

We then selected the smallest size among these three so that the spatial resolution of the displacement field was optimal, with minimal computational effort.

The correlation analysis provides the evolution of the incremental displacement field as the sample deforms because of heating **(Fig. 3)**. Limitations in the maximum displacement measured (see Discussion) prevented us from correlating all successive images to the first image. In other words, we had access only to displacement increments between successive image pairs, not to the absolute displacements. The total displacement can, of course, be obtained as the sum of all previous increments, but with the drawback that the noise level of the results will increase in proportion to the square root of the number of added incremental displacement fields.

For each image, we determined that the x-displacement averaged along the y-direction and the y- displacement averaged along the x-direction are linear function of x and y, respectively (Fig. 3c). This indicates that, upon heating, the thermal- expansion-strain increase is essentially homogeneous in both directions for this unconfined sample. The strain increment can therefore be represented by two scalar values, one for each direction, which are plotted as a function of temperature in **Fig. 4a.** The strain is anisotropic, and the horizontal strain increment (along the stratification) is significantly smaller [by a factor of approximately 2 to approximately 5 depending on the temperature (Fig. 4a)] than the vertical one (perpendicular to the stratification). Their values vary with temperature, indicating that the linear thermal-expansion coefficient (strain increment per unit degree) is itself a function of temperature. It is roughly constant from 60°C to approximately 290°C, with typical values of approximately 5×10^{-5}/degree in the vertical direction and approximately 2×10^{-5}/degree in the horizontal direction. Between 290 and 350°C, the vertical linear-thermal expansion coefficient increases quite rapidly with increasing temperature. The total strain at approximately 350°C, obtained by adding strain increments (Fig. 4b) reaches approximately 2% in the vertical direction and approximately 0.6% in the horizontal direction. All these results were almost the same for the two slices.

Above 350°C, cracks form and grow. These new features in the images have no equivalent in the previous images and this prevented us from using the correlation analysis for $T > 350$°C.

3D Image Analysis. A methodology was developed for 3D image analysis including several steps that should be followed carefully to obtain the best possible quantification of the crack network. Despite the application of powerful computer processing units, the size of the samples made the processing very slow. The selection of the best methods at each step to remove most of the unwanted data in the form of noise or features which are not of interest while keeping small features of interest was challenging.

Image Processing. The raw 3D X-ray tomography volumes must be analyzed to provide images, to extract features of interest, and to perform qualitative or quantitative analyses that can be used for interpretation. This analysis can be time consuming (up to 1 day) given the large size of each data set (each volume is represented by either 2048×2048×256 or 830×830×830 voxels, coded as 8- or 16-bit gray levels) and the need to develop a workflow for all the steps necessary for image processing, from filtering to 3D rendering and quantification of deformation patterns. However, this kind of processing is becoming more mainstream. Moreover, characterization of the nucleation, growth, and healing of cracks during thermal alteration was an important aspect of this study, and to achieve this, the microcracks must be distinguished from other low X-ray attenuation objects such as kerogen lenses and imaging artifacts. A filtering scheme, performed in several steps, that allows segmentation of the cracks is presented in **Fig. 5.** This is applicable to images of very tight rocks with distinguishable small-scale features (in this case microcracks). The software package Avizo Fire was used to develop the image-processing scheme. As shown in **Fig. 6,** small crack apertures (up to 5 voxels/25 μm) and the wide range of crack sizes make segmentation challenging. Sample displacement is also an issue that should be addressed during image reconstruction or at a later stage during data processing. For our images, displacement was not a significant issue because the samples that were analyzed did not undergo displacements that were large enough to affect the accuracy of the method adopted.

Primary Filtering, Preprocessing, and Masking. The microstructure of the rock is readily apparent in the primary 3D images. Apart from the typical imaging artifacts already mentioned, there can be other issues such as uneven illumination of the samples during the imaging process, Gaussian noise, "salt-and-pepper" noise, quantization noise, shot noise, and subvoxel features below the imaging resolution. While there are standardized techniques to deal with some of these sources of image noise, a number of them require user interaction and additional information about the object(s) of interest to properly distinguish between the noise and the signal.

A variety of filtering algorithms was tested, and their outputs were compared to determine which gave the best results.

These included: (1) three noise-reduction filters (minimum, median, and maximum) that replace the value of a pixel by the smallest, median, and largest value of the neighboring pixels using an $N \times N$ mask; (2) a Sobel edge-detection filter; (3) a resampling/low-pass filter based on convolution with a Lanczos kernel; and (4) an edge-preserving Gaussian filter.

The Sobel filter is a rotation-invariant edge-detection filter. This filter convolutes the image with 4 different kernels representing horizontal, vertical, and two arbitrary diagonal orientations, and each kernel consists of a combination of Gaussian

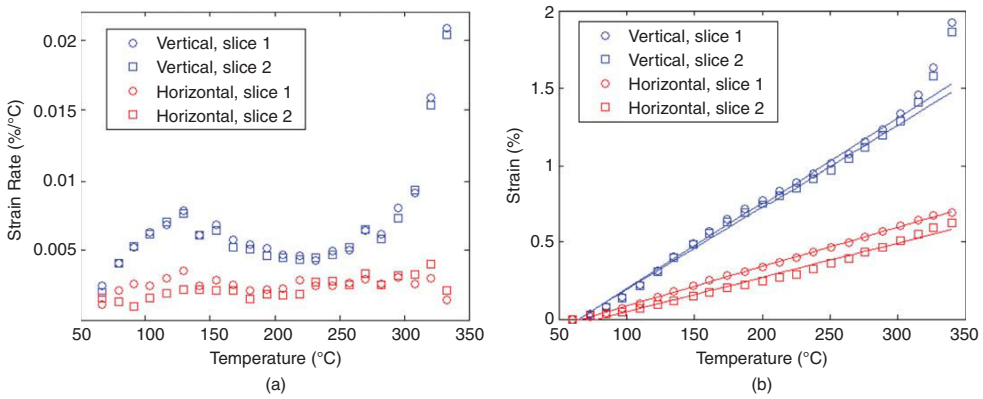

Fig. 4—(a) Evolution of the strain increment between two images. (b) Strain as a function of temperature, for both directions (vertical in blue, horizontal in red) and for two orthogonal vertical slices. The vertical strain/temperature curve deviates from linearity at temperatures of approximately 320°C, which corresponds to the onset of fracturing.

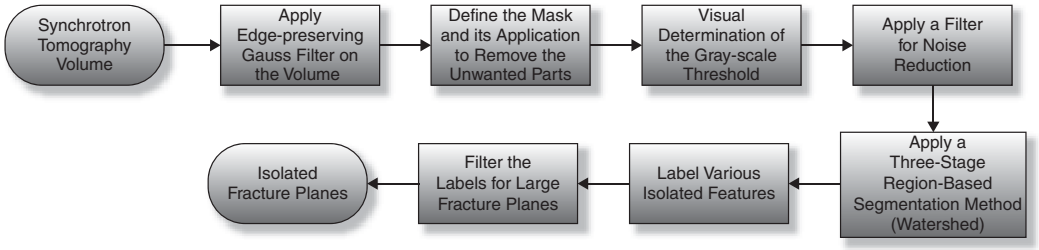

Fig. 5—Processing workflow diagram for the 3D tomogram.

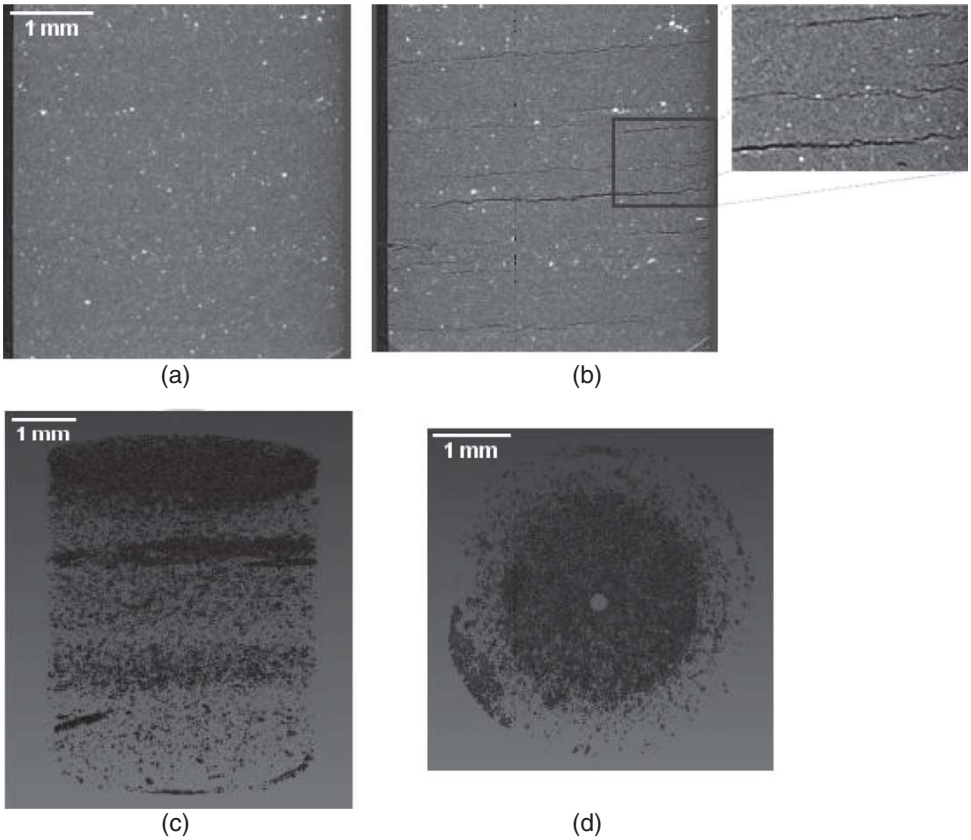

Fig. 6—Microtomography images of Green River shale. (a) 2D slice at the onset and (b) after heating (4 × 4 mm) showing that cracks began to appear at approximately 320°C. (c) and (d) 3D views of porosity showing small crack apertures (in the range 1–5 voxels/ 5 25 μm) and a wide range of crack sizes, which make the segmentation procedure challenging.

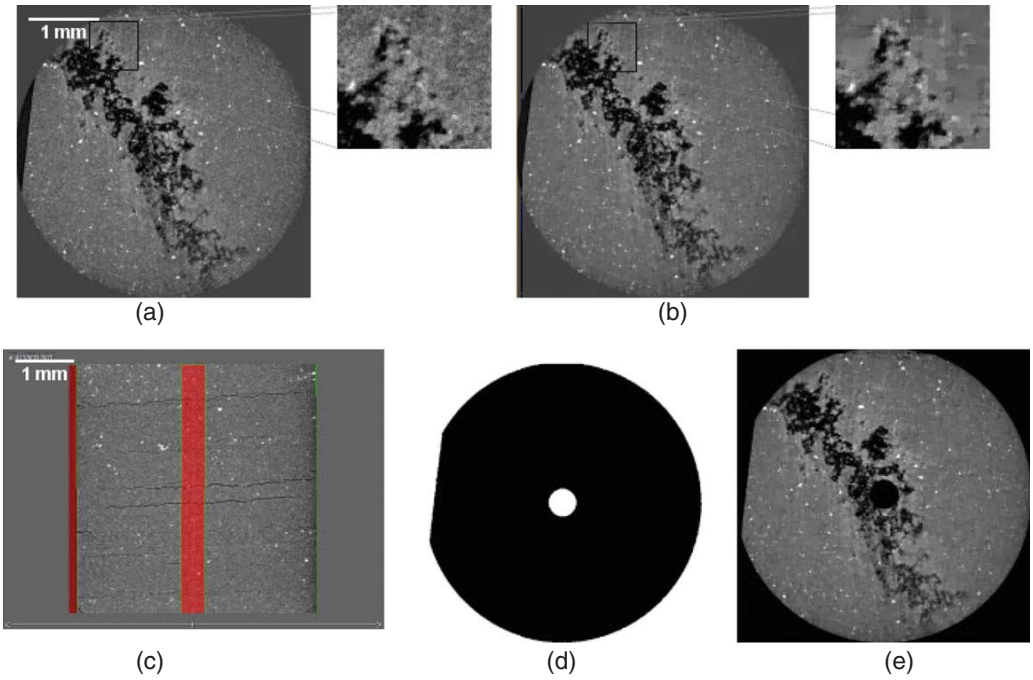

Fig. 7—Primary filtering and masking workflow. (a) Original volume showing a crack (dark area). (b) Gaussian filtered volume. (c) Definition of the mask (red areas) representing the areas that should be taken out of the processing. (d) The mask, and (e) masked and filtered volume. The center of the sample and an edge, where the noise was higher than in the rest of the sample, were removed.

smoothing/filter and differentiation in the proper orientation. The Lanczos filter indicates which features in the original data, and in what proportion, make up each feature in the final data (a statistical feature detection filter). This filter calculates the *n*th centralized moment of the data in a gliding window.

The edge-preserving Gaussian filter gave the most-satisfactory results. It preserved the outlines and areas of features of interest while removing most of the artificial features and/or natural features that were not of interest. A special type of Gaussian filter was used to preserve edges while smoothing the overall 3D image. This filter has an effect similar to the physical process of diffusion, which converts a delta function into a Gaussian (it smooths the gray-level intensity differences between neighboring voxels). However, it does not smear out edges because the "diffusion coefficient" is reduced to zero as edges are approached. The presence of distinctive particles such as pyrite particles helped us to select, customize, and calibrate the filtering technique and the relevant parameters. The blank part of the image, as well as parts of the samples that were chipped off during the coring process, and the central part of the sample with some noise, which established artificial vertical connectivity between the fracture planes, had to be removed and masked carefully before moving on to the next step **(Fig. 7).** Several techniques, such as the application of cluster-detection algorithms and geometric interpolation, were used in this process. Neighboring voxels with similar properties were grouped together by cluster detection. First, all of the voxels within a selected range of properties were given the same label. One of the labeled voxels was selected, recorded, and given a new label. Then, all of its nearest neighboring voxels of the newly labeled voxel were recorded and given a new label. In the next step, all of the nearest neighbors of the relabeled sites (with the exception of previously relabeled voxels) were relabeled and recorded, and the process was repeated until no more voxels with the original label could be found. The total list of recorded sites is a cluster. A new voxel with the original label was found, and the entire process was repeated to find the second cluster. The entire procedure was repeated as often as required until all of the clusters were located, and all of the initially labeled voxels were relabeled (Tout et al. 2007).

Image Binarization and Segmentation of the Cracks. A number of methods have been developed for segmentation of "foreground" objects from a "background" through simple thresholding, edge detection, active contour shape detection, and indicator kriging. The work presented here begins once the images have been converted to binary form to isolate various objects (i.e., the cracks, the pores, and the background solid matrix). These methods are described in depth in the scientific literature (Lindquist et al. 2000). A simple thresholding procedure was used to convert the 8-bit gray-scale images into binary form. The pore spaces and volumes were segmented using a specific range of gray values between 0 and 35 (out of 256 gray levels), where zero represents black (which corresponds to pores, which have no X-ray attenuation), as seen in **Fig. 8a.** The value of 35 was selected visually and by trial and error, with fracture-plane continuity as the goal. Besides, it was not possible to distinguish real features from artifacts if a threshold below 35 was selected. Choosing the threshold value of 35 introduces some errors; however, selecting values less than 35 results in artificially disconnected pore spaces, which do not adequately represent fracture planes. A threshold value of 35 includes voxels that represent volumes with microcracks smaller than 5 μm in diameter. When these smaller microcracks are excluded (i.e., use smaller threshold values), the fracture planes are disjointed. By including these smaller microcracks (< 5 μm), reconstruction of the fracture plane with greater continuity is possible. Thresholding was followed by noise-reduction filtering to make sure that visible cracks and other features do not disappear after this step (Fig. 8b). This was necessary and helped save a considerable amount of computation time in the next step.

In the next phase of this study, we will study transport phenomena inside the material and transport through its boundaries. Therefore, the connectivity of the pore spaces and crack apertures and their connectivity with the exterior must be captured and preserved. To preserve the fracture planes, a region-based segmentation method called the watershed method was used to form fracture planes from seemingly isolated, but densely grouped voxels with gray values approaching zero (Figs. 8c through 8g). This

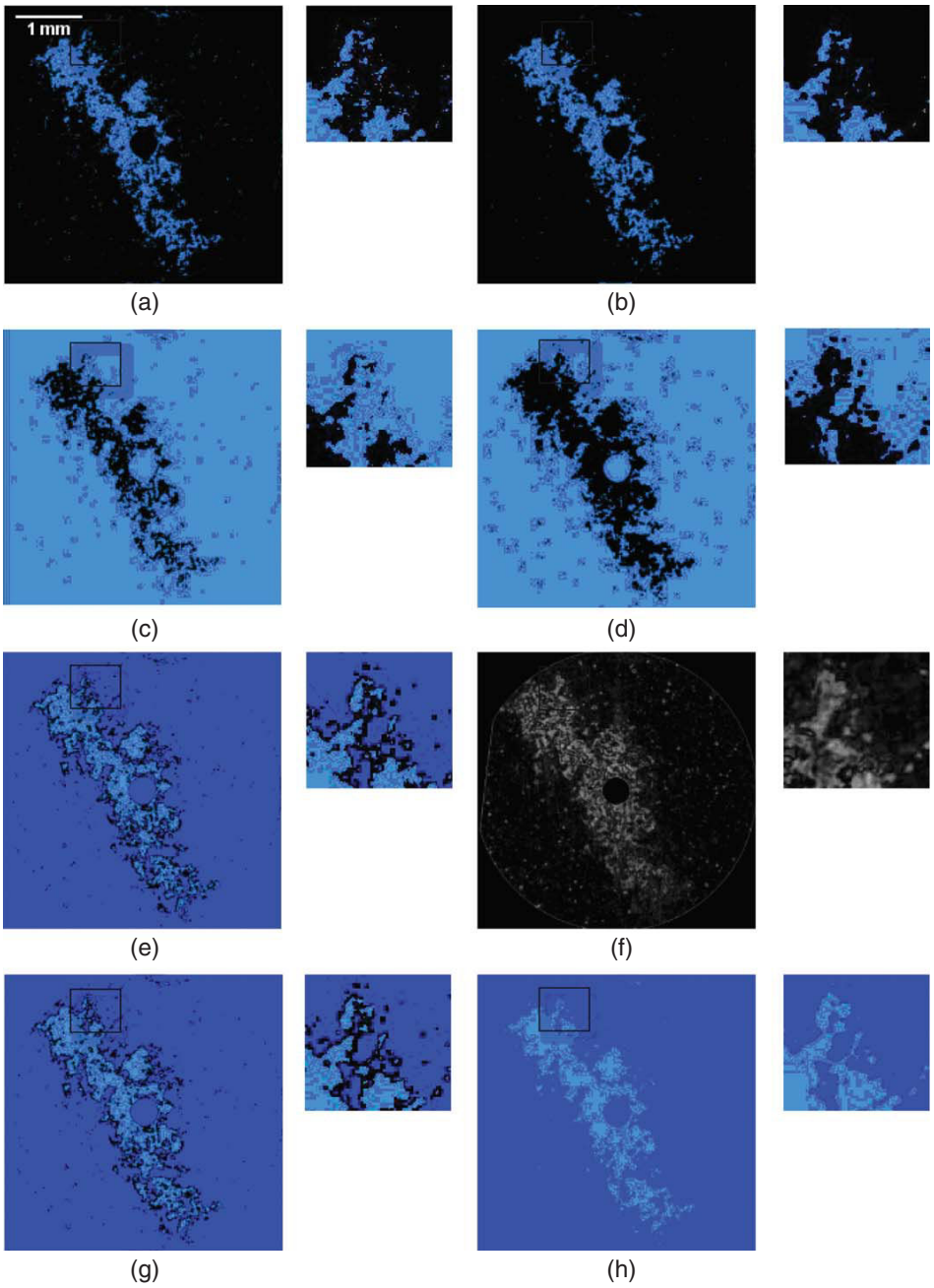

Fig. 8—Image-processing workflow. (a) Thresholded volume. (b) Noise-reduced volume. (c) Prewatershed markers Volume 0. (d) Prewatershed markers volume 1. (e) Watershed markers volume. (f) Gradient volume of the original volume. (g) Watershed volume. (h) Dilated watershed volume.

method was originally proposed by Lantuéjoul (1978). Contrary to simple cluster identification, separations obtained using the watershed algorithm are much more representative of the local geometry. The watershed method finds the "ridge lines" between neighboring "basins" (Vincent and Soille 1991). One minor inconvenience, also reported by others (Cendre et al. 1999), is that the separation is just one voxel thick, while our goal is to assign every voxel of the pore space to a pore. This necessitates postprocessing to assign these watershed voxels to an adjacent pore volume and smooth the fracture planes. The final product, despite all the filtering, is still a more-or-less continuous medium with small amplitude heterogeneity filled with a number of small-width crack apertures. To make sure that "cracks" artificially generated during image acquisition and processing were not interpreted as real cracks, only cracks larger than a certain size (10,000 connected voxels, below which the crack density drops by 3 orders of magnitude) were selected for quantitative description in terms of crack thickness, roughness, orientation, spatial correlation, displacement, and the strain field. Obviously, this filters out some of the real but small fractures, but a statistical study of the crack-size distribution was not part of this study. In **Fig 9,** filtering of some large-scale and oriented cracks from many small and scattered ones is shown; at the current resolution, it is difficult to determine any patterns formed by the small cracks. The large-scale fractures

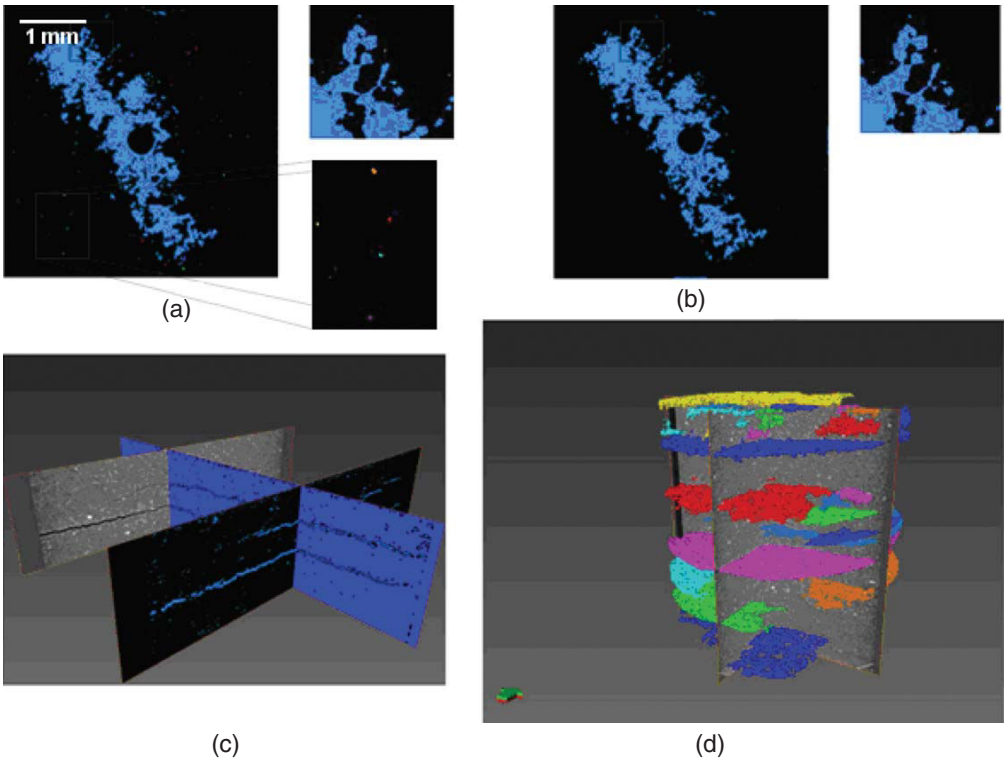

Fig. 9—Post-processing workflow. (a) Labeled volume. (b) Filtered labeled volume. (c) Isolated digitized cracks. (d) Filtered and labeled fracture planes.

are clearly oriented along the plane of the lamination, which is perpendicular to the coring direction.

Discussion

Digital correlation analysis (DIC) of both optical (Rechenmacher and Finno 2004; Bornert et al. 2010) and X-ray (Louis et al. 2007; Lenoir et al. 2007; Viggiani 2009) images is now widely used in experimental mechanics, particularly in geo-materials mechanics, and it is applied to 2D (Rechenmacher and Finno, 2004; Hild and Roux 2006; Louis et al. 2007; Bornert et al. 2010; Kobchenko et al. 2011) and 3D (Lenoir et al. 2007; Viggiani 2009) images. The fact that the 2D digital image correlation analysis of Green River shale during heating was successful indicates that uncontrolled rigid-body motion of the sample was sufficiently small that correlation between one image and the next was not lost. Similarly, the rigid-body motion was small enough for the strain fields (the derivatives of the displacement field) to be determined.

DIC allowed us to quantify the evolution of the linear thermal-expansion coefficient with temperature. Depending on the direction relative to the bedding plane, the linear thermal-expansion coefficient is typically 2 to 5 times smaller in the horizontal direction, parallel to the bedding plane, than in the vertical direction. Depending on the temperature, we found vertical linear thermal-expansion coefficients between approximately 2×10^{-5} and 20×10^{-5}/°C. These values may be compared with, and they were found to be in good agreement with, the reported *volumetric* thermal-expansion coefficients of the kerogen in Green River shales and for the mineral matrix in which it is embedded. The latter is reported to be in the range 2×10^{-5} to 5×10^{-5}/°C (e.g., Settari and Walters 2001; Chen et al. 2003), whereas the former is in the range 10×10^{-5} to 30×10^{-5}/°C below 145°C (the glass temperature of the kerogen) and in the range 55×10^{-5} to 60×10^{-5}/°C above 145°C (Zhang and LeBoeuf 2009).

The spatial resolution of the measured displacement fields is limited by the size of the sub-images used for correlation [of the order of ten pixels, (i.e., 50 μm)]. At each pixel, the measured displacement has a typical resolution of a tenth of the pixel size (i.e., 500 nm). The maximum displacement distance that can be measured accurately with the correlation analysis approach used here is approximately one-quarter of the sub-image size (6 pixels for subimages of 25-pixel size) so that larger displacements were discarded (the proportion of discarded pixels was less than 1.6% at all temperatures below 350°C). As mentioned earlier, this prevented us from correlating most of the images with the initial image to determine total displacements directly. In principle, larger displacements could be measured directly, by changing the correlation procedure, but this would be at the expense of a higher computation cost.

In this work, we limited the correlation analysis to 2D slices of the volume image and did not attempt a computationally demanding 3D correlation analysis. In practice, this was not a limitation for the study of the macroscopic strain before the onset of fracturing because the behaviors determined for the two orthogonal slices extracted from the 3D volume were almost identical, and they are, therefore, representative of the behavior of the whole volume. After fracturing began, open cracks significantly altered the images, thus preventing application of the correlation analysis described in this paper, be it 2D or 3D. In this case, 3D image analysis proved to be an efficient tool to monitor crack propagation and coalescence. In future work, 3D correlation analysis could, in principle, be used to determine the locations of crack-nucleation sites and identify precursors to crack nucleation once the cracks or their precursors become large enough to result in a voxel gray-scale value equal to or less than 35. In reality, undetected nanocracks (and even smaller scale damage) are likely to be microcrack precursors. However, we anticipate that it would be difficult to distinguish small-scale/small-amplitude precursors from the imaging/correlation noise. As a consequence, we used 2D correlation analysis before crack nucleation and we then used 3D image analysis to investigate crack nucleation and growth.

X-ray CT can be used for quantitative and qualitative analysis of internal features only if those features are revealed by sufficiently great differences in atomic composition and/or density.

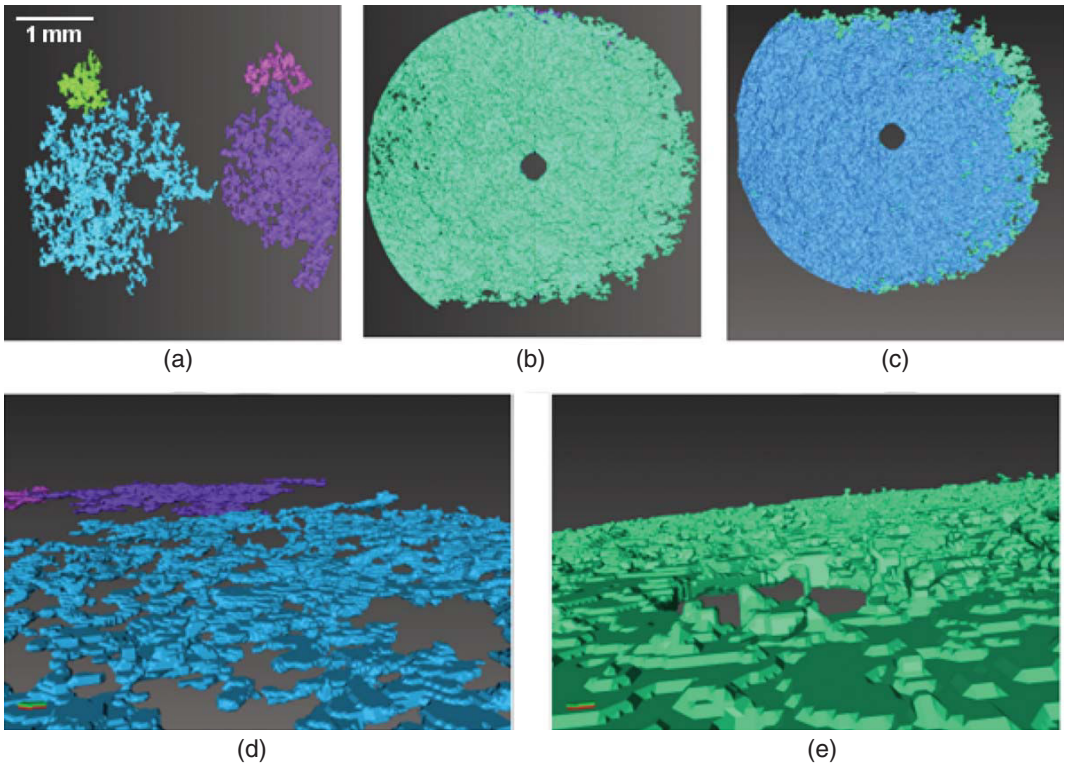

Fig. 10—Imaging of a single fracture. (a) Crack appearance at an early stage of growth. (b) Cracks merging into one another. (c) Overprint of the crack long after reaching the boundary in blue on the one at the onset of hitting the boundary in green. (d) Cracks show out-of-plane fluctuations. (e) Surface roughness of the merged cracks.

Pronounced variations in X-ray attenuation coefficients are required to distinguish two substances in the CT images. A strong contrast exists between solid phases and air-filled pore volumes, and in our case, there was a clear contrast between the cracks and mineral phases. However, the contrasts between other components are smaller, and our experimental/synchrotron setup did not allow us to distinguish between kerogen-containing pore spaces (kerogen lenses) and cracks filled with gas/kerogen mixtures.

Using the 4D CT image analysis results, it can be seen that individual microcracks propagate by means of small local advances in the crack front, which are controlled by the heterogeneity and evolving stress/strain field. The nature of the crack propagation and the geometries of both individual microcracks and the ensemble of microcracks generated in the heating experiment suggest that the process that generates them may be related to percolation or invasion percolation. The standard percolation model is physically realistic because kerogen is distributed more or less randomly along bedding planes throughout the organic-rich rock and decomposes to produce fluids everywhere. However, it would be very surprising if the evolving stress field played no role in the process. A modified percolation or invasion model may be more realistic **(Fig. 10).** The nucleation and growth of cracks in heterogeneous media owing to the internal production of fluids is a complex phenomenon that has not been investigated in detail. Phase separation of gas dissolved in a liquid can be brought about by changing the composition (the gas/liquid ratio), the pressure, or the temperature. In simple liquids, more-or-less- spherical gas-filled bubbles are formed through nucleation and growth during the early stages of phase separation (while the gas/liquid volume ratio is small). However, if the phase separation takes place in a gel, the gas-filled volumes are more like penny-shaped cracks than spherical bubbles (Renard et al. 2009; Boudreau et al. 2005), and under these conditions, bubbles and cracks are indistinguishable. In particular, the production of gases in mud that consists of a 3D gel network of fine particles, which penetrate a volume of aqueous fluid, results in the formation of penny-shaped gas-filled cracks that can be seen in X-ray tomography images (Boudreau et al. 2005). In the case of kerogen-rich rocks, hydrocarbon fluids are formed inside the kerogen particles, and fracturing could be initiated by phase separation inside the kerogen. The molecular architecture of the Type I kerogen in the Green River shale can be thought of as a 3D gel-like (crosslinked-polymer) network. However, bubble/crack nucleation could occur on kerogen/mineral interfaces or the interfaces between liquid-filled pores and minerals or the interfaces between liquids and kerogen. The X-ray images suggest the growth of bubbles or cracks in a heterogeneous medium. It is surprising that the cracks are not more like penny-shaped cracks when they are small, but the Green River shale is much more heterogeneous than synthetic gels or mud, particularly on scales greater than the gel network correlation length (typically smaller than 1 μm).

Although the possibility that small cracks might be present in the materials that we investigated or could have been created when the specimens were collected or when cores and thin sections were prepared cannot be ruled out, but no evidence was found for such fractures in either the thin sections or the cores used in the present study.

In the heating experiment, the sample was heated continuously for 340 minutes as the temperature rose from 60 to 400°C at the constant rate of 1°C/min. It took 20 minutes to image each sample, and 17 images were recorded during the heating stage. An additional 51 images (Images 18–68) were acquired every 20 minutes at a constant temperature of 400°C. Out of the inspected images, quite a large number of very small cracks appeared in Image 23, and by Image 28 out of the 68-image sequence, these microcracks had grown and coalesced into much larger cracks (Fig. 10). The small sizes of the cracks, particularly when they first appear, increases the challenge of robust segmentation. To distinguish between the kerogen patches, which were originally present, and the evolving fluid-filled cracks, it is important to use

information from the preceding images. Without this information, it is not possible to differentiate between kerogen and other forms of hydrocarbons generated by means of kerogen decomposition because they have similar X-ray attenuation coefficients. Even-higher tomographic resolutions would be required to investigate whether cracks nucleate within kerogen patches, at kerogen/mineral interfaces, or elsewhere. Again, comparison of successive images would be needed to distinguish between cracks and pores, which have characteristic dimensions smaller than the size of the voxels used in the work reported here. Image correlation analysis could also be used to indirectly detect early-stage cracks with sub-voxel-scale apertures by means of the displacements associated with them.

A possible explanation for the peak in the strain curve at approximately 120°C (Fig. 4) is dehydration of clay minerals such as smectites. The second peak can be explained by the volume change because of kerogen decomposition, and other processes such as oxidation of organic matter may occur when the temperature reaches approximately 320°C.

The crack-aperture decreases when the crack front reaches the boundary of the sample (Fig. 10c). This suggests that the pressure generated by the low-molecular-weight kerogen-decomposition products inflates the cracks, and that this pressure is released when the cracks reach the exterior. This observation also supports the hypothesis that fracturing is caused by fluid generation, and that the excess pressure inside the cracks drives crack growth. The cracks all have more or less the same orientations, which are apparently controlled by the strongly anisotropic sedimentary morphology (i.e., lamination). The TEM, XRF, and SEM images indicate that some elements are concentrated on the laminations. Damage was observed to initiate at multiple locations within the same interface between two laminations, and the microfractures (damage zones) grow within an interface. Then damaged regions expand and finally interconnect to form a fracture that spans the entire sample. Obviously under subsurface conditions, except at very small depths, the confinement might keep the fracture closed or the aperture might not be large enough to be visible at micron-scale resolution. Another issue that has not been considered here is the correspondence of hydrocarbon escape rate to the time resolution of the X-ray tomography experiment.

One of the main objectives of these experiments was to investigate the applicability of time-lapse high-resolution synchrotron CT to study the evolution of a model source rock during heating. The next step will be to study the same process under confinement—under conditions more similar to those that prevail during natural primary migration. Of course, the time scale of any practical laboratory experiment will be shorter than the time scale of natural kerogen decomposition by many orders of magnitude. This will make fracturing more likely in the experiments because there will be much less time for the fluids produced by kerogen decomposition to migrate by flow or diffusion. However, we do expect that experiments under confinement will lead to important insights into the mechanisms of natural primary migration. The time scales associated with the commercial production of hydrocarbon fluids from oil shales, such as the Green River shale, are much shorter (hours for surface retorting and years for in-situ, subsurface, retorting). The results reported here are directly relevant to surface retorting, and experiments with small confining stresses (0.2–20 MPa) would be relevant to in-situ production.

Conclusion

4D (three space dimensions + time) X-ray CT was performed using synchrotron beam lines that made it possible to acquire images at resolutions of a few microns with short scanning time, among other benefits (monochromatic beam to avoid beam hardening). We have shown how the deformation and fracturing of shales during heating can be investigated using X-ray tomography, and a workflow was developed to extract very small crack apertures from microtomography images of tight- rock samples. This workflow could be modified and customized to extract other features for other geomaterials and other processes that lead to deformation or fracturing and deformation. A conceptual model was presented, which explains why and where these cracks nucleated and how they grew and finally merged together. It has been shown how 3D X-ray tomography detection and analysis of fractures can be supported by 2D correlation analyses.

For the Green River shale sample that was used to investigate the growth of cracks under heating and without confinement, the following observations can be made:

- On micrometer scales, crack nucleation, growth, and coalescence does not occur randomly. Instead, it was observed that cracks nucleate and grow in regions with the highest material heterogeneities in which the highest stress concentrations also occur. Expansion of the organic material present in the shale samples and its transformation into gas explains the stress buildup. Individual cracks grow in the bedding plane in which they are located until they meet other cracks or reach the boundary of the shale sample. The aperture widths of the cracks do not change substantially when they grow, but once the cracks reach the sample boundaries, their aperture widths decrease.
- On larger scales, a set of parallel fractures grow, and the common orientation of the fractures is controlled by the natural lamination.
- The strain increases homogeneously along both the *x*- and *y*-direction. However, the strain is found to be anisotropic, and the horizontal strain increment (along the stratification) is significantly smaller (by a factor of approximately 2 to 5, depending on the temperature) than the vertical strain (perpendicular to the stratification).
- The approach taken here, which combines 2D image analyses with 3D image analyses, has the advantage of compensating for the shortcomings of each approach. The quantitative 2D analysis was complemented by qualitative 3D analysis, and it was shown that the 2D results are characteristic of the 3D behavior.

Acknowledgments

We would like to thank Anne-Céline Ganzhorn, Berit Osteby, Elodie Boller at ESRF, and Samuel McDonald at SLS for their help during the acquisition of tomography data. Rodica Chiriac from LMI laboratory at the University Claude Bernard in Lyon performed the thermogravimetry analyses.

References

Arns, C.H., Knackstedt, M.A., Pinczewski, M.V. et al. 2001. Accurate estimation of transport properties from microtomographic images. *Geophys. Res. Lett.* **28** (17): 3361–3364. http://dx.doi.org/10.1029/2001gl012987.

Bornert, M., Valès, F., Gharbi, H. et al. 2010. Multiscale Full-Field Strain Measurements for Micromechanical Investigations of the Hydromechanical Behaviour of Clayey Rocks. *Strain* **46** (1): 33–46. http://dx.doi.org/10.1111/j.1475-1305.2008.00590.x.

Boudreau, B.P., Algar, C., Johnson, B.D. et al. 2005. Bubble growth and rise in soft sediments. *Geology* **33** (6): 517–520. http://dx.doi.org/10.1130/g21259.1.

Bracewell, R.N. 1990. Numerical Transforms. *Science* **248** (4956): 697–704. http://dx.doi.org/10.1126/science.248.4956.697.

Bray, E.E. and Foster, W.R. 1980. A process for primary migration of petroleum. *AAPG Bull.* **64** (1): 107–114.

Cendre, E., Duvauchelle, P., Peix, G. et al. 1999. Conception of a High Resolution X-Ray Computed Tomography Device; Application To Damage Initiation Imaging Inside Materials. *Proc.*, 1st World Congress on Industrial Process Tomography, Buxton, Greater Manchester, UK, 14–17 April, 362–369.

Chanchani, J., Berg., R.R., and Lee, C.-I. 1996. Pressure solution and microfracturing in primary oil migration, Upper Cretaceous Austin Chalk. *GCAGS Transactions* **46:** 71–78. http://dx.doi.org/10.1306/2DC40B13-0E47-11D7-8643000102C1865D.

Chen, G., Chenevert, M.E., Sharma, M.M. et al. 2003. A study of wellbore stability in shales including poroelastic, chemical, and thermal effects. *J. Pet. Sci. Eng.* **38** (3–4): 167–176. http://dx.doi.org/10.1016/s0920-4105(03)00030-5.

Cordell, R.J. 1973. Colloidal Soap as Proposed Primary Migration Medium for Hydrocarbons. *AAPG Bull.* **57** (9): 1618–1643.

Danilatos, G.D. 1988. Foundations of Environmental Scanning Electron Microscopy. In *Advances in Electronics and Electron Physics*, ed. P.W. Hawkes, Vol. 71, 110–248. San Diego, California: Academic Press.

Deans, S.R. 1983. *The Radon Transform and Some of Its Applications*. New York: John Wiley & Sons.

England, W.A., MacKenzie, A.S., Mann, D.M. et al. The movement and entrapment of petroleum fluids in the subsurface. *J. Geol. Soc. London* **144:** 327–347.

Hermanrud, C., Doré, A.G., Augustson, J.H. et al. ed. 1993. *Basin Modelling: Advances and Applications (Proceedings of the Norwegian Petroleum Society Conference, March 13–15, Stavanger, Norway)*. Amsterdam, The Netherlands: Elsevier Science.

Hild, F. and Roux, S. 2006. Digital Image Correlation: from Displacement Measurement to Identification of Elastic Properties – a Review. *Strain* **42** (2): 69–80. http://dx.doi.org/10.1111/j.1475-1305.2006.00258.x.

Hunt, J.M. 1995. *Petroleum Geochemistry and Geology*, second edition. New York: W.H. Freeman.

Kobchenko, M., Panahi, H., Renard, F., et al. 2011. 4D imaging of fracturing in organic-rich shales during heating. *J. Geophys. Res.* (116) B12201. doi:10.1029/2011JB008565.

Lafargue, W., Espitalie, J., Broks, T.M. et al. 1994. Experimental simulation of primary migration. *Org. Geochem.* **22** (3–5): 575–586. http://dx.doi.org/10.1016/0146-6380(94)90126-0.

Lantuéjoul, C. 1978. *La squelettisation et son application aux mesures topologiques des mosaïques polycristallines*. PhD thesis, Ecole des Mines de Paris, Paris, France.

Lash, G.G. and Engelder, T. 2005. An analysis of horizontal microcracking during catagenesis: Example from the Catskill delta complex. *AAPG Bull.* **89** (11): 1433–1449. http://dx.doi.org/10.1306/05250504141.

Lenoir, N., Bornert, M., Desrues, J. et al. 2007. Volumetric Digital Image Correlation Applied to X-ray Microtomography Images from Triaxial Compression Tests on Argillaceous Rock. *Strain* **43** (3): 193–205. http://dx.doi.org/10.1111/j.1475-1305.2007.00348.x.

Levoy, M. 1992. Volume Rendering using the Fourier Projection-Slice Theorem. Technical Report CSL-TR-92-521, Departments of Electrical Engineering and Computer Science, Stanford University, Stanford, California (April 1992), http://www-graphics.stanford.edu/papers/fourier/Levoy_GI92_VolumeRendering.pdf.

Lindquist, W.B., Venkatarangan, A., Dunsmuir, J. et al. 2000. Pore and throat size distributions measured from synchrotron X-ray tomographic images of Fontainebleau sandstones. *J. Geophys. Res.* **105** (B9): 509–527.

Louis, L., Wong, T.-F., and Baud, P. 2007. Imaging strain localization by X-ray radiography and digital image correlation: Deformation bands in Rothbach sandstone. *J. Struct. Geol.* **29** (1): 129–140. http://dx.doi.org/10.1016/j.jsg.2006.07.015.

Mann, U. 1994. An integrated approach to the study of primary petroleum migration. *Geological Society, London, Special Publications* **78** (1): 233–260. http://dx.doi.org/10.1144/gsl.sp.1994.078.01.17.

McAuliffe, C.D. 1979. Oil and Gas Migration–Chemical and Physical Constraints. *AAPG Bull.* **63** (5): 761–781.

Mees, F., Jacobs, P., Swennen, R. et al. 2003. *Applications of Computerized X-ray Tomography in Geology and Related Domains*, No. 215, 1–6. London: Geological Society.

Price, L.C. 1989. Primary petroleum migration from shales with oxygen-rich organic matter. *J. Pet. Geol* **12** (3): 289-324. http://dx.doi.org/10.1111/j.1747-5457.1989.tb00198.x.

Rechenmacher, A.L. and Finno, R.J. 2004. Digital Image Correlation to Evaluate Shear Banding in Dilative Sands. *Geotech. Test. J.* **27** (1). http://dx.doi.org/10.1520/GTJ11263J.

Renard, F., Bernard, D., Thibault, X. et al. 2004. Synchrotron 3D microtomography of halite aggregates during experimental pressure solution creep and evolution of the permeability. *Geophys. Res. Lett.* **31** (7): L07607. http://dx.doi.org/10.1029/2004gl019605.

Renard, F., Dysthe, D.K., Feder, J.G. et al. 2009. Pattern formation during healing of fluid-filled cracks: an analog experiment. *Geofluids* **9** (4): 365–372. http://dx.doi.org/10.1111/j.1468-8123.2009.00260.x.

Rudkiewicz, J.L., Brévart, O., Connan, J. et al. 1994. Primary migration behaviour of hydrocarbons: from laboratory experiments to geological situations through fluid flow models. *Org. Geochem.* **22** (3–5): 631–639. http://dx.doi.org/10.1016/0146-6380(94)90129-5.

Schiffbauer, J.D. and Xiao, S. 2009. Novel application of focused ion beam electron microscopy (FIB-EM) in preparation and analysis of microfossil ultrastructures: A new view of complexity in early Eukaryotic organisms. *PALAIOS* **24** (9): 616–626. http://dx.doi.org/10.2110/palo.2009.p09-003r.

Settari, A. and Walters, D.A. 2001. Advances in Coupled Geomechanical and Reservoir Modeling With Applications to Reservoir Compaction. *SPE J.* **6** (3): 334–342. SPE-51927-PA. http://dx.doi.org/10.2118/51927-MS.

Snarsky, A.N. 1964. Relationship between primary migration and compaction of rocks. *Petroleum Geology* **5** (7): 362–365 (trans. from the original, Geologiya Nefti i Gaza 1961).

Terzi, S., Boller, E., Salvo, L. et al. 2009. *In situ* X-ray microtomography study of the solidification and remelted microstructures of Al-Cu alloys. *Int. J. Cast Met. Res.* **22** (1–4): 275–278. http://dx.doi.org/10.1179/136404609X368028.

Tissot, B. and Pelet, R. 1971. Nouvelles données sur les mécanismes de genèse et de migration du pétrole. Simulation mathématique et application à la prospection. *Proc.*, 8th World Petroleum Conference, Moscow, 13–18 June, 35–46.

Tissot, B.P. and Welte, D.H. 1978. *Petroleum Formation and Occurrence: A New Approach to Oil and Gas Exploration*. New York: Springer-Verlag.

Tout, S., Sun, J., and Sverdlik, W. 2007. A Hybrid Approach to Cluster Detection. *IAENG International Journal of Computer Science* **34** (1): 105–110.

Viggiani, G. 2009. Mechanisms of localized deformation in geomaterials: an experimental insight using full-field measurement techniques. In *Mechanics of Natural Solids*, ed. D. Kolymbas and G. Viggiani, 105–126. Berlin, Germany: Springer-Verlag.

Vincent, L. and Soille, P. 1991. Watersheds in digital spaces: an efficient algorithm based on immersion simulations. *IEEE Trans. Pattern Anal. Mach. Intell.* **13** (6): 583–598. http://dx.doi.org/10.1109/34.87344.

Wevers, M., de meester, P., and Swennen, R. 2000. Microfocus X-ray Computer Tomography in Materials Research. *Proc.*, 15th World Conference on Non-Destructive Testing (Roma 2000 15th WCNDT), Rome, 15–21 October, http://www.ndt.net/article/wcndt00/papers/idn399/idn399.htm.

Zhang, L. and LeBoeuf, E.J. 2009. A molecular dynamics study of natural organic matter: 1. Lignin, kerogen and soot. *Org. Geochem.* **40** (11): 1132–1142. http://dx.doi.org/10.1016/j.orggeochem.2009.08.002.

Paper 3

Drainage fracture networks in elastic solids with internal fluid generation

Maya Kobchenko[1], Andreas Hafver[1], Espen Jettestuen[1], Olivier Galland[1], François Renard[1,2], Paul Meakin[1,3], Bjørn Jamtveit[1] and Dag K. Dysthe[1]

[1]Physics of Geological Processes, University of Oslo, Norway;
[2]Univ. Joseph Fourier, ISTerre, BP 53, F-38041 Grenoble;
[3]Temple University, Department of Physics, Barton Hall, Philadelphia, PA 19122-6082

Europhysics Letters (in press).

Drainage fracture networks in elastic solids with internal fluid generation

Maya Kobchenko[1], Andreas Hafver[1], Espen Jettestuen[1], Olivier Galland[1], François Renard[1,2], Paul Meakin[1,3], Bjørn Jamtveit[1] and Dag K. Dysthe[1]

[1] *Physics of Geological Processes, University of Oslo, Norway;*
[2] *Univ. Grenoble 1, ISTerre, BP 53, F-38041 Grenoble;*
[3] *Temple University, Department of Physics, Barton Hall, Philadelphia, PA 19122-6082*

PACS 64.60.aq – Networks
PACS 47.70.-n – Fluid flow; reactive, radiative and nonequilibrium
PACS 64.60.av – Cracks, sandpiles, avalanches, and earthquakes

Abstract –Experiments in which CO_2 gas was generated by the yeast fermentation of sugar in an elastic layer of gelatine gel confined between two glass plates are described and analyzed theoretically. The CO_2 gas pressure causes the gel layer to fracture. The gas produced is drained on short length scales by diffusion and on long length scales by flow in a fracture network, which has topological properties that are intermediate between river networks and hierarchical fracture networks. A simple model for the experimental system with two parameters that characterize the disorder and the intermediate (river-fracture) topology of the network was developed and the results of the model were compared with the experimental results.

Introduction. – The formation of many branched, hierarchical networks such as rivers, blood vessels, leaf veins, lightning, etc. are the responses of physical systems to the transport of fluids, substances dissolved in fluids or charge. Such directed tree networks are efficient transport systems and they have characteristic statistical properties [1–4]. It has been postulated that river networks and the landscapes associated with them minimize hydrodynamic energy dissipation [3]. The evolution of river networks is controlled primarily by erosion, an interaction between flowing water and the landscape that does not extend beyond the local drainage basin [4].

Fracture networks are localized strain responses to stress beyond the elastic limits of solids and the fracture network characteristics can reveal the nature of the elastic loading, be it external shear, compression or tension, or generated by material shrinkage [5–7] or by overpressured fluids inside the solid [8]. Even if the fluid pressure in fractures is increased only locally, the elastic interactions are *long ranged* and local pressure increases may have long range effects such as triggering earthquakes [9, 10]. While the statistical topology of river networks has been investigated for almost 70 years [11], the statistical description of fractures [12] has only recently been extended to fracture network topologies [13].

Hydraulic fracturing, used by the petroleum industry to enhance the permeability of reservoir rocks, is induced by injecting a fluid at high pressure into the rock via a cased, cemented and perforated well. In some geological processes large fluid pressures are generated pervasively inside very large rock volumes and the fluid is expelled and transported out of the system. For example, in subduction zones hydrous minerals are subject to increasing pressure and temperature until they are no longer thermodynamically stable and form anhydrous minerals and hydrous fluids with a smaller solid volume but larger total (solid plus fluid) volume [9]. Magmas are formed by partial melting of the Earth's mantle, the melt segregates and moves through the crust to form volcanic intrusions, oceanic crust and volcanoes [14]. As they are progressively burried, organic rich shales are heated and the organic material is thermally decomposed into low molecular mass hydrocarbons with lower densities and viscosities. The transport of these lighter hydrocarbons through the virtually impermeable shale to adjacent high permeability rock layers is called primary migration and if the shale layer is thick the hydrocarbon drainage must occur via fractures generated in the shale [15].

Although the generation and drainage of fluids in subduction zones, magmas and organic rich shales have each

been extensively investigated, the focus of these investigations has been on physical, chemical and geological details rather than generic phenomena. In all of these systems, the solid is under confining stress, a fluid is generated internally in the solid and above some length scale, the fluid migrates through fractures generated in the solid. Here, a set of experiments, a simple theory and an algorithmic model for a system with these characteristics are presented. This system demonstrates the evolution of a new class of networks, drainage fracture networks that are intermediate between river networks and hierarchical fracture networks. River-like drainage networks with loops has been mentioned as topologically possible, but less efficient, network in studies of transport efficiency [1]. Here we explore the physical reasons why they exist in our experiments and possibly in Nature.

Experimental set-up. – The experimental set-up consists of a Hele-Shaw cell with a gel containing water, gelatin, sugar and yeast. When the yeast consumes the sugar it produces CO_2 and CO_2 bubbles nucleate and evolve into gas filled fractures. The gas is transported along these cracks to the edges of the gel layer. The Hele-Shaw cell consists of two 300x300x10 mm glass plates clamped together and separated by 3 mm.

The Hele-Shaw cell was filled with liquid gelatine solution after cleaning the inner surfaces with detergent and distilled water to ensure good adhesion between gelatine and glass. A gelatin solution was prepared by dissolving 58 g of gelatine sheets (from Gelita) in 1 dm^3 of boiling water (100° C). 7.5 g of sugar was dissolved in the gelatine solution, which was then cooled to 30° C, mixed with 2.5 g of baking yeast and stirred well to homogenize it. Half of the liquid solution was poured into an area of L×L, L=250 mm of the Hele-Shaw cell and the other half was poured into a bottle connected to a gas volume meter. Both solutions were kept in a refrigerator at 6° C for 10 hours to obtain a solid, homogeneous gel. It is assumed that the yeast particles are homogeneously distributed on large scales and variations in the particle size and local number density (and gas production rate) are treated as quenched disorder.

Four experiments were conducted under similar conditions at room temperature (17 ± 1° C), where the gelatine is a transparent, brittle, nearly elastic solid [16]. Two experiments (Exp_1, Exp_2) were performed with the same concentration of yeast and sugar (as described above). In the other two experiments (Exp_3, Exp_4) half and double the amounts of yeast and sugar were used. At 17° C, yeast is activated, consumes sugar and produces CO_2 gas. Fracture nucleation and propagation was imaged every minute at a resolution of 9 pixels/mm. Measurements of the bubble sizes and fracture apertures have an estimated accuracy of ±0.1 mm. Digital image correlation analysis showed that the motion of the camera was ≤ 1 pixel length.

Results. – After ≈ 2 hours fracture nucleation and growth began and the fractures transported gas to the edges of the gel. Development of the fracture pattern continued for an additional 20 hours until the "final" pattern, shown in Figure 1, was obtained.

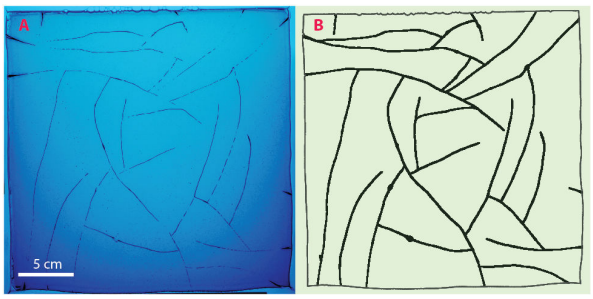

Fig. 1: Original and processed optical images of Exp_1. **A:** Original image of fracture pattern at time t=22h. **B:** Processed binary image used for further analysis of network topology and geometry. The boundary of the gelatine layer is not confined and it is the drainage perimeter.

In parallel with the fracture experiment, the bottle for measuring the gas production rate, γ, was held at the same temperature as the Hele-Shaw cell. In the Exp_1 and Exp_2 the gas production rate increased steadily from zero, after ≈ 2 h the production rate had reached ≈ 0.7 ml/h and at 20 h it peaked at ≈ 2 ml/h.

Dynamics of fracture nucleation and growth. The first tiny bubble appeared in the gel after about 2 hours from the beginning of the experiment and 10-20 bubbles nucleated during the next 20 hours. Bubbles grew until they reached a diameter of approximately $l_0 = 2.3 \pm 0.2$ mm and then changed into elongated cracks with sharp tips after 12 ± 3 min. However, for about 50% of the fractures, an initial bubble nucleation and growth stage was not observed with the image resolution used in these experiment (see movies in the Supplementary Material). Crack tips propagated with increasing velocity, at both ends of the fractures, unless they became blunted or closely approached the boundary of the gelatine layer or another crack. During the free propagation regime, before cracks started interacting with other cracks or with the boundary, the crack length evolved with time as:

$$l = l_0 \exp(t/\tau), \tag{1}$$

where t is the time since fracture nucleation. The increase in the timescale, τ with increasing gas production rate, γ, could be represented by $\tau = 0.54/\gamma - 0.20 \pm 0.017$ h. Each crack tip either propagated until it connected to another fracture or reached the gel boundary, or it slowed down and eventually halted inside the gel matrix, forming a dead end. When a fracture was not connected to other fractures or the gel boundary, its aperture a increased with time due to increasing gas pressure until a maximum aperture of approximately 3 mm was reached

along most of the fracture length. When two cracks intersected their apertures changed rapidly indicating pressure equilibration. When a crack reached the gel boundary, its aperture collapsed as the gas drained from the system in less than one second. Once a crack formed, it continued to serve as an intermittent drainage pathway that closed and opened. New fractures nucleated and propagated until a steady state fracture pattern stabilized, see Fig. 1A.

To analyze the development of the fracture pattern, the images of fractured gelatine were processed such that all pixels that were once covered by a fracture were preserved in accumulated images that represent the development of the fracture network. The final accumulated fracture pattern for experiment Exp_1 is displayed in Fig. 1B).

In most cases, both crack tips propagated linearly, with about the same velocity, until they reached a distance of $\lambda_e = 10\pm5$ mm from another crack or a distance of 20 ± 5 mm from the gel edge. In such instances they would slow down, speed-up, or change direction, depending on the circumstances. We will refer to λ_e as the elastic interaction length.

Using digital image correlation [17], the motion of tracer particles in the gel and of the gel edges was tracked. When cracks open, new volume is generated in the system, but no systematic expansion of the gel in the plane of the Hele-Shaw cell was found. However, by using an LVDT displacement sensor (Omega Engineering), we found that the glass plates confining the gel moved in the direction perpendicular to the plane of the Hele-Shaw cell plane, allowing the gel to increase in thickness. The total deflection of the plates corresponded to a total volume increase of $(1.9 \pm 0.1) \times 10^{-6}$ m^3. Since the gel is essentially incompressible, this corresponds to the volume of the gas trapped in the fractures and the largest total volume of the open fractures was estimated from image analysis to be $(2.2 \pm 0.1) \times 10^{-6}$ m^3.

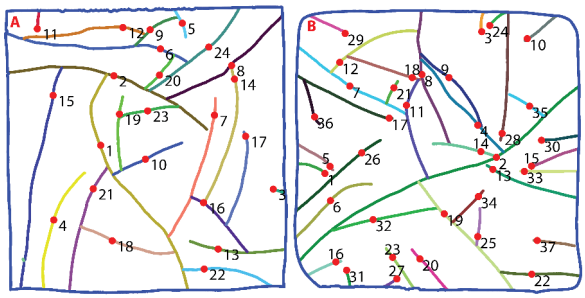

Fig. 2: **A, B:** Nucleation sites and fracture labeling in Exp_1 (A) and Exp_2 (B). The fractures are distinguished by their colours and their numbers indicate the order in which they appeared. The red circles mark the nucleation sites.

Spatial distribution of fracture nucleation. To characterize the mechanisms of crack formation and growth we analyzed to what degree new fractures nucleate either in the middle of unfractured domains, near existing fractures, or randomly. When a crack formed it was assigned a number indicating the order in which it was formed as shown for experiments Exp_1 and Exp_2 in Fig. 2 A and B. Distance maps as shown in Fig. 3 were computed where the colour indicates the distance $r(x, y)$ from the coordinate (x, y) to the closest fracture or free boundary. For each nucleation event i, the distance r_i, position, (x_i, y_i) and gradient $\nabla r(x_i, y_i)$ were determined just before nucleation occurred. On a line through (x_i, y_i) in the direction $\nabla r(x_i, y_i)$, the local maximum of r is denoted $r_{max,i}$. The normalized distance $r_i/r_{max,i}$ =0 or 1 correspond to nucleation at an existing fracture or in the middle of an unfractured domain. The cumulative distribution $N(r/r_{max} > r_i/r_{max,i})$, which is plotted in Fig. 4, characterizes the degree of randomness in the locations of the nucleation sites and is fitted by $N = (r_i/r_{max,i})^{\mu}$, $\mu = 1.94$. $\mu \leq 1$ (the exact value depends on the shape of the unfractured area) corresponds to completely random nucleation and $\mu \to \infty$ corresponds to deterministic nucleation in the middle of an unfractured domain. The inset shows the cumulative distribution of r_i and demonstrates that there is a minimum distance between nucleation sites and preexisting fractures.

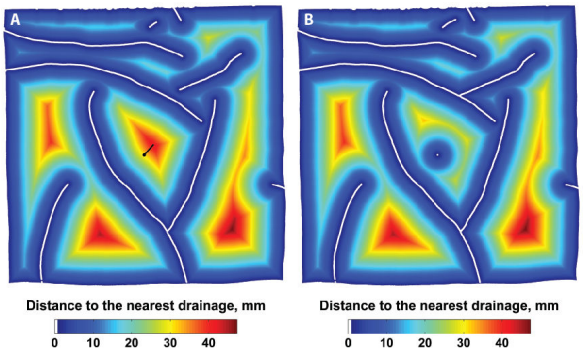

Fig. 3: Map of distance, $r(x, y)$ to the nearest fracture right before and after the nucleation of fracture 10 in Fig.2A. **A:** A line from (x_{10}, y_{10}) in the direction $\nabla r(x_{10}, y_{10})$ up to the position of the local maximum of r, $r_{max,10}$ is drawn in black. **B:** Shows how the distance map is changed immediately following the nucleation of fracture 10.

Fracture growth direction. The direction of fracture propagation from the nucleation point was measured and it was found that the distribution of angles between the fracture directions and the distance gradients, $\nabla r(x_i, y_i)$, was uniform between 0 and 90 degrees.

Analysis of steady state fracture pattern. The steady state fracture network shown in Fig. 1B was skeletonized and all intersections of fractures (blue circles in Fig. 5A) and fracture tips (red squares in Fig. 5A) were identified and labeled as *nodes*. A fracture may be divided into *segments* consisting of the part of the fracture between two adjacent nodes or between a node and an end of the fracture and these segments are identified by different colours

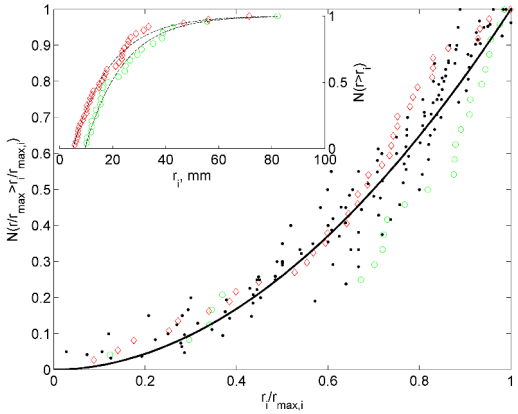

Fig. 4: Cumulative distribution of the normalized distances, $r_i/r_{max,i}$, from nucleation sites to the nearest drainage interface. Green data points correspond to Exp_1, red to Exp_2. The black dots correspond to randomly generated networks using the fragmentation fracture model. The continuous line is a fit of the data using the function $y = x^{\mu}, \mu = 1.94$. The inset shows the cumulative distributions of r_i. This indicates that there is a minimum distance between nucleation points and preexisting fractures, r_{min} of about 5 and 10 mm in the 2 experiments.

in Fig. 5A, (the outer boundary is considered to be one continuous segment).

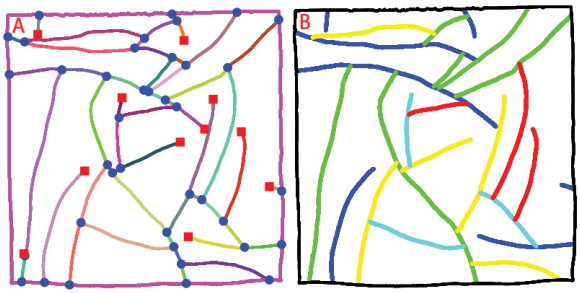

Fig. 5: Characteristics of the fracture network of Exp_1. **A:** Fracture segments labeled with different colours. Blue discs indicate junctions between segments and red squares indicate dead ends. **B:** Fracture network coloured according to the fracture generation number, n_C, of fracture C intersecting fractures A and B: $n_C = \max(n_A, n_B) + 1$, Black: 0, Blue: 1, Green: 2, Yellow: 3, Light blue: 4, Red: 5

At each node we measured the angles between intersecting segments. There were two distinct peaks: one in the range $180 \pm 5°$ and the other in the range $90 \pm 10°$. By joining segments that intersect at angles about 180°, we reconstructed the continuous fractures which formed by propagation from a single nucleation point. This fracture pattern has a temporal order of nucleation (see numbering in Fig. 2). In addition a hierarchical order can be defined such that if fracture C ends at fractures A and B its generation number is $n_C = \max(n_A, n_B) + 1$, where n_A and n_B are the generation numbers of fractures A and B [6]. The draining perimeter is considered to be generation 0. In the experiments, up to five fracture generations ($n = 5$) were measured. In Figure 5 B, the fractures of Exp_1 have been colour coded to indicate their fracture generation numbers. A fracture is "younger" than the youngest fracture it forms a junction with. One possible alternative generation numbering scheme emphasizing the drainage aspect of the network would be $n'_C = \min(n'_A, n'_B) + 1$, which corresponds to numbering of river segments in a drainage basin. Using this scheme the highest drainage generation is $n' = 3$.

Discussion and conclusion. – The experimental results were used to propose a mechanism of fracture nucleation and propagation. We now demonstrate that the fracture network has intermediate statistical properties between those of river-like and hierarchical fracture-like patterns.

A diffusion-nucleation model for fracturing. The production of CO_2 provides the energy required for fracturing the gel and the fracture network evolution depends on the coupling between CO_2 transport and elastic interactions in the matrix. The observation that fractures initiate as bubbles far away from existing boundaries suggest that crack nucleation is not determined by elastic interactions. We therefore propose the following diffusion-nucleation model:

1. Most of the generated CO_2 is dissolved into the gel, which consists of 95% water. The solubility and diffusion coefficient of CO_2 in the gel are approximately the same as in pure water, $c_0 = 1.8$ g/l and $D = 1.85 \cdot 10^{-9}$ m^{2}s^{-1} [18]. The dissolved CO_2 has negligible mechanical effects on the gel matrix.

2. Bubbles nucleate when CO_2 generation leads to local supersaturation in the gel. Nucleation is heterogeneous and only a small supersaturation is required.

3. As bubbles grow they begin interacting elastically with the gel matrix and a transition from bubbles to fractures occurs.

4. The subsequent fracture propagation is driven by the gas pressure on the fracture walls which induces elastic stresses in the material.

Growth of a single fracture. After a fracture has nucleated it propagates when the gas pressure exceeds some critical value p_c. When fractures propagate slowly the gas pressure is constant and equal to p_c. Using the ideal gas approximation $p_c = \frac{n_{CO_2} RT}{V}$ =const., the change in fracture volume is

$$\frac{dV}{dt} = \frac{RT}{p_c} \frac{dn_{CO_2}}{dt}. \qquad (2)$$

The fracture aperture is limited to $a = 3$ mm due to adhesion of the gel to the walls of the Hele-Shaw cell and the

volume of gas in the fracture is $V \approx lah$, where l is the fracture length and $h = 3$ mm is the distance between the glass plates. During propagation of a single fracture we assume a constant CO_2 flux, ϕ, over the fracture surfaces

$$\phi = \frac{dn_{CO_2}}{dt}\frac{1}{2lh} = const. \quad (3)$$

The expression

$$l = l_0 \exp(\frac{2\phi RTt}{p_c a}), \quad (4)$$

for the fracture length can be derived by combining equations (2) and (3) and integrating. Here, l_0 is the integration constant, which characterizes the critical length above which a gas bubble evolves into a fracture. This corresponds to equation (1), which was used to fit the experimental data and comparison of equations (1) and (4) indicate that $1/\tau \propto \phi \propto \gamma$.

Size of unfractured domains. Various factors control the final configuration of the fracture network. Since the gas production rate is virtually constant for a long period after the last fracture has stopped propagating we assume that the system reaches a quasi steady state in which the fracture network drains the gel matrix sufficiently to hinder further fracturing. Using a diffusion-nucleation model, the characteristic size of unfractured domains, for which loss of CO_2 by diffusion is sufficient to prevent nucleation of new fractures can be estimated.

Consider a gel segment bounded by two parallel fractures separated by a distance 2δ. Assuming a constant CO_2 production rate, γ, the steady state equation for the concentration field in the gel is:

$$D\nabla^2 c + \gamma = 0. \quad (5)$$

We assume that the flux ϕ of CO_2 across a fracture surface is proportional to the difference between the concentration c of dissolved CO_2 at the surface and the concentration required for chemical equilibrium with the gas pressure $p = k_H c$ in the fracture, i.e.

$$\phi = D\frac{dc}{dx}|_{x=\pm\delta} = k(\frac{p}{k_H} - c(\pm\delta)), \quad (6)$$

where k_H is the Henry's coefficient and k is a rate constant of CO_2 evaporation from the gel. The solution of (5) is:

$$c(x) = \frac{p}{k_H} + \frac{\gamma\delta}{k} + \frac{\gamma}{2D}(\delta^2 - x^2). \quad (7)$$

We assume that to nucleate a bubble a critical supersaturation $c_c = p_c/k_H$ is needed. Inserting $c(x = 0) = c_c$ into equation (7) we may solve for the critical distance δ_c and find two scaling regimes:

- Diffusion limited ($k \to \infty$), $\delta_c = \sqrt{\frac{2D}{\gamma}\frac{p_c - p}{k_H}} \propto \gamma^{-1/2}$
- Evaporation limited ($D \to \infty$), $\delta_c = \frac{k}{\gamma}\frac{p_c - p}{k_H} \propto \gamma^{-1}$

It follows that in the diffusion limited case $\gamma^{1/2}\delta_c$ should have a constant value and $\gamma\delta_c$ should have a constant value for the reaction limited (evaporation limited) case. In Exp_1 the mean production rate was $\gamma = 1.6$ ml/h and $2\delta_c = 22.2$ mm ($\gamma\delta = 17.76$, $\gamma^{1/2}\delta = 14.0$) and in Exp_4 the mean production rate was $\gamma = 6.2$ ml/h and $2\delta_c = 10.7$ mm ($\gamma\delta = 33.2$, $\gamma^{1/2}, \delta = 13.3$). This is consistent with the diffusion limited model, but not with the reaction limited model. The shape of the cumulative distribution function (for $r_i/r_{max,i}$) shown in Figure 4, with $\mu = 1.94$, is also consistent with the diffusion limited scenario, but not with the reaction limited model since in the reaction limited limit $\mu \leq 1$.

Elastic interactions, directed networks and loops. The short range of the elastic interactions is a consequence of the adhesion between the gel and the essentially rigid walls of the Hele-Shaw cell. A three dimensional solid full of gas filled fractures will also have a limited elastic interaction length due to the "screening" by open fractures. The elastic interaction between fractures in the model system results in the opening and closing of fracture apertures at junctions, which act as valves to the gas flow. This dynamic process, causing intermittent gas release, will be described in detail in a future communication. The adhesion between the gel and the glass walls of the Hele-Shaw cell also imposes an effective confinement on the system similar to the effects of compressive elastic stress on a three dimensional system. Under such confining conditions, neighbouring fractures in analogous three dimension systems will interact in a similar manner - when the aperture of one fracture increases due to increased fluid pressure it will increase the compressive stress on neighbouring fractures and this will reduce their apertures.

It should be noted that although $\delta_c \sim r_{min} \sim \lambda_e \sim 10mm$ in experiments Exp_1 and Exp_2, the similarity between λ_e and the other lengths is fortuitous. The elastic interaction length λ_e does not depend on the gas production rate as do δ_c and r_{min} and elasticity does not control δ_c and r_{min}.

The direction of gas flow follows the direction of the pressure gradient, but because confinement induces elastic interactions between fractures and nearby fractures and junctions, which may act as valves when the gas pressure is reduced, the direction of the pressure gradient is not static. Because of the "valve closing" effect, fractures that are connected at one end to a fracture network that reaches the edge of the gel may propagate at the other end until that end also contacts a preexisting fracture. The end result is a network with loops. A hierarchical fracture network [6, 7] is ideally fully connected.

Model of fracture propagation. A simple model that captures some of the essential features of our experimental system and incorporates river-like and hierarchical fracture-like networks as limiting cases was developed. A lattice model of size $L \times L$ was used, where L is the size of the gelatine layer. Fractures nucleate and propagate

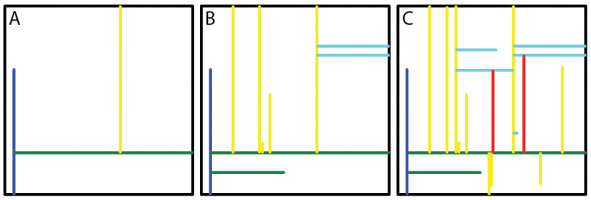

Fig. 6: Fragmentation fracture model with $\omega = 0.36$ shown at three stages of evolution, $l_t/L = 2.2, 5.1, 8.56$. The lines are coloured according to the fracture generation number, n_C, of fracture C intersecting fractures A and B: $n_C = \max(n_A, n_B) + 1$, Black: 0, Blue: 1, Green: 2, Yellow: 3, Light blue: 4, Red: 5.

sequentially and form a "final" pattern when the system is completely drained, i.e. when the cumulative fracture length in the pattern exceeds or equals the cumulative fracture length l_t. l_t/L is 8.5 in Exp_1 and 8.7 in Exp_2. The nucleation sites are chosen according to a probability distribution $P(x, y)$ that depends on the distance from the site to the nearest fracture or boundary. We chose a power law distribution such that the probability of nucleating a fracture at site (x, y) is:

$$P(x, y) = r(x, y)^{\mu-1} / \sum_{x,y} r(x, y)^{\mu-1}, \qquad (8)$$

where $r(x, y)$ is the distance from the nearest fracture or the boundary. This choice is justified by the experimental distribution (Figure 4), where the power law exponent was determined to be $\mu = 1.94 \pm 0.06$. The black dots in Figure 4 show the resulting cumulative distribution of $r_i/r_{max,i}$ of nucleation points for 20 realizations of the model. This demonstrates that although the model was constructed with a different metric from that used to measure μ an exponent of $\mu = 1.94$ makes the model nucleation distribution lie within the range of uncertainty of the experimental nucleation distribution.

Once a nucleation site is selected, the fracture orientation is randomly selected as horizontal or vertical. The fracture propagates by the same distance in both directions until it reaches and forms a junction with another fracture or the system boundary. At this instance the fracture may either cease to grow because it is drained by the joining fracture (with probability 1-ω), or it may continue to grow until the other end meets an existing fracture (with probability ω). $\omega = 1$ corresponds to all fractures connected at both ends which is typical of a hierarchical fracture pattern [6]. $\omega = 0$ corresponds to all fractures connected at one end only which is typical of river networks. The probability ω of a network can be deduced from the ratio between the number of dead ends, n_d, and the number of junctions, n_j: $\frac{n_d}{n_j} = \frac{1-\omega}{1+\omega}$ and ω are 0.41 and 0.32 for Exp_1 and Exp_2.

Conclusion. The generation and exsolution of CO_2 in a gel filled Hele-Shaw cell generated a new type of drainage fracture network with topological properties intermediate between those of directed river networks and hierarchical fracture networks. The valve-like opening and closing of fracture apertures at fracture junctions plays an important role in the formation of this type of fracture network. Diffusion of CO_2 in the gel inhibits the nucleation of new fractures in the vicinity of preexisting fractures and a simple random nucleation model that takes this and the probability that fracture propagation stops before both ends of the growing fracture reach other fractures, reproduces key characteristics of the experimental fracture network.

* * *

We acknowledge support by the Petromaks program of the Norwegian Research Council. This study was supported by a Center of Excellence grant from the Norwegian Research Council to the Physics of Geological Processes Center (PGP).

REFERENCES

[1] Banavar J. R., Maritan A. and Rinaldo A., *Nature* , **399** (1999) 130.
[2] Dodds P. S. and Rothman D. H., *Physical Review E* , **63** (2001) .
[3] Rinaldo A., Banavar J. R. and Maritan A., *Water Resources Research* , **42** (2006) .
[4] Zaliapin I., Foufoula-Georgiou E. and Ghil M., *Journal of Geophysical Research-Earth Surface* , **115** (2010) .
[5] Goehring L. and Morris S., *Europhysics Letters* , **69** (2005) 739.
[6] Bohn S., Douady S. and Couder Y., *Physical Review Letters* , **94** (2005) .
[7] Cohen Y., Mathiesen J. and Procaccia I., *Physical Review E* , **79** (2009) .
[8] Sibson R. H., *Journal of Structural Geology* , **18** (1996) 1031.
[9] Davies J. H., *Nature* , **398** (1999) 142.
[10] Miller S. A., *Journal of Geophysical Research-Solid Earth* , **107** (2002) .
[11] Horton R. E., *Geological Society of America Bulletin* , **56** (1945) 275.
[12] Alava M. J., Nukalaz P. K. V. V. and Zapperi S., *Advances in Physics* , **55** (2006) 349.
[13] Andresen C. A., Hansen A., Le Goc R., Davy P. and Hope S. M., *arXiv:1203.4510* , (2012) .
[14] McKenzie D., *Earth and Planetary Science Letters* , **74** (1985) 81.
[15] Ozkaya I., *Marine and Petroleum Geology* , **5** (1988) 293.
[16] Di Giuseppe E., Funiciello F., Corbi F., Ranalli G. and Mojoli G., *Tectonophysics* , **473** (2009) 391.
[17] Hild F. and Roux S., *Strain* , **42** (2006) 69.
[18] Li H. L., Wilhelmsen O., Lv Y. X., Wang W. L. and Yan J. Y., *International Journal of Greenhouse Gas Control* , **5** (2011) 1119.

Paper 4

Temporal evolution of a drainage fracture network in an elastic medium with internal fluid generation

Maya Kobchenko[1], Andreas Hafver[1], Espen Jettestuen[1], Olivier Galland[1], François Renard[1,2], Paul Meakin[1,3], Bjørn Jamtveit[1] and Dag K. Dysthe[1]

[1]Physics of Geological Processes, University of Oslo, Norway;
[2]Univ. Joseph Fourier, ISTerre, BP 53, F-38041 Grenoble;
[3]Temple University, Department of Physics, Barton Hall, Philadelphia, PA 19122-6082

In preparation. Will be submitted to Physical Review E.

Temporal evolution of a drainage fracture network in an elastic medium with internal fluid generation

Maya Kobchenko, Andreas Hafver, Espen Jettestuen, François Renard,
Olivier Galland, Bjørn Jamtveit, Paul Meakin, and Dag Kristian Dysthe
Physics of Geological Processes, University of Oslo, Norway and
Univ. Grenoble Alpes, ISTerre, BP 53, F-38041, Grenoble, France
(Dated: May 30, 2013)

Escape of internally generated fluids from low permeability elastic solids plays an important role in several natural environments. In geological systems, primary migration of hydrocarbons, dehydration of sediments and hydrated mantle rocks in subduction zones are examples where the existing permeability cannot accommodate transport of generated fluids in low permeability rocks and fluid pressure build-up may alter the permeability by fracturing. Fractures form and propagate in the rock due to internal pressure build-up. We develop a simple and reproducible analog experiment to simulate fracture formation in a low permeability elastic solid during internal fluid/gas production in a Hele-Shaw cell. The present study aims to describe the physical mechanism of fracture network growth and the temporal evolution of the created fractures. The nucleation, propagation and coalescence of fractures within the solid matrix occurs due to CO_2 production by yeast consuming sugar, and is monitored by optical means. We first quantify how an equilibrium fracture network develop, and then how the intermittent fluid transport is controlled by the dynamics of opening and closing of fractures. Three characteristic features of the gas escape dynamics are evidenced. 1) A periodic release of gas due to the Hele-Shaw cell confinement, where the characteristic frequency is independent of system size and depends on gas production rate. 2) An intermediate range of $1/f$ dependence of fracture opening fluctuations, that is argued to be due to collective effects in the drainage network. 3) A $1/f^2$ dependence of the power spectrum at high frequencies, that can be explained by a single fracture cellular-automaton model.

I. INTRODUCTION

Natural fracture networks in the rocks of the Earth's crust develop either when an external stress is applied at the boundaries of a system, or when such stress builds up inside the system. Natural hydraulic fractures form inside a rock matrix due to the internal fluid pressure build-up [1]. Fluid pressure build-up may have various origins: compaction of the rock matrix in sedimentary basins may trap overpressured reservoirs [2]; compaction of gouge in fault zones [3]; magma emplacement and rapid heating of either water (phreatic explosions) or organic-rich rocks [4]; or partial melting of minerals [5]. The internal fluid pressure can also be generated by chemical reactions which produces fluid in a tight rock matrix. An example is the reaction-induced fracturing of low-permeability rocks during hydrocarbon generation in organic-rich shales during diagenesis [2]. In these systems, the fracture network develops in response to internal pressure generation and the resulting crack pattern is therefore the consequence of energy dissipation at various scales in the rock body. In the present study, our goal is to better understand the spatio-temporal coupling between elastic matrix deformation, fracture generation and fluid transport.

Visualizing the coupling between fluid pressure build-up and fracturing processes is important. X-ray microtomography techniques can be used to analyze the three-dimensional morphology of fractures produced experimentally in rocks [6, 7]. Combinations of various thermodynamic conditions (temperature, pressure) with in-situ X-ray imaging is also under development, for example imaging of microcracks forming during heating of shales [8], investigation of dehydration processes in gypsum during heating [9] or the generation of magmatic melt in oceanic olivine-rich rocks [10]. In such studies, obtaining a good time and spatial resolution, at the thermodynamic conditions where the process occurs, is technically challenging and few data can be collected. Moreover, the micro-tomography technique does not allow, yet, ultrafast acquisitions for geomaterials because of their high absorption of X-rays. Other experimental techniques where time and spatial resolutions allow following the processes of fracturing at high resolution are therefore complementary to such in-situ studies.

To study fracture formation processes, experiments using materials analog to rocks, such as elastic gels, plasticine or sand, are widely used [11, 12]. Among such analog systems, the accumulation and transport of fluid in gelatin as well as hydro-fracture propagation was studied [13–15]. In all but one study, the source of the fluid was a single point. Bons and van Milligen [11] simulated homogeneous gas production by using CO_2 produced by yeast consuming sugar. In this experiment, sand was used as a host matrix, which deforms brittly when fractures form, but exhibits grain flow behavior when fractures are reactivated after healing. This system was designed to model transport of melt within rock. They presented the power spectrum of the volume of escaping gas $|Y(f)^2|$ as function of time frequency f. The existence of a signal with $1/f$ statistics in the low frequency range and $1/f^2$ statistics in the high frequency range was observed. The rescaled range analysis showed a Hurst exponent $H = 0.9$. The system was argued to be self-organized critical and have memory. Dahm [14]

observed the buoyancy driven propagation of hydrofractures that open at one end and close at the other end, providing pathways for moving fluid. The discrete character of fluid transport in time and space was also recognized [11], as observed in natural calcite veins that show crack-seal patterns with several generations of fracture opening [16]. But the intermittency of this process of fracture closing and opening was not studied in-situ. In low permeability rocks, the opening, closing and healing of fractures may be the dominant fluid transport mechanism during compaction and fluid expulsion. In some systems, phenomena such as episodic fluid expulsion [17] and porosity waves [18] are controlled by these processes.

In the present study, we introduce a laboratory experiment where we model homogeneous gas production inside a thin gelatin elastic layer, a model system for brittle rocks. We monitor 2D in-situ fracture nucleation, growth and coalescence until the formation of a fracture network occupies the entire system. When time passes, the internally produced gas escapes from the fractures which become partially healed. When the gas pressure rises again, the same fractures are reactivated and serve as pathways for intermittent gas discharge. We quantify the dynamics of fractures opening, closing and interacting with neighboring fractures using optical imaging. Our main objective is to characterize how fractures initiate, grow, and coalesce, and how the flow of produced gas is drained out of the system.

II. MATERIALS AND METHODS

II.1. Experimental set-up

We study experimentally the accumulation, segregation, and escape of fluid from an impermeable solid, representing a model system of fracturing of organic-rich shales during hydrocarbon production [8]. A quasi two-dimensional elastic gelatin layer simulates an almost impermeable shale rock. Gas production is initiated by baking yeast consuming sugar (sucrose) in the bulk of gelatin matrix and producing CO_2. Transparency of gelatin allows good optical imaging and monitoring of fracture formation during CO_2 production. Although the gelatin medium does not reproduce the full complexity of the shale matrix properties, it reproduces several basic features of the fracturing process. The experimental set-up includes a Hele-Shaw cell made of two 1 cm thick glass plates clamped together and separated 3 mm apart (Figure 1A), a white light source, and photo- and video- cameras (AF-S Nikkor 18-70mm, and DX lens on Nikon D300). The preparation protocol consists of cleaning the inner surfaces of the Hele-Shaw cell before filling it with an aqueous gelatin gel (cross-linked collagenous polymers) to ensure maximum hydro-filling effect and sticking of gelatin to the glass. A rubber band was placed between two glass plates for sealing purposes while the gel was solidifying. The rubber sealing band was removed before the beginning of experiments.

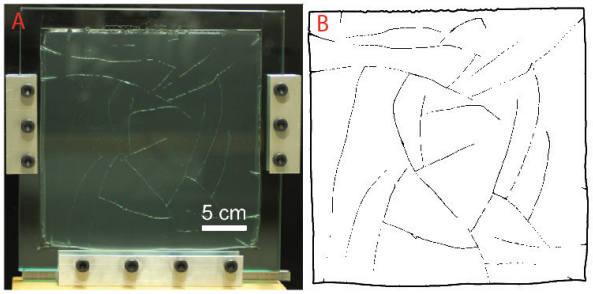

FIG. 1. **A:** The Hele-Shaw cell consists of two glass plates, 10 mm thick, separated 3 mm apart and filled with a layer of gelatin. The boundaries in lateral directions are free of confinement and the generated gas can escape only through them. The Hele-Shaw cell stands vertically. Back light was used to illuminate the fracture pattern. **B:** Thresholded image of the fracture pattern of the experiment D.

II.2. Materials

Gelatin dry sheets (from Gelita) were soaked into water ($20°C$) for 5-7 minutes and then mixed with hot water ($100°C$) until complete dissolution. The same gelatin concentration was used in all experiments: 58 g of gelatin sheets per total 1 dm^3 volume of water. Sugar was added to the hot gelatin mixture and dissolved. The gelatin and sugar mixture was then cooled down to $30°C$, and mixed with fresh baking yeast to ensure homogeneous solution. The liquid gelatin-yeast mixture was poured into the Hele-Shaw cell, and kept in refrigerator ($6°C$) for two hours in vertical position until the gel solidifies. When gelatin becomes solid, the Hele-Shaw cell was placed in horizontal position and kept for 10 hours in the refrigerator in order to obtain a homogeneous elastic gelatin solid matrix.

II.3. Experimental protocol

We conducted the experiments at 17°C, where the gelatin is transparent, brittle and nearly elastic. The rheological properties of gelatins have been studied in detail [19] and some applications of this material as rock analog was also proposed [12]. Inversion and fermentation of the dissolved sugar by yeast enzymes produces CO_2. For each experiment, half of the gel was poured into a bottle, for measuring the gas production rate using a simple volumometer system. In all experiments, the gas production rate increased steadily from zero, reached a maximum after several hours and then decreased; average production rates are given in Table II.

Initially, the CO_2 dissolves in the aqueous fluid that pervades the gel, but when the concentration of dissolved CO_2 becomes large enough, CO_2 bubbles nucleate and evolve into gas filled fractures. Fractures form by breakage of the cross-linked polymer structure forming the gel and the subsequent elastic deformation of the matrix. As

gas is produced the fractures propagate until they reach an open boundary or another fracture. When a pathway connecting a CO_2 filled fracture aperture to the edge of the Hele-Shaw cell via a fracture network is formed, the gas is transported along the fracture network, down a pressure gradient, to the edges of the gel layer, while the pathway remains open. Gas can escape everywhere along the perimeter of the gelatin layer (Figure 1A). Six

TABLE I. List of experiments and conditions. The yeast and sugar concentrations are given in Table II. Δt is the time resolution of the images.

Exp.	System size	Yeast+sugar	Δt	Duration
A	320x320 mm	x1	60 sec	16 h 21 min
B	250x250 mm	x1	15 and 60 sec	14 h 53 min
			video 15 fps	6 h 55 min
C	120x120 mm	x1	60 sec	29 h 25 min
D	250x250 mm	x1	60 sec	72 h 26 min
E	250x250 mm	x2	15 sec	36 h 16 min
F	250x250 mm	x1/2	15 sec	92 h 55 min

experiments under different conditions were conducted (see summary in Table I). Two main parameters were varied: system size (the lateral dimensions of the gelatine layer in the Hele-Shaw cell) and the concentration of yeast and sugar. Three experiments with the system size 32x32cm, 25x25cm and 12x12cm were performed using the reference concentration of yeast and sugar, which corresponds to the values under x1 in Table II. We will further call these experiments A, B and C respectively (see Table I). The experiment D was performed at longer duration in order to investigate the effect of variation in gas production rate with time. The experiments E and F with double and half yeast mixture concentration (x2 and x1/2 in the Table II) were conducted in the 25x25cm size system with the imaging time resolution $\Delta t = 15$ seconds between snapshots. In the experiments A-E a fracture pattern was observed, in the experiment F the gas production was not sufficient to cause fracturing. The experiments B and D were performed under identical conditions, to test for reproducibility. Fracture nucleation and

TABLE II. Variation of gas production.

Concentration	x1/2	x1	x2
Amount of yeast, gr/dm^3	1.25	2.5	5
Amount of sugar, gr/dm^3	3.75	7.5	15
CO_2 production rate, ml/h	0.4	1.6	6.2

propagation was monitored with high resolution camera, at a resolution of $9-4$ pixels per mm, and a pixel size of $0.1-0.25$ mm, taking snapshots every $\Delta t = 15-60$ seconds. At the same time, in the experiment B, video was recorded at a rate of 15 frames per second, in order to resolve fast processes of fracture collapse and gas escape. The recording was stopped when no new fractures formed.

During fracturing experiments, a series of images were acquired. First a picture of unfractured gelatin was taken as a reference image. Then, snapshots were recorded continuously with a time interval Δt between the images. We subtracted the reference image from all subsequent images to correct for the background light. Then, we applied a mask on all the images to select the gelatin area as the region of interest. We used the same threshold value to convert the images into binary data (Figure1B). Zero values of pixels (white color) on the binary images correspond to unfractured gelatin matrix, pixels with a value equal to 1 (black color) correspond to fractured site. We also conducted additional experiments where we used cross-polarizers to image the elastic strain field at the fracture tips, as gelatin is a photoelastic material (Figure 2).

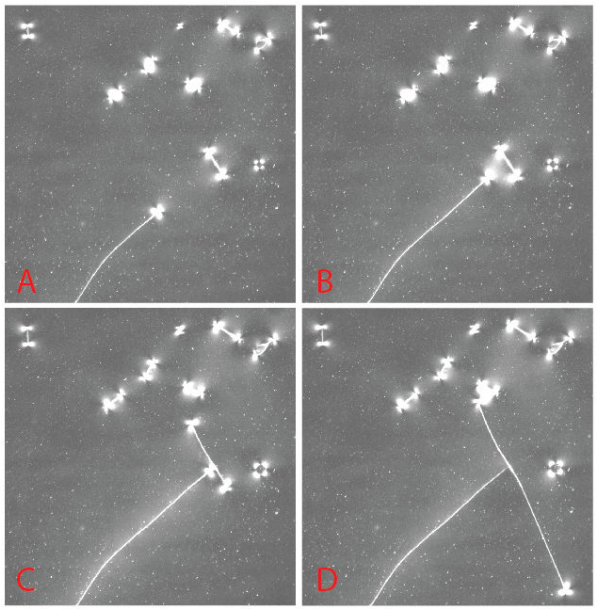

FIG. 2. Time-lapse strain field imaged using cross-polarizers. The photoelastic property of the gelatin allows the observation of elastic stress concentration at the fracture tips and interactions between fractures.

III. DEVELOPMENT OF A FRACTURE NETWORK

III.1. Nucleation and development of fractures

At the beginning of the experiment, yeast began to produce CO_2 homogeneously into the gelatin layer. As gas production increased, small volumes of gas accumulated randomly as bubbles. CO_2 diffused from the surrounding matrix to these bubbles, which led to local pressure increase. When the pressure exceeded the tensile strength of gelatin, bubbles evolved to cracks. The first fracture nucleates typically after $1-3$ hours after the start of the

experiment (Figure 3A). After nucleation, cracks begin to propagate (Figure 3B), while new cracks are formed.

With pressure increase, fractures grew in both directions until they reached a free boundary or another fracture. When a fracture reaches the open boundary, gas escaped from the fracture. When one fracture reaches another fracture, they coalesced and the strain field at the fracture tip disappeared (Figure 2). When gas escaped from a fracture, the pressure inside the fracture dropped down and the fracture walls collapsed. When a fractured collapsed, the fractured pixels disappeared from the image and the fracture is seen as a dashed line (Figure 3C). When the gas diffused into a closed fracture, it reopened, the fractured pixels reappeared and cracks could be seen as continuous lines again. The whole process of cracks opening and closing is highly intermittent, as characterized below. The gelatine layer is confined between two

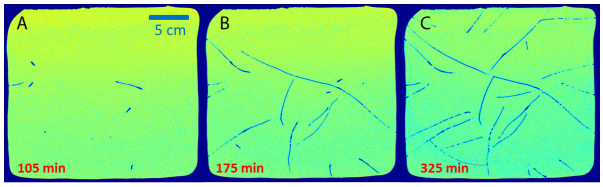

FIG. 3. Time-lapse images of fracture formation process in the experiment B. Dark pixels correspond to the fractured sites. **A**: As yeast produces CO_2, gas accumulates in bubbles, which nucleate randomly in the gelatin layer; then fractures start propagating. **B**: Fractures grow and propagate until coalescence. **C**: Coalesced fractures form an equilibrium network which provides pathways to the open boundary for outgoing CO_2 as fractures open and close intermittently through time.

glass plates with a gap of 3 mm. The adhesion of the gel to the glass surface causes resistance in the gel to the movement relative to the glass surface. When a fracture is formed in the gel, the fracture walls are perpendicular to the glass. In order to open the fracture, a pressure force needs to be applied on the fracture walls to overcome the elastic resistance. The higher the gas pressure in the fracture, the larger is the gap between fracture walls. The thickness of the fracture lines on the images represents the width of fracture openings and varies in the range from 0 to 3-5 pixels. The number of dark pixels in an image corresponds to the surface area created by open fractures. We will call this amount - *total fracture surface area*. Because fractures open and close with time, the variation of the total fracture surface area with time is a relevant measure of the dynamics of single fractures or of the whole network.

III.2. Fracture coalescence

In order to analyze the evolution of fracture networks without considering fractures collapsing and reopening, we need to identify the existing fractures from the moment they appear. As an input, we use the time series of binary images obtained after image analysis (Figure 3). We superimpose the binary images from the first up to the current time-step so that all pixels which fractured once remain fractured until the end of the experiment. In this way we obtain a series of images of continuously developing fracture network, whether fractures are open or closed (figure 4). These continuous fractures represent all the potential pathways for gas drainage. The amount

FIG. 4. The evolution of the fracture network for experiment D. Connected fractures are marked with the same color. **A:** New cracks nucleate. **B:** Fractures propagate and coalesce. **C:** Coalesced fractures form large connected pathway for outgoing gas.

of fractured pixels, which represent the fractured area, is constantly growing as experiment evolves because new fractured pixels are constantly added. Thus not only fracture length is increasing but also does the fracture thickness. In order to investigate how the fracturing network develops with time, we chose to consider the total fracture length as a more accurate measurement. We apply a skeletonization procedure to the overlapping images to reduce the fracture thickness to one pixel. In such way the amount of fractured pixels represents the total fracture length. Figure 5 shows the evolution of

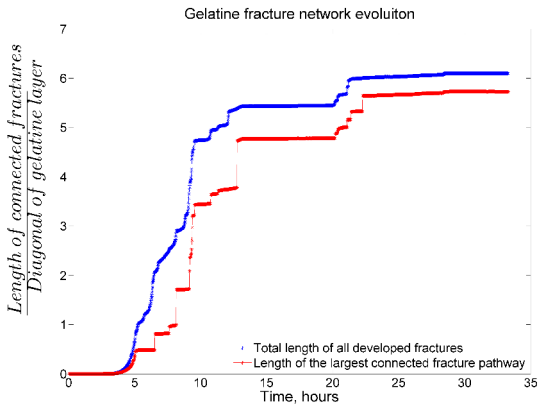

FIG. 5. Evolution of the connected fracture pathway in experiment D. **Blue curve:** Temporal evolution of the length of all connected fractures normalized by the diameter of the gel layer. **Red curve:** Temporal evolution of the largest connected fracture pathway. The abrupt stair-like increases on the curves correspond to fracture coalescence events.

the length of all accumulated fractures with time (blue curve), normalized by the diameter the gel layer. Three regimes of fracture growth can be distinguished. Firstly,

the initial nucleation of new fractures is characterized by slow growth in fracture length. Secondly, the nucleated fractures propagated and new ones appeared. Thirdly, at the end of the experiment when the system becomes saturated, the total fracture length remained constant.

We use overlapped binary images to extract and analyze connected fractures. We assign a label to every connected crack and we mark them with different colors (Figure 4). The analysis of the developed stationary fracture pattern is performed in another study [20]. Here we use the fracture labeling and information about fracture connectivity to analyze the spatial correlations of gas drainage dynamics.

As fractures propagate, they coalesce and form connected clusters (Figure 4C). Initially, the length of the largest connected fracture cluster evolves smoothly. When cracks start to coalesce, the length increases by discrete increments, producing jumps on the red curve in Figure 5. During the coalescence process, different clusters connect together until they form one dominant connected pathway, which covers almost the entire gelatin layer (blue pathway in Figure 4C). This dominant cluster drains the largest surface area and its evolution governs the drainage process of the whole system.

III.3. Evolution of the total fracture surface area

Figure 6 shows the time evolution of the total surface area of fractures in the gelatin layer in five distinct experiments (A-E). The amount of fracture pixels was normalized by the system surface area. Three regimes of fracturing can be distinguished. The first regime corresponds to fractures nucleation and propagation, when the total fractured area increases exponentially. The second regime corresponds to the stage when some fractures start to collapse while new cracks still appear and propagate. This regime is characterized by an overall increase in fracture surface area with superimposed oscillations. Finally, the third regime corresponds to an equilibrium fracture network, where no new fractures form. However, when fractures collapse and reopen again, the amount of fracture pixels fluctuates around a slowly varying value. The fluctuation amplitude and the time between fracture opening (surface area increase) and fracture closing (surface area decrease) depends on the rate of gas generation in the system as well as on system size. From the Figure 6 one can see that after about 2000 minutes, when the gas production decreases, the amplitude of the fracture surface area fluctuation in the experiment D decreases by the factor two. Experiment D also shows a slowly decreasing trend in the total fracture surface area for the same time interval.

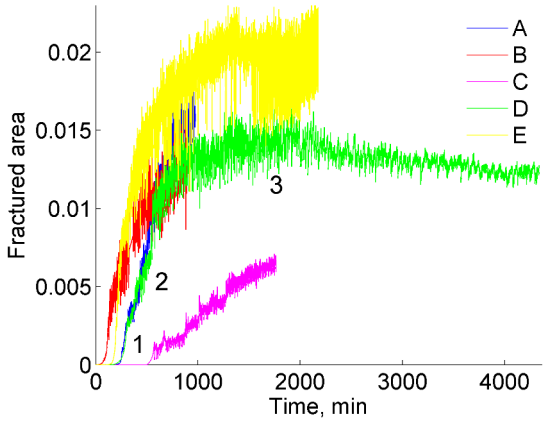

FIG. 6. Total fractured area fluctuation signal for five experiments. Three regimes of fracturing: 1 - fractures nucleate and grow; 2 - fractures collapse, new fractures appear; 3 - stationary regime, all fractures developed, they open and close.

IV. DYNAMICS IN THE FRACTURE PATTERN

IV.1. Temporal fluctuations of single fractures

In this section, we consider the dynamics of fractures that are not connected to other fractures (Figure 4). These isolated fractures originate in the gelatine layer and one of their tip connects to the open boundary. The amount of isolated fractures varies in different experiments. In the experiment C almost all fractures are isolated, because of the small size of the system. The inset of the Figure 7 shows the variation of the fractured area for one of the isolated fractures from the experiment C. A clear periodicity in the surface area fluctuations can be observed. The power spectrum of the signal is shown in Figure 7. One can see that the power spectrum features a well-pronounced peak around the frequency $f_c = 1.63 * 10^{-3}$ Hz, corresponding to a period of $\tau_c = 613$ seconds. Power spectra of opening/closing fluctuations were calculated for all isolated fractures in the experiments A,B, and C. These three experiments were conducted at the same gas production rate. The obtained power spectra were smoothed and the peak frequency f_c (as shown in the Figure 7) in the power spectra were determined. Figure 8 shows the distribution of the characteristic frequencies f_c. One can notice that the characteristic frequency does not depend on fracture length and is the same for all experiments $(1.97 \pm 0.64) * 10^{-3}$Hz. We suggest a simple model of periodic fracture opening and closing during homogeneous gas production. We consider an isolated crack which drains from one end to the open boundary. The amount of gas flowing into the fracture during time t is proportional to the drainage basin of the fracture $I \propto A$. The drainage basin area A is proportional to the fracture length l multiplied by typical basin width w: $A \propto l * w$. As we showed in [20], the typical basin width is constant for given gas production rate,

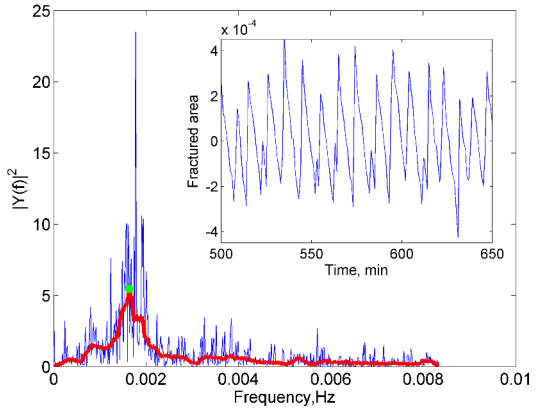

FIG. 7. Power spectrum of the fractured surface area fluctuation signal for one of the isolated cracks in the experiment C. Blue curve: original data. Red curve: filtered data. The peak frequency (green dot) is located at $1.63*10^{-3}$ Hz, which corresponds to a period of 613 sec. **Inset**: Variation of the fractured surface area for one isolated fracture in the experiment C. A low frequency trend was removed from the data.

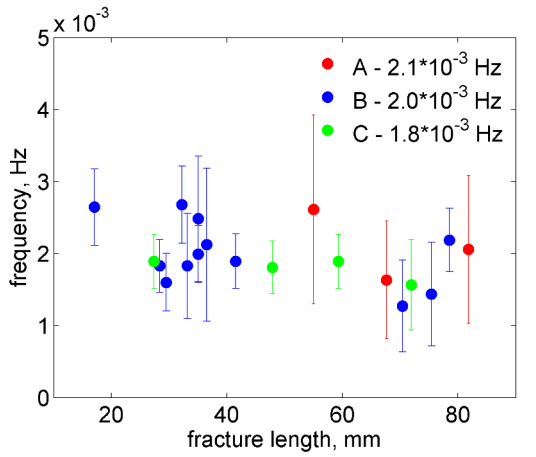

FIG. 8. Characteristic frequencies in the power spectra f_{ci} of fracture surface area of isolated fractures in the experiments A,B, and C versus length of the fractures l_i. The legend indicates the average characteristic frequency for each experiment. The characteristic frequencies do not depend on fracture length and vary in the range $f_c = (1.97 \pm 0.64) * 10^{-3}$Hz.

therefore $I \propto l$. The fracture capacity c is proportional to the fracture length l. The event of gas escape occurs when the amount of gas in the fracture exceeds the fracture capacity. From the relations $I \propto l$ and $c \propto l$ it follows that the time between two escape events (the period of fractured area fluctuations), τ, does not depend on fracture length but only on the rate of gas production into the system. The power spectra for 12 isolated fractures from experiment C were averaged (Figure 9). One observes a distinct peak at $f_c = 2 * 10^{-3} Hz$ and a rapid decay of all power spectra at higher frequencies,

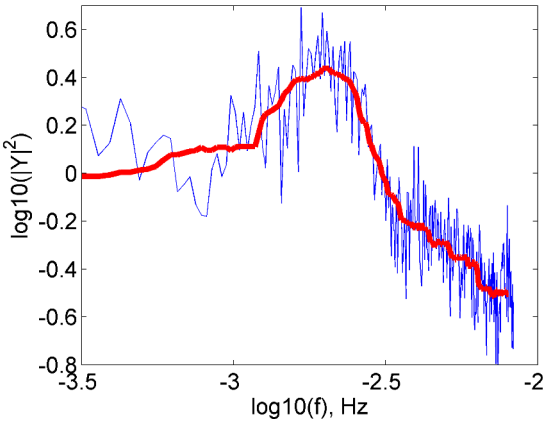

FIG. 9. Average power spectrum for 12 isolated fractures in the experiment B (blue curve) and filtered signal (red curve). The characteristic peak frequency is $f_c = 2 * 10^{-3} Hz$.

confirming of the presence of a characteristic frequency of fracture vibration, independent of their length.

IV.2. Temporal fluctuations of the total fracture surface area

Now we consider the variations of the total fracture surface area, without taking into account overall the period during which cracks grew. To do so, the total fracture surface area fluctuation signals (Figure 6) were analysed for all experiments as following. Firstly, a median filter with a window of 100 minutes was applied in order to extract the low frequency trend of the curve. Secondly, the filtered trend was subtracted from the original signal to display only the fracture surface area fluctuations, which occurred due to fracture opening and closing (Figure 10). On this curve, the growth in fracture surface area corresponds to the moment when gas flows into the fracture from surrounding gelatin and the fracture aperture and the amount of fractured pixels (fracture area) increases. When the gas escapes out of the fracture and fracture walls collapse, the amount of fracture pixels in the image decreases. The fluctuations of total fracture surface area features different amplitudes and frequencies. To analyse the frequency distribution, a Fast Fourier Transform algorithm (FFT) was applied. The fracture fluctuation signals for five experiments (Figure 6) were cut into intervals of equal duration containing $2^9 = 512$ data points. This length of the intervals was chosen in order to perform the FFT with maximum accuracy. Each interval was detrended and normalized by the standard deviation in order to remove low frequency components. The resolution of frequency distribution was $1/120Hz$ for the experiments with 1 minute time resolution, and $1/30Hz$ for the experiment with 15 seconds time resolution. The obtained power spectra were filtered with a median filter and averaged for all the inter-

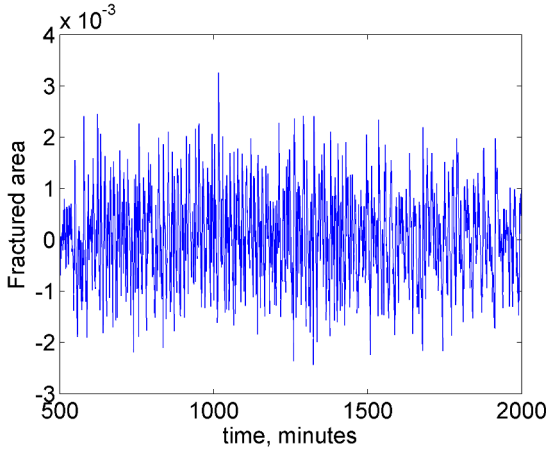

FIG. 10. Fracture surface area fluctuations after removing the low frequency trend between 500 and 2000 minutes in experiment D (see Figure 6.

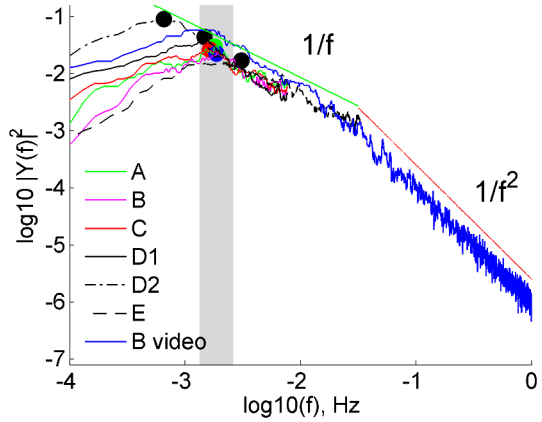

FIG. 11. Power spectra of the fracture surface area fluctuations for five different experiments.

vals in each experiment. The experiment D, which had the longest duration, was cut in two parts: $D1$ - from 500 minutes to 2000 minutes (the period of normal gas production) and $D2$ - from 2000 minutes until the end, when the gas production decreased. Figure 11 represents the smoothed frequency distribution curves. They are characterized by the high frequency slope, position of the peak and low frequency tail. One can see that the peak frequency is nearly the same for experiments A, B, C and D1, it varies in the range $(1.97 \pm 0.65) * 10^{-3}$ Hz. For the experiments D2 and E the peak is shifted in frequency. The reason is that experiments A, B, C and D1 were conducted with approximately the same gas production rate, whereas during experiments D2 and E the gas production rate was different. After normalization of the frequency curve by the peak value, the data collapse is shown in Figure 12. The power spectrum normalized by f_c and $|Y(f_c)|^2$ shows three distinct features: 1) A

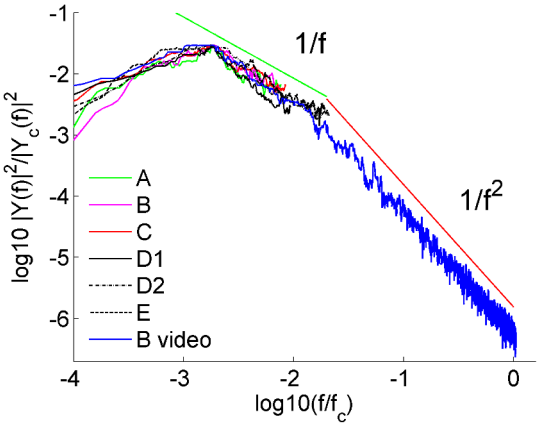

FIG. 12. Power spectra of fracture surface area fluctuations for five different experiments, normalized by critical frequency f_c and amplitude. All data collapse onto a single master curve.

periodic release of gas due to the Hele-Shaw cell confinement, where the characteristic frequency is independent of system size and depends on gas production rate; 2) a $1/f^2$ dependence of the power spectrum at high frequencies, that can be explained by a single fracture cellular-automaton model (see section V); and 3) an intermediate range with $1/f$ dependence, that is thought to be due to the collective effects of drainage on a connected fracture network.

IV.3. Hurst exponent

A rescaled range analysis is used to investigate the degree of self-similarity [21]. The original signal of total fractured surface area $a(t)$ fluctuation was detrended. The cumulative in time $A(t)$ of the original signal $a(t)$ was used to determine the range of variation R, calculated at different time intervals τ. S is the standard deviation of the original signal $a(t)$ taken at the same time interval. The quantity R/S plotted versus time lag in a bi-logarithmic scale falls on a straight line. The slope of this line is known as the Hurst exponent H. A random walk process has Hurst parameter $H = 0.5$. The rescaled range plots, measured for five fracturing experiments are presented in Figure 13. The mean value of the Hurst parameter for all five experiments is $H = 0.5$ for time periods $\tau_H > 100$ sec. For $\tau_H < 100$ sec the slope is 0.92, corresponding to a persistent behaviour. This τ_H behaviour corresponds to the high frequency domain of the power spectrum where $|Y(f)|^2 \propto 1/f^2$.

IV.4. Spatial correlations

We now investigate how different parts of the fracture pattern interact with each other. First, we consider dy-

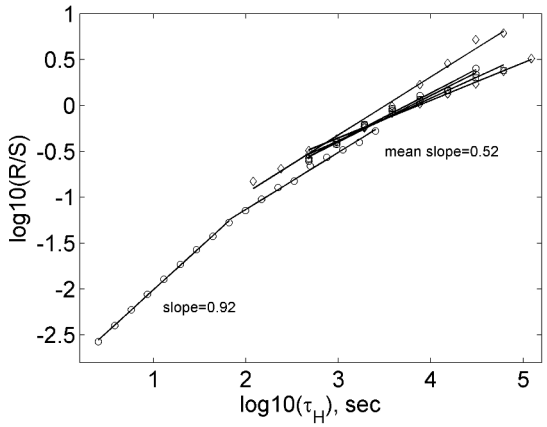

FIG. 13. Self-similarity analysis for five experiments, showing rescaled range (R/S, R - range, S - standard deviation) versus time lag.

namics of isolated fractures, the fractures which are not connected to other fractures but only drain to the open boundary. The fractures are located at some distance from each other, and this distance is larger than the distance of elastic interaction λ [20]. The signal of fractured surface area fluctuations for each isolated fracture has a characteristic period. The autocorrelation of fractured

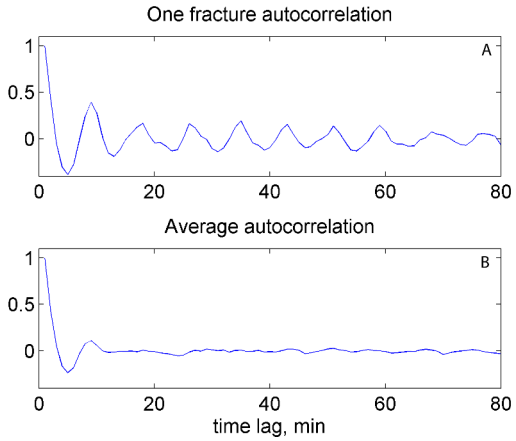

FIG. 14. Autocorrelation function for isolated fractures in the experiment B. Period equals 10 minutes. **A** An example of autocorrelation function for one fracture. **B** Average autocorrelation function. The fluctuation period is $\tau = 9$ minutes.

area signal for isolated fractures allows to determine fluctuation periodicity. The autocorrelation for one of the 12 fractures is presented in the Figure 14A. The fluctuation period is about 10 minutes. The average of all autocorrelation functions for 12 isolated fractures in the experiment B has a well-defined peak, which corresponds to the average characteristic period, $\tau \simeq 540$ seconds, for the area fluctuation of all isolated fractures in this experiment (Figure 14B). This confirms the peak frequency $f_c = 1.97 * 10^{-3} Hz$ observed in Figure 9 when performing a Fourier analysis.

In order to investigate how isolated fractures interact with each other, the cross-correlation between all possible pairs of 12 isolated fractures from the experiment B was calculated. Figure 15A,B shows two examples of cross-correlations between fluctuations of two isolated fractures. For both fracture pairs, the opening and closing oscillations are synchronized. Figure 15A) demonstrates an example of in-phase oscillations (the cross-correlation is positive during first time period). Figure 15B shows an example of two fractures which open and close out of phase. For both examples the average period between correlation peaks is 480 seconds, a periodicity similar as in the Figure 8. Because the surface area variations

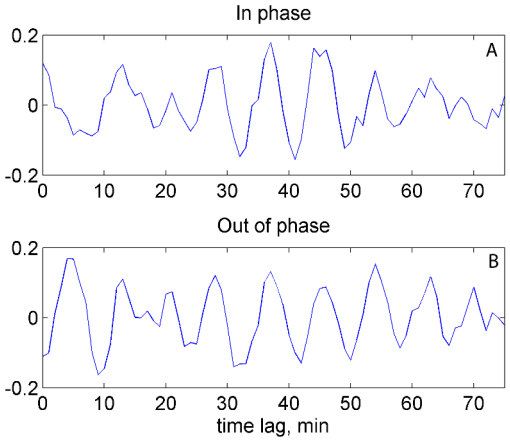

FIG. 15. Cross-correlation function for pairs of isolated fractures in the experiment B. **A** Fractured surface area of two fractures fluctuating in phase. The fluctuation period is $\tau = 480$ seconds. **B** Fracture surface area fluctuating are out of phase. The fluctuation period is $\tau = 480$ seconds.

for different isolated fractures have different initial phase shift, the average of cross-correlation function for all possible pairs does not exhibit any periodicity (Figure 16, green curve). The existence of a small peak (8% correlation) before a relaxation time lag of 1 minute may indicate that isolated fractures have some synchronization, noting however that this time is the resolution time of the experiment. This instantaneous correlation may be explained by the fact that all fractures are located in one layer of gel, which is placed between two glass plates. Because the gel is sticking well to the glass plates, the movement of the glass affects the dynamics of all fractures to a small degree. We now investigate the correlation of fractures that are connected to each other and form a drainage fracture network pattern. We consider fracture branches between intersection points (Figure 4). If two crack branches are connected in a junction point we call them neighbors and define the topological distance between them as $L_t = 1$. If two crack branches have one neighbor in between them, we say that these branches are located at the topological distance $L_t = 2$.

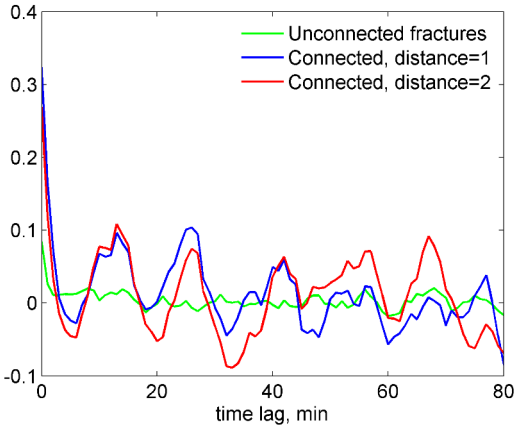

FIG. 16. Average cross-correlation for all possible pairs of fractures. **Green**: The average of cross-correlation functions for all possible pairs of isolated fractures in the experiment B. **Blue**: Average correlation of fracture branches at the topological distance $L_t = 1$ in the experiment D. **Red**: Average correlation of fracture branches at the topological distance $L_t = 2$ in the experiment D.

The fracture branches with topological distance $L_t = 1$ and $L_t = 2$ can communicate with each other through the junction points. This means that gas can flow from one fracture branch to another through the junctions.

We consider the cross-correlations of all possible pairs of fracture branches located at the topological distance $L_t = 1$, which is shown by the blue curve in the Figure 16, and branches located at the distance $L_t = 2$ - red curve in the Figure 16. The instantaneous correlation for close neighbors ($L_t = 1$) is larger (30%) than for the crack branches at the distance $L_t = 2$ - 25%. During evolution, opening and closing of neighboring fractures remain correlated for at least ten periods.

V. SIMPLE MODEL FOR INTERMITTENT FLUID EXPULSION

The $1/f$ spectrum observed in our experiments is typical for self-organized criticality (SOC) and could indicate that the gas expulsion from our system is a SOC process [22]. Bons and van Milligen [11] have already suggested SOC ballistic transport as a mechanism of primary migration, and they reported $1/f$ frequency spectra in experiments similar to ours. They also proposed a valve-network model, which they claim to reproduce their observations.

Inspired by Bons et al. [11], we seek a simple model that can reproduce our experimental observations. The first step in constructing such a model is to reduce our system of fractures to a network representation of links and nodes. In a coarse-grained version we take the junctions of the fracture network to be links and the fracture segments between junctions to be nodes. In a more fine-grained version we use the skeletonized image of a fracture system and represent nodes by the fracture pixels and links by pixel adjacency. Irrespective of the network discretization we consider the links to be valves that can open and close according to some set of rules. Fluid may be inserted either uniformly across the nodes or randomly at one node during each time increment. We used the

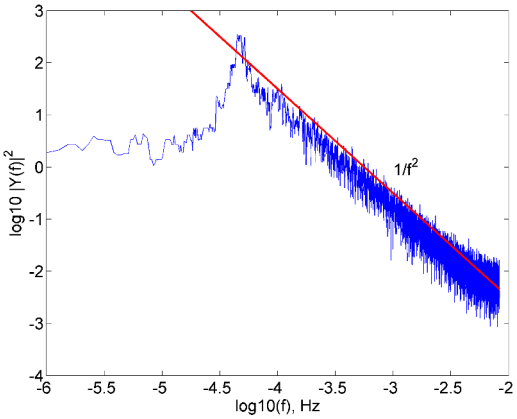

FIG. 17. Cellular-automata model of one single fracture. Peak indicates periodicity in the system. Power spectrum varies as $1/f^2$.

model of Bons et al. [11] on a single fracture. In agreement with their findings we obtain a $1/f$ frequency spectrum for the pressure variation at a single node. However, in our experiments we measured the area of open fractures, so a more relevant quantity to measure in the model is the total fluid content. Using the model of Bons and van Milligen we obtain fluctuations of the form $1/f^2$ (Figure 17). We are currently exploring alternative rules in an attempt to find a model that better represent our experiments.

VI. CONCLUSION

A simple and reproducible analog experiment was developed to simulate the drainage fracture pattern formed into a low permeability elastic solid during internal fluid production and subsequent escape. The fluid transport is controlled by intermittent dynamics of fracture opening and closing. A periodic dynamics of unconnected fractures was observed. The periodicity of gas release occurs due to the Hele-Shaw cell confinement, where the characteristic frequency is independent of system size and fracture length and depends on gas production rate. Cumulative dynamics of the drainage fracture pattern shows a $1/f^2$ dependence of the power spectrum at high frequencies, that can be explained by a single fracture cellular-automaton model, and $1/f$ dependence in the intermediate frequency range, that is argued to be due to collective effects in the drainage network. The analysis of spatial correlations in the fracture pattern shows the degree of

communication of fractures through fracture junctions that act as valves.

[1] E. G. Flekkoy, A. Malthe-Sorenssen, and B. Jamtveit, Journal of Geophysical Research-Solid Earth **107** (2002).

[2] K. Bjorlykke and P. Avseth, *Petroleum Geoscience: From Sedimentary Environments to Rock Physics* (Springer, 2010).

[3] F. Renard, J. P. Gratier, and B. Jamtveit, Journal of Structural Geology **22**, 1395 (2000).

[4] B. Jamtveit, H. Svensen, Y. Y. Podladchikov, and S. Planke, *Physical Geology of High-Level Magmatic Systems*, edited by C. Breitkreuz and N. Petford, Geological Society Special Publication, Vol. 234 (2004) pp. 233–241.

[5] J. A. D. Connolly, M. B. Holness, D. C. Rubie, and T. Rushmer, Geology **25**, 591 (1997).

[6] O. G. Duliu, Earth-Science Reviews **48**, 265 (1999).

[7] F. Renard, European Physical Journal-Applied Physics **60** (2012).

[8] M. Kobchenko, H. Panahi, F. Renard, D. K. Dysthe, A. Malthe-Sorenssen, A. Mazzini, J. Scheibert, B. Jamtveit, and P. Meakin, Journal of Geophysical Research-Solid Earth **116** (2011).

[9] F. Fusseis, C. Schrank, J. Liu, A. Karrech, S. Llana-Funez, X. Xiao, and K. Regenauer-Lieb, Solid Earth **3**, 71 (2012).

[10] W. L. Zhu, G. A. Gaetani, F. Fusseis, L. G. J. Montesi, and F. De Carlo, Science **332**, 88 (2011).

[11] P. D. Bons and B. P. van Milligen, Geology **29**, 919 (2001).

[12] E. Di Giuseppe, F. Funiciello, F. Corbi, G. Ranalli, and G. Mojoli, Tectonophysics **473**, 391 (2009).

[13] A. Takada, Journal of Geophysical Research-Solid Earth and Planets **95**, 8471 (1990).

[14] T. Dahm, Geophysical Journal International **142**, 181 (2000).

[15] J. L. Kavanagh, T. Menand, and R. S. J. Sparks, Earth and Planetary Science Letters **245**, 799 (2006).

[16] N. Rodrigues, P. R. Cobbold, H. Loseth, and G. Ruffet, Journal of the Geological Society **166**, 695 (2009).

[17] S. J. Roberts and J. A. Nunn, Marine and Petroleum Geology **12**, 195 (1995).

[18] J. A. D. Connolly and Y. Y. Podladchikov, Geodinamica Acta **11**, 55 (1998).

[19] G. M. Kavanagh and S. B. Ross-Murphy, Progress in Polymer Science **23** (1998).

[20] M. Kobchenko, A. Hafver, E. Jettestuen, O. Galland, F. Renard, B. Jamtveit, P. Meakin, and D. K. Dysthe, to be submitted to EPL (2013).

[21] B. A. Carreras, B. van Milligen, M. A. Pedrosa, R. Balbin, C. Hidalgo, D. E. Newman, E. Sanchez, M. Frances, I. Garcia-Cortes, J. Bleuel, M. Endler, S. Davies, and G. F. Matthews, Physical Review Letters **80**, 4438 (1998).

[22] P. Bak, C. Tang, and K. Wiesenfeld, Physical Review Letters **59**, 381 (1987).

Paper 5

Porosity evolution and crystallization-driven fragmentation during weathering of andesite

Bjørn Jamtveit[1], Maya Kobchenko[1], Håkon Austrheim[1], Anders Malthe-Sørenssen[1] Anja Røyne[1] and Henrik Svensen[1]

[1]Physics of Geological Processes, University of Oslo, Norway;

Publication data:
Journal of geophysical research, Vol. 116, B12204, doi:10.1029/2011JB008649, 2011.

Porosity evolution and crystallization-driven fragmentation during weathering of andesite

Bjørn Jamtveit,[1] Maya Kobchenko,[1] Håkon Austrheim,[1] Anders Malthe-Sørenssen,[1] Anja Røyne,[1] and Henrik Svensen[1]

Received 1 July 2011; revised 6 October 2011; accepted 7 October 2011; published 17 December 2011.

[1] A 10 m thick andesitic sill intrusion from the Neuquén Basin, Argentina, shows spectacular examples of spheroidal weathering and Liesegang banding. The Liesegang patterns demonstrate how andesite blocks, initially cut out by a preweathering joint set, are subdivided by fractures formed during the spheroidal weathering process. The stresses that cause fracturing originate from the growth of ferrihydrite and calcite in the pore space of the andesite, partly at the expense of original ilmenite, amphibole, and plagioclase. The porosity evolution and fracture formation during progressive weathering was characterized by scanning electron microscopy studies, X-ray computed tomography, and He- and Hg-porosimetry. Fresh andesite has a porosity of approximately 8%, and a major fraction (>80%) of the pore volume is composed of pores less than 10 μm in diameter. The extent of pore filling during weathering increases with pore size. Pores more than 100 μm are almost completely filled by an intimate intergrowth of calcite and ferrihydrite, whereas pores less than 10 μm are filled less than 50%. The fracturing associated with spheroidal weathering is caused by mineral growth in the largest pores, which account for 10%–20% of the total porosity. The periodic precipitation of the weathering product to form Liesegang bands indicates a significant supersaturation threshold before nucleation commences. The increase in the weathering product growth rate with increasing size is therefore most likely due to higher nucleation probabilities in larger pores.

Citation: Jamtveit, B., M. Kobchenko, H. Austrheim, A. Malthe-Sørenssen, A. Røyne, and H. Svensen (2011), Porosity evolution and crystallization-driven fragmentation during weathering of andesite, *J. Geophys. Res.*, *116*, B12204, doi:10.1029/2011JB008649.

1. Introduction

[2] The interface associated with the propagation of a weathering front into fresh rocks is of importance because it is the region where the biosphere interacts most strongly with the geosphere. It has recently become known as the base of the "Critical Zone" [cf. *Brantley et al.*, 2007]. The complex patterns and processes associated with the advancement of this interface, as well as the morphology of landforms and landscapes, are likely to be affected both by the heterogeneities in the unweathered bedrocks and by the weathering process itself. While some authors favor major controls by preexisting structures [*Twidale*, 2002; *Vidal Romani*, 2008], others emphasize pattern-forming instabilities arising during the weathering processes [*Strudley et al.*, 2006; *Chan et al.*, 2008].

[3] Spheroidal weathering is a well-known pattern formation process associated with weathering in a wide range of lithologies and climate zones. It has previously been interpreted as a process largely controlled by preexisting fractures, in which the role of weathering is mainly to round off the corners of blocks cut out by a network of fractures using an "onion-skin" spallation process to produce the observed "corestones" [*Ollier*, 1971; *Turner et al.*, 2003; *Fletcher et al.*, 2006]. However, recent studies of reaction-driven fracturing indicate that the weathering process itself may contribute to fracturing and division of corestones into smaller domains by corestone splitting [*Røyne et al.*, 2008; *Jamtveit et al.*, 2009]. Because of the continuous production of reactive surface area, this reaction-driven fracturing may significantly accelerate the weathering process.

[4] This article focuses on spheroidal weathering of an andesitic sill from the Neuquén Basin in Argentina. Because of the pronounced Liesegang banding of corestones separated by various generations of fractures, this andesite presents an unusually unambiguous record of corestone evolution and associated fracturing during spheroidal weathering. The weathering-driven fragmentation of preexisting andesite blocks can clearly be observed. The fresh andesite has a significant porosity (~8%), and the evolution of the pore structure during weathering reactions was characterized by scanning electron microscopy (SEM), X-ray

[1]Physics of Geological Processes, University of Oslo, Oslo, Norway.

0148-0227/11/2011JB008649

computed tomography (CT), and Hg-porosimetry. In contrast to previous studies, which suggest that fracturing during spheroidal weathering is caused mainly by volume-expanding reactions [*Fletcher et al.*, 2006; *Buss et al.*, 2008; *Røyne et al.*, 2008], this study emphasizes the influence of stresses generated by precipitation of weathering products in the largest pores of the original rock. The pore fluids become supersaturated with respect to carbonates and ferrihydrite during hydrolysis and oxidation of ferrous Fe released from the magmatic minerals. This supersaturation drives both the formation of Liesegang bands and the fracturing processes.

2. Geological Setting

[5] The Neuquén Basin is located on the eastern side of the Andes Mountains in Argentina and central Chile, between 32°S and 40°S. The basin comprises Late Triassic to early Cenozoic sequences covering an area of more than 120,000 km^2, with up to 6000 m of preserved marine and continental stratigraphy [e.g., *Gulisano and Gutiérrez Pleimling*, 1995; *Cobbold and Rossello*, 2003]. The sediments consist mainly of shale, sandstone, and carbonate, reflecting the varying depositional environments in the basin through time. The volcanic deposits formed during Andean subduction zone volcanism are also abundant. The weathering patterns in the andesitic to dacitic sill intrusion shown in this study were observed and sampled near Cuesta del Chihuido in southern Mendoza. Several sill intrusions outcrop in a road section along the RN 40, about 30 km south of the city of Malargüe. The intruded sediments are a part of the Malargüe fold and thrust belt, formed as a result of Mesozoic rift inversion during tertiary compressional orogeny [*Manceda and Figueroa*, 1995]. The sills are hosted in the Vaca Muerta Formation in the Mendoza Group, a marine limestone-shale unit of Tithonian to Berriasian age, that is, Upper Jurassic and Lower Cretaceous, respectively [*Leanza and Hugo*, 1978]. The age and regional extent of the sills are poorly determined, and no radiometric ages are available. However, a recent study suggests that the sills were emplaced as a part of the Huincán eruptive episode during the late Miocene [*Nullo et al.*, 2005].

3. Fracturing and Domain Division

[6] The 8–10 m thick sill intrusion has a sharp and somewhat undulating lower contact with the underlying Vaca Muerta formation (Figure 1), and it is divided into columns by a conjugate set of subvertical joints (Figure 2a). One set strikes about 70°NE and has a spacing of 1–2 m, and the other strikes 130°N–140°E and has a more narrow spacing (often <0.5 m). The resulting andesite columns are further split into blocks by horizontal joints, often confined to individual columns with spacings similar to or somewhat less than the most widely spaced vertical joints (Figure 2b).

[7] Figure 2c shows one such "block" and how it evolved during spheroidal weathering. The rings that can be observed in Figure 2c are a mixture of "onion-skin" fractures, formed by spallation, and Liesegang bands. The brown Liesegang bands are relatively enriched with ferrihydrite (see in the following). The spacing of the spheroidal cracks is usually 0.5–3 cm, whereas the spacing between the Liesegang bands is typically 2–5 mm. Most of the rings seen in Figure 2c are therefore Liesegang bands.

[8] During weathering, the block initially cut out by the jointing processes was subdivided into at least three major domains (I, II, and III, as shown in Figure 2c). Domain III was further subdivided into IIIA and IIIB, before IIIA split into IIIAa and IIIAb. This process has sometimes been referred to as twinning [cf. *Sarracino and Prasad*, 1989] but may include several generations of twins. The domain-splitting fractures do not cut Liesegang bands or onion-skin fractures encapsuling the same domain, nor do they cut preexisting domain-splitting fractures. This subdivision of domains is an example of a hierarchical fragmentation process [*Iyer et al.*, 2008; *Røyne et al.*, 2008].

[9] Figure 3 shows an example of a block subdivided into four parts, which have each developed into subspherical shapes by spheroidal weathering. The central horizontal fracture (arrow) includes a central calcite vein surrounded by a brownish layer relatively enriched with ferrihydrite (see in the following). A polished section of the lower right-hand block is shown in Figure 3b. This block was cut for a bulk rock analysis, thin sectioning, CT scanning, and Hg- and He-porosimetry.

4. Mineralogy and Microstructures

[10] Mineral compositions were obtained by a wavelength-dispersive analysis using a Cameca SX100 electron microprobe at the Department of Geosciences, University of Oslo. Natural minerals and synthetic phases were used as standards. The accelerating voltage was 15 kV, and the beam current varied between 10 and 15 nA. The counting time was 10 s on both peak and background. Data reduction was carried out with the Cameca PAP software package.

[11] The original magmatic mineralogy is dominated by euhedral plagioclase, amphibole (≈5 vol %), ilmenite, and apatite with interstitial quartz, albite, and K-feldspar. Plagioclase crystals commonly display oscillatory zoning with a range in composition from $An_{30–40}$ to $An_{40–50}$. Their grain sizes range from about 50 μm to ≈5 mm. Amphiboles are dominated by pargasites and pargasitic hornblende. Even in the best preserved rocks, chlorite occurs among the interstitial minerals, and it is presumably formed by deuteric alteration during the last stages of cooling of the magmatic rocks.

[12] The alteration of the magmatic andesite mineral assemblage was analyzed with reference to the corestone as shown in Figure 3. The weathering products (notably carbonates and ferrihydrite) are present throughout this corestone, but the progress of weathering increases toward the rim. The weathering reactions and products are shown in Figure 4. The feldspars from the central area are fresh with visible oscillatory zoning. Alteration of rims with the generation of secondary porosity and formation of albite may have been a result of late magmatic alteration rather than weathering. Toward the margin of the corestones, the plagioclase crystals often indicate that cores have been partly altered to albite and calcite. The plagioclase core regions are connected to the matrix by a set of subparallel fractures (Figure 4a).

[13] Ilmenite grains are often euhedral, and former exsolution lamellae, presumably composed of hematite, are still

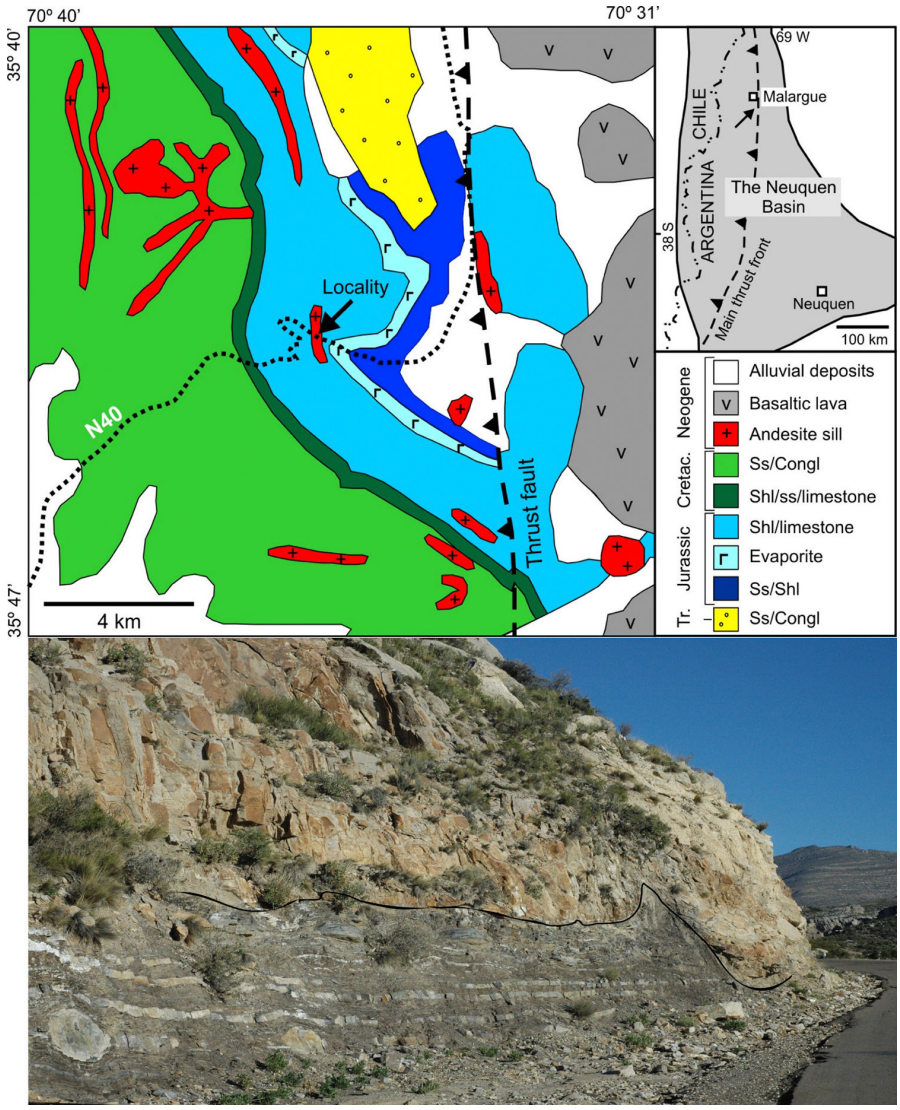

Figure 1. (top) Geological map showing the setting of the studied andesite sill within the Upper Jurassic Vaca Muerta shale-limestone formation near Malargüe in the Neuquén Basin. (bottom) Outcrop showing the lower contact of the 8–10 m thick andesite sill intrusion in the Vaca Muerta shale-carbonate sequence. The road cut strike direction is roughly 120°N.

visible. However, fresh ilmenite was not detected in this corestone. Most grains, even in the corestone cores, are highly porous and fractured (Figure 4b) and have suffered both major Fe loss and hydration, reaching Fe/Ti ratios of 1:3 and H_2O contents up to 10 wt %. The most extensive Fe loss can be observed as darker regions near fracture junctions on the backscattered electron images. The fracture patterns (Figure 4b) resemble shrinkage patterns formed by tensile stresses and could conceivably form in response to mass loss during Fe leaching. Ilmenites frequently contain inclusions of magmatic apatite and zircon.

[14] Amphibole from the core region is partly replaced by dolomite and smectite (Figure 4c). Toward the corestone margin, amphibole grains are more extensively altered, internally fractured (Figure 4d), and invariably contain calcite rather than dolomite as the carbonate phase.

[15] The complex intergrowths of carbonates and ferrihydrite containing variable amounts of Si, Al, and Ca are common throughout the corestone. In the core region, these intergrowths may contain calcite, dolomite, and siderite within the same submillimeter domains and may appear to have precipitated along with euhedral quartz crystals (Figure 4e). However, Mg-bearing carbonates are found only in the central regions of the corestones. In the area that displays Liesegang bands and spheroidal fractures, only calcite is found, often as a complex intergrowth with ferrihydrite (Figure 4f). The Liesegang bands are in fact characterized by high ferrihydrite and calcite contents.

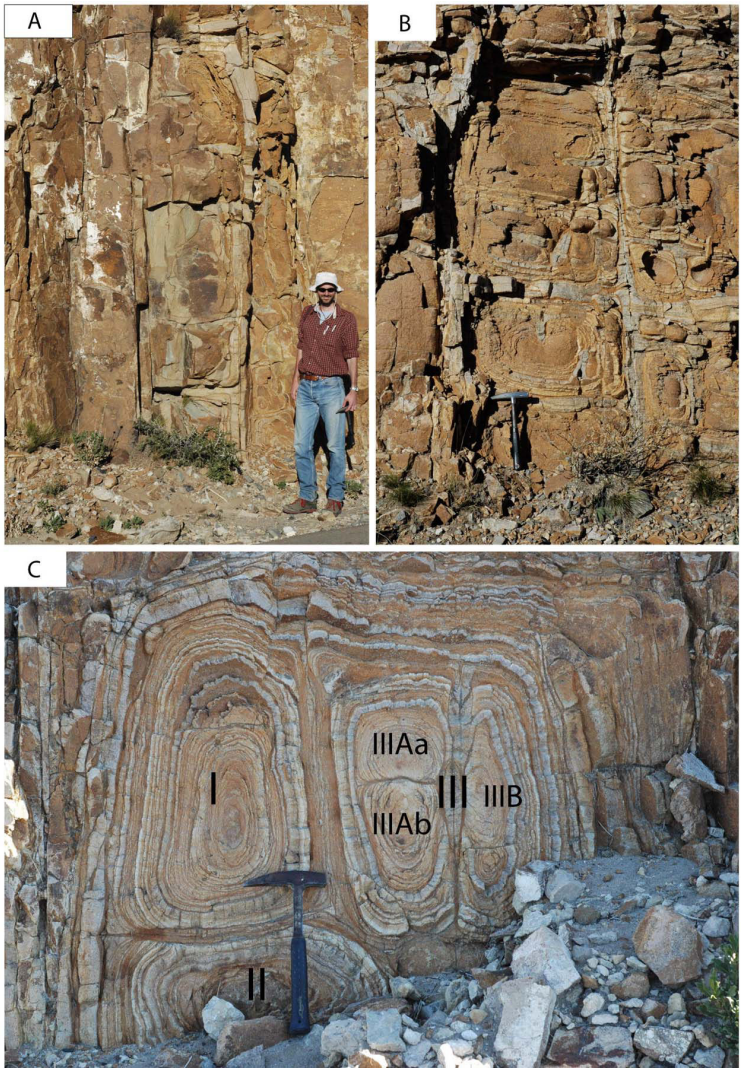

Figure 2. Lower sill contact with joints and "corestones." (a) The vertical joints strike 70°NE and have a characteristic spacing of approximately 1 m. Horizontal joints typically terminate toward the vertical joints and may have formed subsequently. (b) A conjugate set of joints strike 130°N–140°E and are more closely spaced, usually a few decimeters. These three sets of joints separate blocks (corestones) of andesite typically around 1 × 1 × 0.5 m in size. (c) A single corestone subdivided into smaller domains (I–III) by internal fracturing (see text). Domain III is further subdivided into IIIA and IIIB, before IIIA split into "twins" IIIAa and IIIAb. The brown-colored striation is a combination of Liesegang bands and "onion-skin" fractures.

[16] The fresh andesite has a porosity of approximately 8% (see in the following). The subspherical pores exceeding 100 μm in diameter are common (Figure 5a). These frequently contain euhedral quartz crystals, and they are often coated with chlorite. In weathered andesite, the pore structure is significantly modified. All pores have diameters less than 100 μm. The large pores present in the original rock seem to have been filled with a fine-grained intergrowth of carbonates and Fe-hydroxides (Figure 5b). However, the weathered rocks contain abundant microfractures, which are not present in the fresh andesite. These are typically dilated grain contacts around preexisting pores filled with weathering products (Figure 5b).

5. Mass Transfer

[17] A bulk rock analysis by standard inductively coupled plasma–mass spectrometry methods was performed on variably weathered andesites. Strictly speaking, the compositional range overlaps the andesite-dacite boundary. The results for total Fe contents (expressed as Fe_2O_3 contents) are shown in Figure 3c. Three fresh andesite samples with no ferrihydrite have Fe_2O_3 contents in the range 3.0–3.4 wt %.

Figure 3. (a) Four corestones rounded by spheroidal weathering. (b) A polished cross section of the stone in the lower-right corner of Figure 3a. This corestone contains numerous Liesegang bands and five "onion-skin" fractures (arrows). Characteristic spacing between rings: Liesegang bands, 2–5 mm; onion-skin fractures, 0.5–3 cm. (c) Bulk rock Fe_2O_3 contents for the fresh (area 1) and weathered andesites from the corestone shown in Figure 3b. Numbers correspond to locations on the corestone. The fresh andesites (area 1) are from the same outcrop a few meters away from these corestones. He- and Hg-porosimetry performed for approximately 2 cm^3 samples from the unfractured core (areas 2 and 3) and for Liesegang banded (but macroscopically unfractured) areas 5 and 6. CT scans were carried out on somewhat smaller (0.1–0.2 cm^3) samples collected between layers 3 and 4 (innermost "onion-skin" fracture) and between layers 4 and 5 (second innermost fracture). He- and Hg-porosity values are given for samples cut out from the various locations indicated by numbers in Figures 3a and 3b.

The extensively Liesegang-banded corestone shown in Figure 3b has increased Fe_2O_3 contents in the range 3.7–3.8 wt %, but no detectable core-to-rim variation. The highest Fe_2O_3 contents (4.4–4.6 wt %) were found around the central horizontal fracture as shown in Figure 3a. For the other components, no systematic weathering-related concentration shifts were found. However, the carbon required to form carbonates in the corestones must have been externally derived as the fresh andesite does not contain carbon-bearing phases.

6. Quantification of Porosity Evolution

[18] He-porosities were measured to a precision of 0.15% in a double-cell Helium porosimeter at the Core Laboratory of the Geological Survey of Denmark and Greenland (GEUS). The densities were measured using a standard pycnometer with an estimated precision of about 0.02 g/cm^3. The fresh andesite has a measured density of 2.47 g/cm^3. On the basis of the mineralogical composition, a nonporous rock would have a density of 2.65–2.70 g/cm^3. An inferred porosity of 7%–9% prior to weathering is consistent with the measured He-porosity of 8.0%. The weathered corestone in Figure 3b has a density of 2.53 g/cm^3, measured on 1–2 cm^3 sized samples, with no significant core-to-rim variation. Thus, a slight density increase is associated with the weathering process.

[19] The unfractured core of the corestone has a He-porosity of 7.5%–7.8% (two samples measured), whereas two samples of the Liesegang-banded layers ("rindlets"

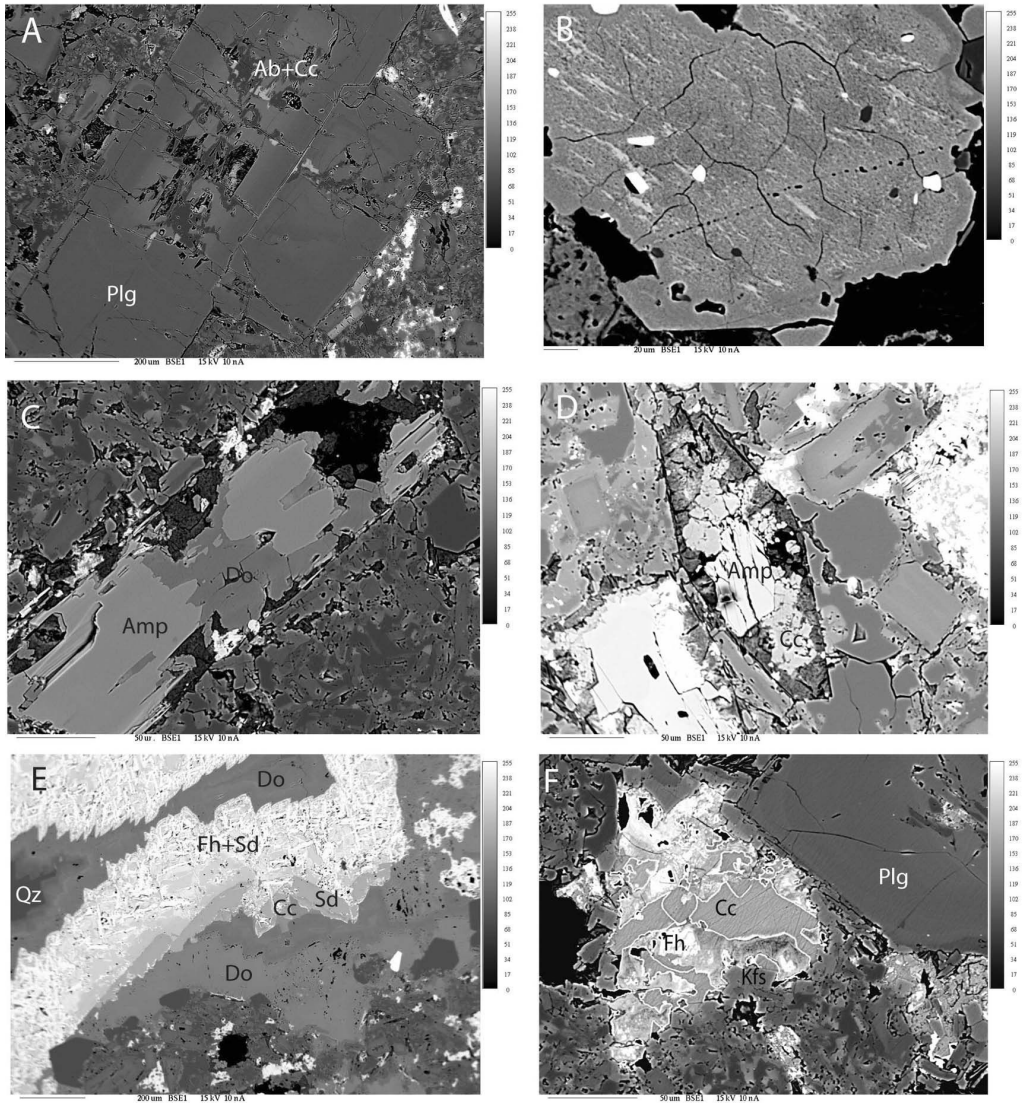

Figure 4. Backscattered electron (BSE) image of microstructures from the corestone shown in Figure 3b. (a) Plagioclase (Plg) crystal with an originally An-richer core partly altered by a mixture of albite (Ab) and calcite (Cc). Note the fractures that connect the core region to the feldspar rim. (b) Fe- and Ti-oxide/hydroxide (Fe/Ti ratio ≈ 2:3) pseudomorphing magmatic ilmenite. The replacement process is associated with a significant Fe loss and the generation of porosity and what appears to be a network of tensile cracks within the domain of the original ilmenite grain. The regions near the crack network are more Fe depleted than the surrounding regions (darker color on this BSE image). The bright grains are apatite. (c) Pargasitic amphibole (Amp) in plagioclase matrix from the central part of the corestone partly replaced by dolomite (Do). The dark mineral is a hydrous Fe-Al-Si-rich sheet silicate, possibly a smectite. (d) Amphibole crystal from the outer, fractured part of the corestone partly replaced by a mixture of calcite and a sheet silicate with chlorite-like composition. (e) Complex carbonate intergrowths from the corestone center including Do, siderite (Sd), and Cc. Sd also occurs intergrown with ferrihydrite-like oxide/hydroxide (Fh). Qz refers to quartz. (f) Complex intergrowth of calcite and ferrihydrite from the fractured part of the corestone. No Mg-carbonates are found in this region.

according to the terminology used by *Buss et al.* [2008] and others), collected between the macroscopic "onion-skin" fractures have measured porosities of 8.5% and 11.4%.

6.1. X-Ray CT

[20] One fresh and four weathered andesite samples from the corestone shown in Figure 4 were characterized by CT scanning using the Nikon Metrology model XT H 225 LC

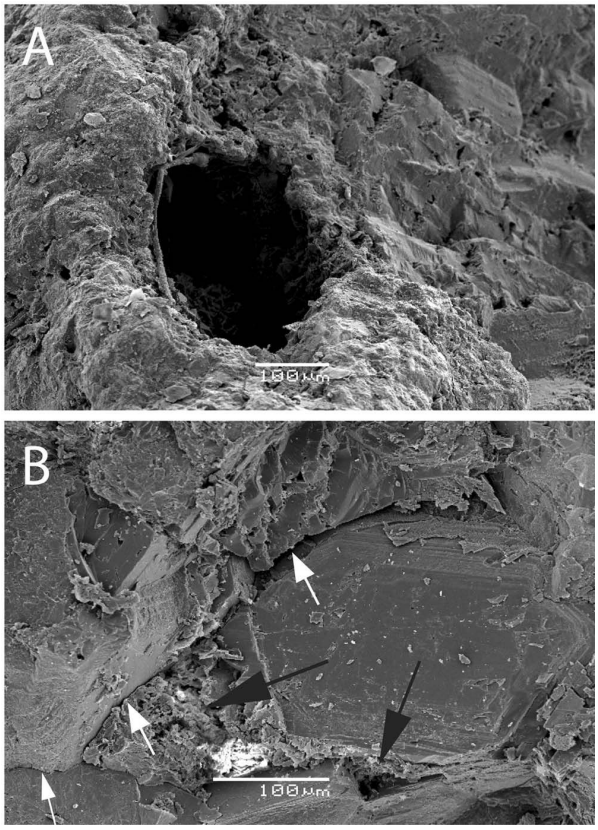

Figure 5. Secondary electron image of the surface of the (a) fresh and (b) weathered andesites. Note the large subspherical pore in Figure 5a. Dark arrows in Figure 5b indicate inferred preexisting pores that are now filled with a fine-grained mixture of ferrihydrite and calcite. White arrows indicate microfractures inferred to have formed during growth in the preexisting pores.

industrial type CT scanner at the Norwegian Geotechnical Institute. The voxel size was in the range of 5.2–7 μm for 5–7 mm sized cube-shaped samples, and the software package *Avizo Fire* was used for data analysis and image processing. The pore structures of andesite samples were obtained by thresholding the CT data to make the image consistent with petrographic observations and independent measurements of porosity and pore size distributions inferred from Hg-porosimetry (see in the following). The resulting pore structures for the fresh andesite and samples containing the innermost and second innermost, onion-skin fractures (see Figure 3) are shown in Figure 6. The pore size distributions and cumulative distributions are shown in Figure 7. Pore sizes smaller than 10^{-6} mm^3 have been ignored in the analysis because a pore diameter of approximately 10 μm approaches the CT spatial resolution.

[21] For the fresh andesite, the pore volume consisting of pores exceeding the lower cutoff of 10^{-6} mm^3 contributes a porosity of approximately 1%, with several pores exceeding 10^{-2} mm^3 and an apparently homogeneous distribution of pores (Figure 6a). The pore size distribution (Figure 7a)

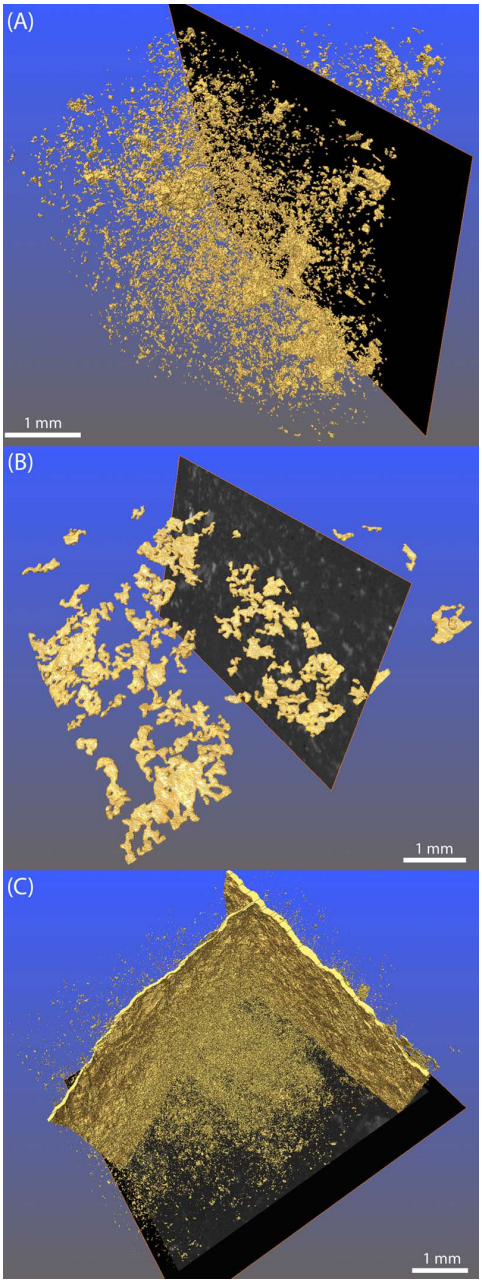

Figure 6. (a) CT representations of pores in the fresh andesite, (b) innermost "onion-skin" fracture zone (between rindlets 3 and 4 in Figure 3b) with numerous microfractures, and (c) macroscopic onion-skin fracture (NW-SE orientation) with a smaller crosscutting fracture collected between rindlets 4 and 5 as shown in Figure 3b. Porosity in the bulk of the weathered andesite between the fractures is also visualized. Note that no pores are as large as the largest pores seen in Figure 6a.

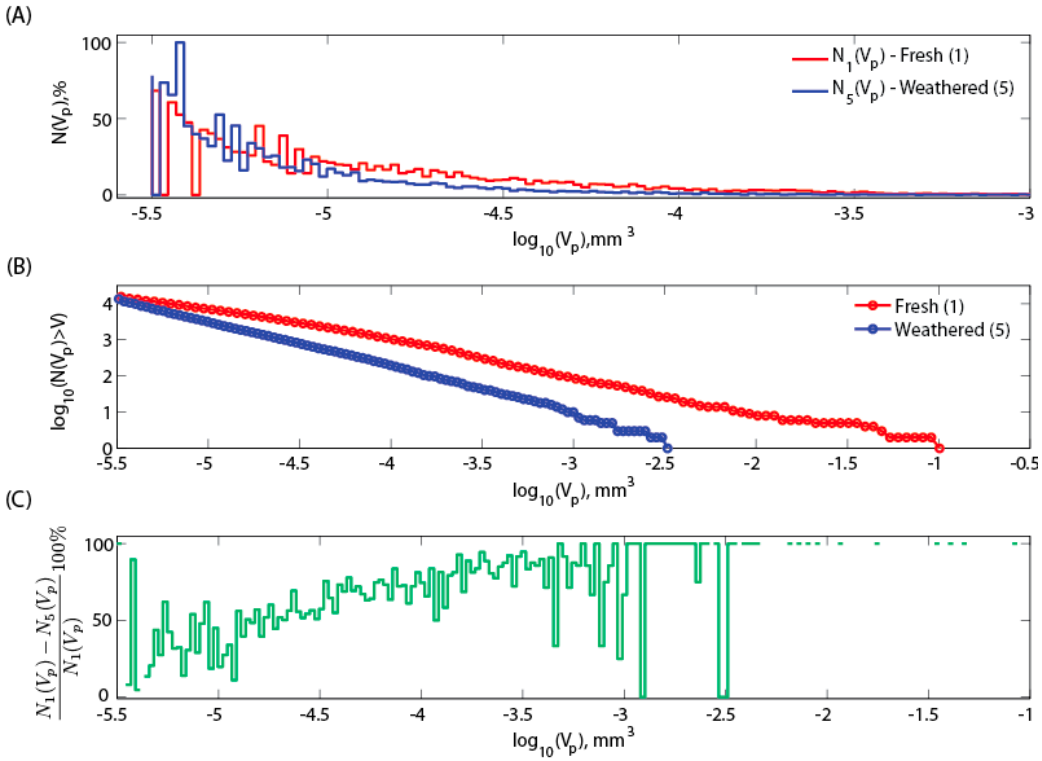

Figure 7. (a) Pore size distribution (number of pores $N(V_p)$ as a function of pore size (V_p) for pore size intervals of 0.0226 mm^3) for the fresh andesite (N_1) and weathered andesite from region 5 (N_5) normalized to the values for the interval with the largest number of pores. (b) Cumulative distribution of pore sizes for the fresh and weathered andesites. (c) Degree of filling (in %) of pores as a function of pore size.

displays an apparent power law scaling for pores greater than 10^{-4} mm^3 (Figure 7b). The corresponding slope of approximately -1.0 is comparable to the pore size distribution for the larger vesicle fraction in volcanic rocks [cf. *Klug et al.*, 2002]. In contrast, weathered andesite from the area with onion-skin fractures (see Figure 3b) has a much smaller number of large pores (ignoring the macroscopic onion-skin fractures themselves; Figure 7a). No pores larger than $10^{-2.5}$ mm^3 were observed. The pore size distribution is much steeper and corresponds to a power law exponent of approximately -1.25 (Figure 7b) for the cumulative distribution. This exponent is larger than that usually determined for fresh igneous rocks. The steep slope continues toward pore sizes below 10^{-5} mm^3, implying that the weathered rocks have a higher number of small pores, relative to the number of large pores, than the unaltered rock.

[22] Figure 7c shows that the degree of pore filling (defined as the relative difference in the number of pores occupying a given pore-volume interval between weathered and unweathered andesite) decreases with decreasing pore size. Pores with volumes greater than $10^{-3.5}$ mm^3 are almost completely filled during weathering, whereas pores with volumes lesser than 10^{-5} mm^3 are less than 50% filled. Linear extension of the trend observed for this volume range to pore volumes smaller than the resolution of the CT scans would indicate that pores with volumes lesser than 10^{-6} mm^3 (or $\sim$10 μm in diameter for spherical pores) would be nearly empty.

[23] The innermost onion-skin fracture (Figure 3b) is not a single well-defined macroscopic crack such as the one seen for the outermost onion-skin fractures. It is a narrow zone consisting of multiple microfractures. Figure 7b shows the CT representation of these microfractures. As the aperture of many of these are near or below the CT resolution, the image should not be interpreted as a "true" image of this zone because many of the microfractures that appear to be unconnected in the image may well be connected by sub-resolution-scale fractures. We still believe that Figure 7b gives a correct impression of the qualitative features of this "fracture zone." A similar microcrack system, close to an unfractured corestone in weathered granites in Galicia, was described by *Bisdom* [1967].

6.2. Mercury Porosimetry

[24] Hg-porosimetry measurements were carried out at the Core Laboratory of the GEUS using a Micromeritics Autopore-IV porosimeter. Hg capillary pressure was measured with an injection sweep from vacuum to 60,000 psi (400 MPa). Pore throat sizes can be measured from 200 μm down to $\sim$3 nm, covering pore size distributions in the micro-, meso-, and macropore range.

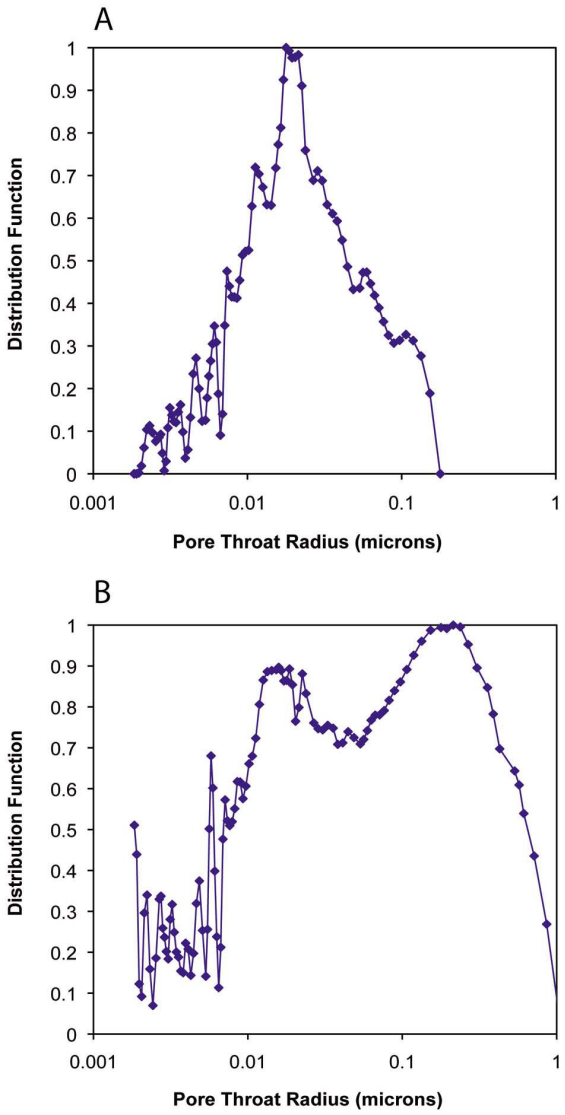

Figure 8. Distribution of pore throat radii for the (a) fresh and (b) weathered andesites (from region 5) obtained by Hg-porosimetry.

[25] The Hg-injection data gave lower porosities than the He-data. The fresh andesite gave 5.7% porosity, the unfractured cores of the corestone shown in Figure 3 (area 2) gave 5.2%, whereas two samples of the Liesegang-banded rims gave 5.5% and 6.0% porosity. Thus, 20%–30% of the overall porosity present in the andesite (fresh or weathered) was not accessible to Hg. This implies that a substantial fraction of the pores have pore throats that are too narrow for Hg to enter. Under these analytical conditions, this indicates that pore throat radii are less than about 5 nm. Figures 8a and 8b show the frequency distribution of pore throat radii obtained for the fresh andesite and Liesegang-banded weathered andesite (area 5 in Figure 3). The fresh andesite shows a total range in pore throat radii of 2–180 nm, with a maximum around 20 nm (Figure 8a). The inferred pore diameter [cf. *Washburn*, 1921] ranges from 4 nm to 140 μm, with a maximum near 10 μm. The weathered andesite shows a distinctly different distribution of pore throat radii with two distinct peaks (Figure 8b). One peak corresponds to the peak for the fresh andesite near 20 nm, whereas the other and slightly higher peak is near 200 nm. The total range in pore throat radii is also much larger for the weathered sample (2–1075 nm). The inferred range of pore diameters is similar for unaltered andesite, but the fraction of large pores is higher with a maximum frequency near 35 μm. This is in contrast to the results from analysis of the CT data that indicate a reduction in the abundance of large pores in the weathered samples. The discrepancy is clearly related to the fact that the resolution of the CT images is insufficient to record microfractures with a fracture aperture less than approximately 10 μm, and the assumptions made when Hg-injection data are interpreted in terms of pore sizes and pore size distributions [cf. *Capek and Hejtmanek*, 2009].

[26] On the basis of the SEM and CT observations, we interpret the second (and highest) peak in the Hg-porosimetry data to reflect the presence of the microfractures. The microfractures may have "pore throats" that are much larger than those associated with even the largest subspherical pores in the original andesite but still small enough to be unobservable in the CT images.

7. Discussion

[27] Previous models for spheroidal weathering of igneous rocks, including both the formation of rindlets by surface-parallel spallation processes [e.g., *Chapman and Greenfield*, 1949; *Fletcher et al.*, 2006] and the hierarchical fragmentation of corestones [*Røyne et al.*, 2008], have attributed fracturing to *volumetric expansion* during oxidation and/or hydration of the original, essentially nonporous, magmatic rock. As has been demonstrated by numerous articles on frost damage [e.g., *Taber*, 1929; *Everett*, 1961; *Walder and Hallet*, 1986] and salt weathering [*Espinosa-Marzal and Scherer*, 2010], this approach is generally inadequate for the porous systems open to exchange of mass with the environment.

[28] Both the CT and Hg-porosimetry data clearly demonstrate that the weathering process is associated with a marked change in the pore structure. The growth of the weathering products is confined to large pores, while smaller (even nanoscale) pores stay open during weathering. Moreover, grain boundary dilation and generation of microfractures can be observed around the largest pores during weathering.

[29] The precipitation of pore-filling material from supersaturated solutions is well known to generate stresses sufficiently high to cause fracturing, and this can lead to rapid fracturing associated during weathering in a range of systems, including concrete and other porous materials [cf. *Goudie and Viles*, 1997; *Scherer*, 2004]. In this study, the andesite is emplaced in carbonate-bearing sedimentary rocks, and fractures in the andesite are commonly filled with calcite. Thus, it seems reasonable to assume that the fluid involved in the weathering reactions is calcite saturated even before entering the andesite. During interaction with the magmatic mineralogy, weathering-related hydrolysis of magmatic silicates and oxides will consume protons and increase the pH of

the pore fluid. Moreover, dissolved Fe from amphibole and ilmenite hydrolysis is expected to become oxidized by the infiltrating fluids under these near-surface conditions. This will drive *both* carbonate and ferrihydrite precipitation through a set of coupled reactions:

$$\text{(R1)}\quad Ca_2Fe_5Si_8O_{22}(OH)_2(\text{actinolite}) + 14H^+ = 2Ca^{2+} + 5Fe^{2+} + 8SiO_2\,(\text{quartz}) + 8H_2O$$

$$\text{(R2)}\quad Ca^{2+} + HCO_3^- = CaCO_3\,(\text{calcite}) + H^+$$

$$\text{(R3)}\quad 2Fe^{2+} + \frac{1}{2}O_2 + (3+n)H_2O = 2FeOOH \cdot nH_2O\,(\text{ferrihydrite}) + 4H^+,$$

where n is a stoichiometric coefficient accounting for variable water contents in the ferrihydrite. In this case, actinolite ($Ca_2Fe_5Si_8O_{22}(OH)_2$) is representative of any magmatic mineral in terms of consuming protons during hydrolysis. The weathering of ilmenite and plagioclase would, in a similar way, consume protons and produce Ca and Fe ions, respectively. SiO_2 is a weathering product commonly observed to grow in the pore space along with carbonate and ferrihydrite (Figure 4e). The formation of the weathering products (calcite and ferrihydrite) is favored both by the proton consumption and by the production of cations (Ca and Fe) during hydrolysis of the original magmatic minerals. At the same time, the proton production during the formation of the weathering products provides a positive feedback to the hydrolysis of the magmatic minerals.

[30] The weathering process is an autocatalytic reaction. Once started, the progress of this reaction can only be halted by precipitation in the pore space to reduce either the reactive surface area or to limit the access of externally derived components by clogging the connected pore structure. The externally derived components include H_2O, HCO_3^-, and O_2. Reactions (R1)–(R3) can be combined to conserve either protons or divalent cations. Conserving Fe and Mg requires an external source of protons. If Fe is supplied externally, as indicated in Figure 3, the overall reaction may conserve protons and Ca^{2+}.

[31] The pervasive weathering of meter-sized blocks such as those observed in Figures 2 and 3 indicates that these processes were inefficient. Thus, a central question is: What processes maintain the porosity during weathering? On the basis of the observations described earlier, it is clear that the porosity is maintained in two ways: Small pores do not become filled with weathering products, and the growth of weathering products in the large pores cause them to expand to produce new porosity through microfracturing. The expansion by microfracturing eventually leads to macroscopic spalling of layers to produce the observed onion-skin fracturing and rindlet formation.

7.1. Stress Generation Mechanism

[32] Supersaturation of pore fluids implies that mineral growth in the pores may generate a significant local stress and may potentially cause porosity and permeability generation by fracturing processes. An explicit relationship between supersaturation (Ω = ion activity product/solubility product) and the stress generated by crystal growth in a pore can be expressed as [*Steiger*, 2005]:

$$\Delta p_c = \frac{RT}{v_0}\ln\Omega - \gamma_{cl}\kappa_{cl}, \tag{1}$$

where Δp_c is the deviatoric "pressure" (stress) defined as the difference between the pressure on the advancing crystal face and the pressure of the surrounding liquid. For small pores (<0.1 μm), curvature effects must be taken into account. In equation (1), γ_{cl} is the crystal-liquid interfacial energy, κ_{cl} is the local curvature, R is the Boltzmann constant, ν_0 is the molar volume, and T is the temperature.

[33] Because of the surface energy effects on crystal solubility, increased supersaturation levels may be maintained in submicron-sized pores. Thus, a rock with a broad initial distribution of pore sizes may thus experience growth in the larger pores, while crystals in small pores may even dissolve [*Everett*, 1961; *Emmanuel and Berkowitz*, 2007]. In terms of the distribution of deviatoric pressures generated by the growing crystals, it is expected that a steady state will be reached at a given value of Ω, in which an equilibrium pressure is exerted in the largest pores in the system, and a distribution of lower pressures (down to zero) is observed in the smallest pores.

[34] For a porous rock in which the individual pores are subject to an internal crystallization pressure, the mechanical response will depend on the distribution of individual stress intensity factors K_I. Because K_I scales with the square root of the pore size, large pores may expand by subcritical crack growth, while small pores remain unfractured. Macroscopic fracturing, such as the onion-skin spalling process observed during spheroidal weathering, may arise either through linking of individual microfractures formed during "popping" of a sufficient number of the larger pores or as a response to the elastic stresses generated by inflation of nonfractured pores. In this study, we observe abundant microfractures around pores filled by the weathering products. We also observe that the innermost onion-skin related fracture (or rather fracture zone) is composed of a number of microfractures. Thus, the macrofractures are probably at least to some extent formed by coalescence of microfractures.

[35] Treating the rock as a continuum deformed by expansion of pores, the crystallization pressure (Δp_c) will result in an expansion of the rock analogous to thermal expansion, and the strain ε is given by [*Espinosa-Marzal and Scherer*, 2010]

$$\varepsilon = \frac{bS_c\Delta p_c}{K}, \tag{2}$$

where K is the bulk modulus of the rock, b is the Biot coefficient of the rock ($b = 1 - K/K_s$ where K_s is the bulk modulus of the solid part of the rock), and S_c is the volume fraction of expanding pores. When crystallization-driven stress is building up in the outer layer of the rock volume, it is free to expand in the direction normal to the rock surface but constrained in the direction parallel to the surface. The resulting surface-parallel stress is given by [*Timoshenko*, 1970]

$$\sigma = 3K\varepsilon, \tag{3}$$

When the elastic energy built up in the outer layer of the rock becomes sufficiently large, it spalls by the formation of fractures parallel to the surface. The spalling of a surface layer due to edge loads was analyzed by *Hutchinson and Suo* [1991] for a 2-D geometry, and they found that the elastic strain energy is large enough to drive a surface-parallel crack when the thickness of the layer (assuming a uniform surface-parallel stress) is given by

$$h = \frac{2\Gamma E}{\sigma^2}, \tag{4}$$

where h is the thickness of the layer, E is the elastic modulus, and Γ is the surface energy of the rock. In this study, the average thickness of the layers spalled off during spheroidal weathering is about 2.5 cm. For typical values of E (2×10^5 MPa) and Γ (200 Pa), this corresponds to a surface-parallel stress of approximately 30 MPa. From equations (1) and (3) (with parameter values from the study by *Fletcher et al.* [2006] and the molar volume of calcite), this corresponds to a "crystallization pressure" of 20 MPa and a supersaturation (Ω) of only about 1.2. By comparison, the supersaturation required to form ferrihydrite, rather than the more stable goethite and hematite, at 25°C and 1 bar is higher by factors of 2.2 and 6.5, respectively.

7.2. Liesegang Banding and Causes of Growth in Large Pores

[36] The precipitation of weathering products produces a sequence of 5–10 Liesegang bands or rings, within each rindlet. Macroscopic fracturing is always parallel to these bands. Because the stresses generating fracturing is produced by precipitation of the weathering products, these stresses do not built up homogeneously within each rindlet but are to some extent focused to the Liesegang bands. The observations indicate that the stresses accumulating in the andesite during the formation of Liesegang bands exceeds that required to produce a new rindlet by spalling when 5 to 10 bands have precipitated. However, there is another important implication of the pattern-forming process operating during Liesegang band formation. The current models for the origin of Liesegang banding during coupled diffusion and precipitation in gels or porous systems invoke either a supersaturation-nucleation-depletion process [*Ostwald*, 1897; *Smith*, 1984] or a postnucleation, surface tension-mediated, competitive particle growth mechanism [*Sultan and Ortoleva*, 1993]. In this study, supersaturation arises because of the counter-diffusion of ions that can form a precipitate, and this is very similar to a Liesegang experiment, with an external source of carbon and oxygen, and an internal production of cations (Ca, Fe, Mg). Furthermore, we observe that the Liesegang bands are invariably oriented parallel to the macroscopic fractures. It is hard to see how these features of the system can be explained by a post-nucleation redistribution of mass driven by surface tension. Thus, we argue that the observed Liesegang banding is generated by a supersaturation-nucleation-depletion process.

[37] Nucleation control on the site of precipitation of the weathering products provides a possible mechanism for the observed correlation between pore size and amount of pore filling as the nucleation probability is higher in large pores [*Chen et al.*, 1998]. Once growth commences in the large pores, a local reduction in supersaturation will cause diffusion toward the large pores and prevent nucleation in smaller pores. Thus, for a system characterized by slow nucleation and rapid growth, it is expected that large pores will become filled before smaller pores. A pore size effect on the degree of pore filling might be observed even for pores that are too big for surface tension to play a major role. In this study, we see this effect for pores approaching 100 μm (see Figure 7). As Liesegang banding is quite commonly observed during spheroidal weathering in a range of systems [*Augustithis and Ottemann*, 1966; *Singer and Navrot*, 1970; *Augustithis et al.*, 1980], there should be ample opportunities to test such a model.

8. Conclusions

[38] A spectacular example of spheroidal weathering of andesite from the Neuquén Basin in Argentina reveals the progress of weathering-related fragmentation through a combination of Liesegang banding and fracture patterns. Microtomography and Hg-porosimetry reveal how ferrihydrite and calcite precipitate in the largest pores of the andesite during hydrolysis and oxidation of the original magmatic minerals. The precipitation is focused along millimeter-spaced (Liesegang) bands, and there are typically 5–10 Liesegang bands between each macroscopic "onion-skin" fracture. The growth of the weathering products generates local stresses that initiate microfracturing and eventually drives macroscopic onion-skin fracturing by coalescence of microfractures, as well as several stages of corestone division or "twinning." Both the Liesegang banding and the preferential growth in large pores are consistent with a supersaturation-nucleation-depletion process in which the rate of nucleation increases with an increase in pore size.

[39] **Acknowledgments.** We thank Hector Leanza (Universidad Nacional de Córdoba) for his guidance during the fieldwork and for introducing us to the local geology and the associated literature. We also thank Paul Meakin, Bruce Yardley, and an anonymous reviewer, who provided valuable comments on the manuscript. The company of Sverre Planke, Ellen Eckhoff Planke, Adriano Mazzini, Fernando Corfu, and Olivier Galland (all from the University of Oslo) during the field trip to the Neuquén Basin is highly appreciated. We extend our sincere gratitude to Øistein Johnsen at the Norwegian Geotechnical Institute for conducting the CT scanning. This study was supported by a Center of Excellence grant to PGP from the Norwegian Research Council.

References

Augustithis, S. S., and J. Ottemann (1966), On diffusion rings and spheroidal weathering, *Chem. Geol.*, *1*, 201–209, doi:10.1016/0009-2541(66)90016-7.

Augustithis, S. S., E. Mposkos, and A. Vgenopoulos (1980), Diffusion rings (spheroids) in bauxite, *Chem. Geol.*, *30*, 351–362, doi:10.1016/0009-2541(80)90101-1.

Bisdom, E. B. A. (1967), The role of micro-crack systems in the spheroidal weathering of an intrusive granite in Galicia (NW Spain), *Geol. Mijnbouw*, *46*, 333–340.

Brantley, S. L., M. B. Goldhaber, and K. V. Ragnarsdottir (2007), Crossing disciplines and scales to understand the Critical Zone, *Elements*, *3*, 307–314, doi:10.2113/gselements.3.5.307.

Buss, H. L., P. B. Sal, A. M. Webb, and S. L. Brantley (2008), Weathering of the Rio Blanco quartz diorite, Luquillo Mountains, Puerto Rico: Coupling oxidation, dissolution, and fracturing, *Geochim. Cosmochim. Acta*, *72*, 4488–4507, doi:10.1016/j.gca.2008.06.020.

Capek, P., and V. Hejtmanek (2009), A relationship between pore shapes and mercury porosimetry curves as revealed by random pore networks. *R. Soc. Chem. Publ.*, *318*, 385–393.

Chan, M. A., W. A. Yonkee, D. I. Netoff, W. M. Seiler, and R. L. Ford (2008), Polygonal cracks in bedrock on Earth and Mars: Implications for weathering, *Icarus*, *194*, 65–71, doi:10.1016/j.icarus.2007.09.026.

Chapman, R. W., and M. A. Greenfield (1949), Spheroidal weathering of igneous rocks, *Am. J. Sci.*, *247*, 407–429, doi:10.2475/ajs.247.6.407.

Chen, S. L., P. P. Wang, and T. S. Lee (1998), An experimental investigation of nucleation probability in supercooled water inside cylindrical capsules, *Exp. Therm. Fluid Sci.*, *18*, 299–306, doi:10.1016/S0894-1777(98)10040-7.

Cobbold, P. R., and E. A. Rossello (2003), Aptian to recent compressional deformation, foothills of the Neuquén Basin, Argentina, *Mar. Pet. Geol.*, *20*, 429–443, doi:10.1016/S0264-8172(03)00077-1.

Emmanuel, S., and B. Berkowitz (2007), Effects of pore-size controlled solubility on reactive transport in heterogeneous rock, *Geophys. Res. Lett.*, *34*, L06404, doi:10.1029/2006GL028962.

Espinosa-Marzal, R. M., and G. W. Scherer (2010), Advances in understanding damage by salt crystallization, *Acc. Chem. Res.*, *43*, 897–905, doi:10.1021/ar9002224.

Everett, D. H. (1961), The thermodynamics of frost damage to porous solids, *Trans. Faraday Soc.*, *57*, 1541–1550, doi:10.1039/tf9615701541.

Fletcher, R. C., H. L. Buss, and S. L. Brantley (2006), A spheroidal weathering model coupling porewater chemistry to soil thickness during steady-state denundation, *Earth Planet. Sci. Lett.*, *244*, 444–457, doi:10.1016/j.epsl.2006.01.055.

Goudie, A. S., and H. A. Viles (1997), *Salt Weathering Hazards*, John Wiley, Chichester, U.K.

Gulisano, C. A., and A. R. Gutiérrez Pleimling (1995), *The Jurassic of the Neuquén Basin, Field Guide: B) Mendoza Province*, Asoc. Geol. Argentina, Buenos Aires.

Hutchinson, J. W., and Z. Suo (1991), Mixed-mode cracking in layered materials, *Adv. Appl. Mech.*, *29*, 63–191, doi:10.1016/S0065-2156(08)70164-9.

Iyer, K., B. Jamtveit, J. Mathiesen, A. Malthe-Sørenssen, and J. Feder (2008), Reaction-assisted hierarchical fracturing during serpentinization, *Earth Planet. Sci. Lett.*, *267*, 503–516, doi:10.1016/j.epsl.2007.11.060.

Jamtveit, B., C. Putnis, and A. Malthe-Sørenssen (2009), Reaction induced fracturing during replacement processes, *Contrib. Mineral. Petrol.*, *157*, 127–133, doi:10.1007/s00410-008-0324-y.

Klug, C., K. Cashman, and C. Bacon (2002), Structure and physical characteristics of pumice from the climactic eruption of Mount Mazama (Crater Lake), Oregon, *Bull. Volcanol.*, *64*, 486–501, doi:10.1007/s00445-002-0230-5.

Leanza, H. A., and C. A. Hugo (1978), Sucesión de ammonites y edad de la Formación Vaca Muerta y sincrónicas entre los paralelos 35° y 50° L. S. Cuenca Neuquina-Mendocina, *Asoc. Geol. Argent. Rev.*, *32*, 248–264.

Manceda, R., and D. Figueroa (1995), Inversion of the Mesozoic Neuquén rift in the Malargüe fold thrust belt, Mendoza, Argentina, in *Petroleum Basins of South America*, vol. 62, edited by A. J. Tankard et al., pp. 369–382, Am. Assoc. Pet. Geol. Mem., Boulder, Colo.

Nullo, F. E., G. Stephens, A. Combina, L. Dimieri, P. Baldauf, P. Bouza, and J. C. M. Zanettini (2005), *Hoja geológica 3569-III/3572-IV Malargüe, provincia de Mendoza*, Bol. 346, 85 pp., Servicio Geológico Minero Argentino, Instituto de Geología y Recursos Naturales, Buenos Aires.

Ollier, C. D. (1971), Causes of spheroidal weathering, *Earth Sci. Rev.*, *7*, 127–141, doi:10.1016/0012-8252(71)90005-5.

Ostwald, W. (1897), Besprechung der Arbeit von Liesegang A-Linien. *Z. Phys. Chem.*, *23*, 365.

Røyne, A., B. Jamtveit, J. Mathiesen, and A. Malthe-Sørenssen (2008), Controls on weathering rates by reaction induced hierarchical fracturing, *Earth Planet. Sci. Lett.*, *275*, 364–369, doi:10.1016/j.epsl.2008.08.035.

Sarracino, R., and G. Prasad (1989), Investigation of spheroidal weathering and twinning, *GeoJournal*, *19*, 77–83.

Scherer, G. W. (2004), Stress from crystallization of salt, *Cement Concr. Res.*, *34*, 1613–1624, doi:10.1016/j.cemconres.2003.12.034.

Singer, A., and J. Navrot (1970), Diffusion rings in altered basalt, *Chem. Geol.*, *6*, 31–41, doi:10.1016/0009-2541(70)90003-3.

Smith, D. A. (1984), On Ostwald's supersaturation theory of rhythmic precipitation (Liesegang's rings), *J. Chem. Phys.*, *81*, 3102–3115, doi:10.1063/1.448012.

Steiger, M. (2005), Crystal growth in porous materials–II: The crystallization pressure of large crystals, *J. Cryst. Growth*, *282*, 470–481, doi:10.1016/j.jcrysgro.2005.05.008.

Strudley, M. W., A. B. Murray, and P. K. Haff (2006), Regolith thickness instability and the formation of tors in arid environments, *J. Geophys. Res.*, *111*, F03010, doi:10.1029/2005JF000405.

Sultan, R., and P. Ortoleva (1993), Periodic and aperiodic macroscopic patterning in two precipitate post-nucleation systems, *Physica D*, *63*, 202–212, doi:10.1016/0167-2789(93)90155-T.

Taber, S. (1929), Frost heaving, *J. Geol.*, *37*, 428–461, doi:10.1086/623637.

Timoshenko, S. (1970), *Theory of Elasticity*, McGraw-Hill, New York.

Turner, B. F., R. F. Stallard, and S. L. Brantley (2003), Investigation of in situ weathering of quartz diorite bedrock in the Rio Icacos Basin, Luquillo Experimental Forest, Puerto Rico, *Chem. Geol.*, *202*, 313–341, doi:10.1016/j.chemgeo.2003.05.001.

Twidale, D. R. (2002), The two-stage concept of landform and landscape development involving etching: Origin, development and implications of an idea, *Earth Sci. Rev.*, *57*, 37–74, doi:10.1016/S0012-8252(01)00059-9.

Vidal Romani, J. E. (2008), Forms and structural fabric in granite rocks, *Cadernos Lab. Xeol. Laxe*, *33*, 175–198.

Walder, J. S., and B. Hallet (1986), The physics of frost weathering: Toward a more fundamental and unified perspective, *Arct. Alp. Res.*, *18*, 27–32, doi:10.2307/1551211.

Washburn, E. W. (1921), The dynamics of capillary flow, *Phys. Rev.*, *17*, 273–283, doi:10.1103/PhysRev.17.273.

H. Austrheim, B. Jamtveit, M. Kobchenko, A. Malthe-Sørenssen, A. Røyne, and H. Svensen, Physics of Geological Processes, University of Oslo, PO Box 1048 Blindern, N-0316 Oslo, Norway. (bjorn.jamtveit@geo.uio.no)